Using acoustic backscatter data to provide estimates of profiles of suspended sediment concentrations for cohesive particles in the field

A thesis

submitted in partial fulfilment

of the requirements for the Degree

of

Master of Science (Research) in Earth Sciences

at

The University of Waikato

by

Isabella Redder

THE UNIVERSITY OF
WAIKATO
Te Whare Wānanga o Waikato

2023

Abstract

Many estuaries and rivers in New Zealand and other locations worldwide are stressed by the input of fine (muddy) sediments. Suspended sediment concentrations (SSC) are often used as a key indicator of water quality and are a critical variable in management practices to aid in the health of estuarine habitats. However, robust measurements of SSC are difficult to obtain, owing in part to large gradients in conditions, and the process of 'flocculation' or aggregation of fine particles. Amongst the range of measurement tools available, acoustic backscatter (ABS) sensors offer significant potential to provide temporally and spatially well resolved profiles of SSC from the field. The process of 'inversion' or converting the acoustic backscatter signal into SSC is effective when all terms are known within the theoretical context. However, the challenge facing the use of ABS technology in the field, is the scattering properties, the form function f_∞ and the total scattering cross-section Σ_s, of cohesive particles typical in estuarine environments, are unknown.

For this study, a unique laboratory calibration combined with ABS field data from a mudflat, were used to investigate if a pair of f_∞ and Σ_s values could be evaluated for finer grain, mud material as opposed to sand particles. The derived f_∞ and Σ_s values appeared to be influenced by other physical controls from the field environment and were sensitive to several assumptions made in the inversion equation. Nonetheless, the acoustic data yielded reasonable estimates of SSC in a field setting, when compared to discrete single-point measurements of SSC obtained from a calibrated optical backscatter sensor. However, there were also times when the inversion methodology did not work

well (particularly for acoustic transducers with lower frequencies). Moreover, inversion results were better when using time-varying values for f_∞ and Σ_s, the inversion procedure implemented with a universal set parameters did not perform as well. These results imply more research is needed in gathering better descriptions of the f_∞ and Σ_s values from multiple ABS frequencies, to improve inversion SSC results from the field.

Acknowledgements

I would like to express my gratitude to all those who have supported and guided me throughout this master's research journey. To my supervisors, Dr Julia Mullarney (University of Waikato) and Dr Iain MacDonald (NIWA), your guidance, expertise, and support throughout this research endeavour are appreciated. Your insightful feedback and encouragement have been instrumental in shaping the direction and quality of this work.

I am extremely thankful to the Ministry of Business, Innovation and Employment (MBIE) for the funding support of my master's research. To the National Institute of Water and Atmospheric Research Ltd (NIWA) thank you for providing the necessary equipment and resources to conduct the research. Facilitating the acquisition of essential equipment has contributed to the accuracy and reliability of the findings. I am grateful for NIWA's and MBIE's belief in the significance of this study and their commitment to advancing scientific knowledge applying acoustic technology in the field of cohesive particles.

I would also like to acknowledge Dani McMonagle, your assistance in the laboratory was much appreciated. To my friends in the Coastal Marine Group, particularly Toby Biesely and Bérengère Dejeans, thank you for being there to lend an ear and offer support. Your laughter, encouragement, and shared 'ups and downs' have made this road, which has been challenging at times, easier to navigate.

To my loving family, your unconditional love, unwavering belief in me, and endless encouragement have been my driving force.

Table of Contents

List of Figures

List of Tables

Chapter 1

Introduction

Estuaries represent the interface between land and the oceans: with approximately 87% of the global land surface connected to the ocean by rivers (Ludwig and Probst, 1998). Estuaries are defined as semi-enclosed, intermediary coastal water bodies where saline tidal currents interact with land-derived freshwater runoff (Pritchard, 1967). Half of land surface drainage, 50% of freshwater runoff and 40% of the transport of particulate matter enters the ocean via twenty-five of the world's largest river-front delta estuaries (Bianchi and Allison, 2009). As a result, these dynamic, intertidal mixing zones are often highly productive ecosystems (Chapman and Wang, 2001), which foster a selection of endemic benthic fauna and sediment-residing organisms (Chapman and Wang, 2001; Thrush et al., 2004), which are well-adapted to the intense biological, chemical, and physical reactions taking place. Accordingly, estuaries acquire high intrinsic, ecological value (Thrush et al., 2004) by facilitating numerous ecosystem services of a benefit to humans, for example nutrient cycling, food production and recreational use (Costanza et al., 1997; Thrush et al., 2013). The economic value of ecosystem services provided by coastal systems like estuaries is estimated at US \$10.6 trillion yr^{-1} (Costanza et al., 1997). Despite this high value of natural capital, the ecological health of estuaries worldwide is degrading (Barbier et al., 2011; Thrush et al., 2004). In New Zealand in particular, sedimentation is acknowledged as a key stressor of the coastal marine environment (Douglas et al., 2018; Levin et al., 2001), with enhanced levels of

sediment input driven by increased industrial, urban, and agricultural catchment activities, in addition to expanded land use conversion (Bulmer et al., 2022; Little et al., 2017; Thrush et al., 2004). Accelerated input of sediment affects the state of turbidity, water quality, morphology, mortality rate of organisms and biogeochemistry of an estuary (Bulmer et al., 2022; Little et al., 2017; Thrush et al., 2004; Urlich, 2020).

The approximately 18,000-km long New Zealand shoreline encompasses 443 estuaries with estuarine habitats covering about 5300 km^2 (Hume et al., 2007; National Institute of Water & Atmospheric Research (NIWA) Ltd., 2016). Clearance of radiata pine (*Pinus radiata*) forestry in the Marlborough Sounds since the 1970s has caused soil erosion and high sedimentation deposition of fine sediment into the surrounding estuarine ecosystems (Urlich, 2020). Other seafloor disturbance activities such as dredging, reclamation and trawling have modified shorelines and increased the amount of suspended sediment in estuaries (Jones, 1992; Kanga et al., 2020; Little et al., 2017; Thrush et al., 2013). At high sediment concentrations, bonded contaminants can have toxic effects on biota and inhibit nutrient cycling (Little et al., 2017). High sediment loads proportionally increase nutrient enrichment of estuarine intertidal flats, leading to eutrophication (Thrush et al., 2013). Deposition of muddy material can smother bed species (Thrush et al., 2013), alter the erodibility and mobility of the bed substrate (Staudt et al., 2017, 2019) and change the cohesiveness of the estuarine sediments, which in turn alters the geochemical gradients governing solute transport between the sediment pores and water (Lohrer et al., 2004). In a New Zealand study of Whitford Bay in the North Island, as little as a 3 mm-layer of terrigenous sediment was enough to adversely change the composition of microbenthic and faunal communities (Lohrer et al., 2004). Increased suspended sediment concentration (SSC) of fine inorganic silts and clays also affects benthic suspension feeders filtering the seawater column (Lohrer et al., 2004; Thrush et al., 2004). Specifically, fine sediments can choke the filter-

feeding anatomy of such organisms, requiring increased energy expenditure to clear away particles, and thus impacting the overall growth and reproduction of the species. In addition to smothering, fine sediments suspended in the water column strongly attenuate sunlight with depth, and therefore controlling the light climate of benthic flora and fauna. Light penetration into the water column and to the benthos is fundamental as light is the primary energy source on which nearly all aquatic ecosystems depend (Davies-Colley et al., 2003).

The assemblage of estuarine sediments is neither exclusive to marine nor terrestrial sources (Chapman and Wang, 2001). 'Mud' as a natural, abiotic (inorganic) and biotic (organic) composed substance is described as "a dense mixture of water and particles of diameters that are predominantly smaller than 63 μm" (Mehta, 2013). After transportation down fluvial systems (Nittrouer et al., 2017), single grain suspended particles ($< 64\,\mu$m) include mainly fine silt and clay with some detritus, natural organic matter, and sand which tend to carry dissolved, surface nutrients and contaminants (Mehta, 2022; Milligan and Loring, 1997; Nittrouer et al., 2017).

Accurate monitoring of suspended sediment concentrations is needed to underpin estuarine management practices, restoration efforts and engineering applications focused on sediment dynamics (Kanga et al., 2020; Rai and Kumar, 2015; Staudt et al., 2019). SSC measurements are also essential to calibrate and validate numerical models of hydro- and morpho- dynamics (Anh et al., 2022); however, given the significant spatial temporal variability of SSC, reliable measurements of this key indicator of water quality throughout the water column are not easily obtained (Kanga et al., 2020; Rai and Kumar, 2015). These difficulties are due in part to the dynamic process of flocculation. 'Flocs' are described as heterogenous, irregular aggregates, which form when suspended sediment grains ($< 64\,\mu$m) collide in water (O'Laughlin et al., 2014; Safak et al., 2013). Flocculation changes the size, composition, and density of the

particles, thus changing the settling velocity, and influencing how far a particle can travel before being deposited on the seafloor (Milligan and Hill, 1998; Milligan et al., 2007; Winterwerp, 1998; Winterwerp et al., 2006). However, the tendency of flocs to combine in suspension is unresolved in terms of predicting the concentration, size, and density of precipitated mud agglomerates. The degree of flocculation relies upon complicated small-scale turbulent, hydrodynamic, and physicochemical forcing (Milligan and Hill, 1998; Safak et al., 2013; Soulsby et al., 2013).

1.1 Field measurements of SSC and knowledge gaps

Field-based studies of sediment dynamics will typically obtain estimates of SSC using pump/bottled water samples, optical backscatter sensors (OBS) and acoustic backscatter sensors (ABS) (Wren et al., 2000). Each method of measuring SSC has strengths and shortcomings; for example, the direct collection of water samples in energetic coastal regions can prove logistically challenging. Additionally, the limited spatial and temporal coverage of intrusive water samples can make the determination of a representative value for a field site difficult, particularly for sites with significant variability in discharge flows and water-level conditions (Hamilton et al., 1998; Guerrero et al., 2017; Wren et al., 2000). Recent advances in indirect, automated, optical, and acoustic technology have improved the ability to effectively capture characteristics of suspended sediment loads (Guerrero et al., 2017). Optical sensors operate by emitting visible or infrared light into a water sample (Downing, 2006; Wren et al., 2000). Upon return, the scattered radiation captured by the OBS photodetector is linearly proportional to SSC, providing an indirect estimate of the characteristic. This relationship can be determined through a calibration with water samples collected adjacent to the sensor in the field (Downing, 2006; Hamilton et al., 1998), or by performing a laboratory calibra-

tion using sediment representative of the suspension at the field site (Nowacki and Ogston, 2013). For the laboratory approach, often a surface grab sample is used and in muddy environments, this sample is sieved to remove larger particles. In both scenarios, the water samples are taken at a known time and the particle mass concentration is determined by filtering to weigh the dry sediment weight of the water sediment mixture (Gray, 2000). Although OBS sensors allow for remote deployment and data logging, they are prone to reproducing false SSC gradients (Hamilton et al., 1998) because the data is from a single point measurement and does not cover the entire water column (Rai and Kumar, 2015; Thorne et al., 1991; Wren et al., 2000). Moreover, OBS instruments are susceptible to biological fouling and the scattering from suspended particulate matter is heavily dependent on particle size (Downing, 2006; Hamilton et al., 1998; Rai and Kumar, 2015; Wren et al., 2000). If the particle size is inconsistent across a measurement campaign as is the case in bi-modal, mixed mud/sand field sites and under flocculation or disaggregation, inaccurate estimate of SSC can be derived, with distorted values up to 100-fold (Downing, 2006; Eidam et al., 2022; Wren et al., 2000). A form of optical laser diffraction instrumentation is Laser In Situ Scattering and Transmissometry (LISST) sensors, which operate by collecting the intensity of the scattered light at different angles from a sample volume, across an array of concentric ring detectors (Fugate and Friedrichs, 2002; Styles, 2006; Wren et al., 2000). The refracted beam angle provides a diffraction pattern, which can be converted to estimates of particle size spectra and volume concentration over the measured size range. Use of point sampled, LISST sensors in estuarine environments comprised of varying particle aggregates or in density stratified water bodies is limited, as these components change the refractive index and forward scattering of the particles in suspension (Fugate and Friedrichs, 2002; Styles, 2006), thus impacting the measured particle size distribution and volume concentration estimates.

Acoustic technology offers the possibility of measuring in-situ vertical profiles of suspended sediment for depths of the order of several metres throughout the water by capturing the strength of the range-resolved backscattered pulse, an advantage over optical devices and direct sampling (Thorne and Hanes, 2002; Thorne and Hurther, 2014; Wren et al., 2000) which are limited to a single measurement location. Monostatic, multi frequency Acoustic backscatter sensors (ABS) in the range of 0.5 to 5 MHz, transmit a short ($\approx$10 μs) sound pulse which insonified sediment in suspension will reflect a portion of, to be received by the transducer, see Figure (1.1) (Thorne et al., 1991; Thorne and Buckingham, 2004; Thorne and Hanes, 2002). Published literature has highlighted the non-intrusive nature of ABS deployments that capture high spatial and temporal resolution profiles of SSC on the intra-wave, turbulent scale (Hamilton et al., 1998; Thorne and Hay, 2012; Thorne and Hurther, 2014; Wilson and Hay, 2015).

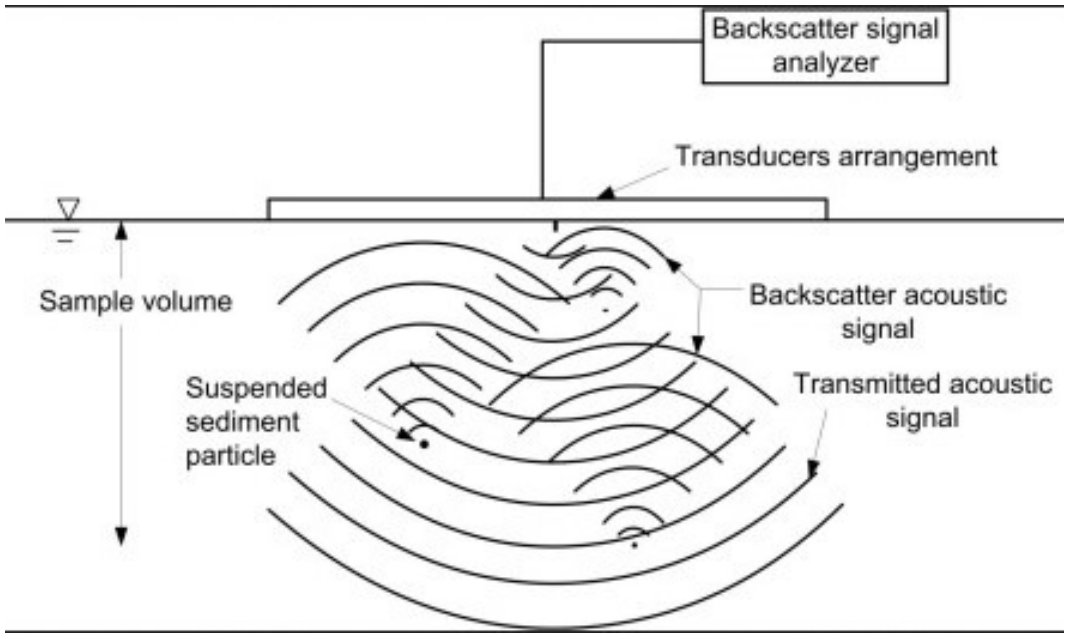

Figure 1.1: Diagram of acoustic backscatter pulse from suspended sediment particles of a sample volume. From Rai and Kumar (2015).

To obtain estimates of SSC from measured backscatter data an inversion

(Moate and Thorne, 2012; Thorne and Hurther, 2014; Thorne and Meral, 2008)) is required. To invert the measured ABS backscattered signal received from a suspension of scatterers, the scattering characteristics, the so-called form function (f_∞) and total scattering cross-section (Σ_s) of the suspended particles is required. The dimensionless form function (f_∞) and total scattering cross section (Σ_s) approximate respectively, the backscattering expected due to the geometrical size of the particle and the scattering received from all scattering angles of a particle, within a cross sectional area. For non-cohesive, regular shaped particles like quartz and glass spheres, there exists an established set of formulae for the scattering characteristic terms (Moate and Thorne, 2012; Thorne and Buckingham, 2004; Thorne and Meral, 2008) and this method has successfully been used to obtain measurements of unimodal particle concentrations along a vertical profile in sandy environments (Moate et al., 2016; Sahin et al., 2013; Thorne et al., 2009; O'Hara Murray et al., 2011). For irregularly shaped sand particles, analytical solutions for the acoustic scattering properties (f_∞ and Σ_s) have evolved to accommodate the difference in backscatter received from marine sand consisting of varyingly shaped mineral grains (Moate and Thorne, 2009, 2012, 2013; Thorne and Meral, 2008). However, for cohesive, irregular shaped sediments generalised as 'mud' which is the main substrate of estuaries globally (O'Laughlin et al., 2014; Soulsby et al., 2013; Thorne et al., 2021; Thrush et al., 2004), the scattering characteristics are currently unknown (Moate and Thorne, 2009, 2012). As a result, there is currently no sound theoretical interpretation of the ABS response to fine grained material, thereby impeding the discrete use of acoustic technology (Sahin et al., 2013; Thorne et al., 2014). Therefore, it is typical for in-situ OBS and LISST measurements, turbidity recordings or direct water samples to be gathered in conjunction with the ABS observations of the muddy suspension either in the field (Moore et al., 2012; Sahin et al., 2013) or in controlled laboratory studies (MacDonald et al., 2013). These water samples can then be used to calibrate and/or validate the SSC estimates obtained from the ABS.

Despite these difficulties, there have nonetheless been recent advancements in understanding of the scattering characteristics of flocculated sediment, through laboratory studies such as MacDonald et al. (2013), Thorne et al. (2014), and field work by Fromant et al. (2017), Vergne et al. (2020) and Thorne et al. (2021). A laboratory study by MacDonald et al. (2013) gathered ABS measurements of flocculating sediment and evaluated the scattering terms and compared values for f_∞ and Σ_s, derived from an elastic and fluid sphere model. A key finding was neither model exactly represented the scattering parameters of the generated kaolin flocs, rather the models provided upper and lower bounds for the terms as ultimately, the form function increased with the increasingly flocculated particles. In a theoretical analysis, Thorne et al. (2014) proposed a hybrid fluid model to accommodate unknown particles' scattering, constrained by the experimental data of MacDonald et al. (2013). The model accounted for the increased fluid interstices between the fractal entities of the porous floc clusters (Winterwerp et al., 2006). The model predictions for f_∞ and Σ_s agreed reasonably well with the measurements from MacDonald et al. (2013). However, both studies recommended further laboratory experiments to widen the parameter space and to improve theoretical understanding (MacDonald et al. (2013) and Thorne et al. (2014)). Since then, field studies like Fromant et al. (2017) aimed to extend this *a priori* model by evaluating f_∞ and Σ_s from in-situ multi-frequency ABS data. The authors used a LISST granulometer to determine an assumed mean porosity value over the total size range of low-density flocs studied. This value was used to invert backscatter observations by Fromant et al. (2017), and generated estimates of SSC which were consistent with values from the in-situ water samples. Vergne et al. (2020) conducted a field study across two experimental sites in a river cross section, with a low sediment load at one site, and a high sediment load at a second site. They inverted multi-frequency backscatter data from the heterogenous suspension, with some success, producing realistic SSC estimates when com-

pared to the SSC obtained from the water samples. However, the specifics of the instrument calibration and acoustic backscatter modelling were based on the water samples collected and the authors noted a lack of temporal variability in the suspension. In a numerical study by Thorne et al. (2021) of a bi-modal particle size distribution in an inter-tidal estuary, they investigated how the acoustically inverted SSC found in the water column was affected by using bed samples composed mainly of sand in the calibration phase. Across each of the scenarios modelled in the study with the suspension ultimately becoming muddier with height above the bed, when using the bed sediment samples the results tended to overestimate the suspended particle size and underestimate SSC, from what was in suspension.

The field studies emphasised the profiling ability of multi-frequency ABS systems to provide estimates of SSC in rivers and estuaries at high spatial and temporal resolutions (Fromant et al., 2017; Vergne et al., 2020) and information on the particle size (Vergne et al., 2020). Nonetheless many studies also recommended exercising caution in interpreting acoustic SSC data from cohesive sediment environments (Fromant et al., 2017; Thorne et al., 2021; Vergne et al., 2020). Above all, Fromant et al. (2017) and Vergne et al. (2020) expressed the argument for more research and field studies to answer further questions, such as how well the average porosity term derived from Fromant et al. (2017) would work for differentially composed, floc aggregations. Additionally, much more study is likely required to form the basis of a theoretical framework of the cohesive suspended sediment scattering properties, which would enable implementation in the field of ABS "stand-alone systems" (Fromant et al., 2017).

1.2 Aims of the present study

The objective of this study was to address the knowledge gap described above and to answer the research question:

Can laboratory-calibrated acoustic backscatter sensors (ABS) be applied to obtain accurate estimates of the scattering characteristics, which in-turn can be used to derive estimates of SSC profiles for cohesive particles in the field?

1.3 Thesis structure

- Chapter 2 details the underlying background and includes the relevant theoretical equations to describe the acoustic wave reflection.
- Chapter 3 describes the laboratory experiments used to calibrate the ABS, and methodology including data processing. Chapter 3 also includes a description of a field experiment which was undertaken to derive estimates of the scattering characteristics and in-turn ascertain the potential to invert ABS data to provide accurate SSC profiles.
- Results are presented in Chapter 4, with particular emphasis on the results obtained from the ABS calibration and the scattering characteristics derived from the field data.
- Findings are discussed and set into context of previous work in Chapter 5.

Finally, Chapter 6 concludes the thesis with a summary of the outcomes and suggestions for further research work.

Chapter 2

Theoretical Background

2.1 The speed of sound and attenuation of sound waves in water

As a pulse generated by the ABS propagates through the water column a proportion of the transmitted pulse is scattered back to the ABS by suspended particles in the water column. By "listening" at fixed time intervals after each transmitted pulse the ABS generates a profile of backscattered sound intensity. As distance and time are related via the speed of sound in water the "listening" times can convert into range or distance. The speed of sound (c) in water varies with several parameters, including temperature, salinity, and depth. Given this thesis focuses on shallow coastal waters, only the former two factors are considered. Sound speeds increase with both salinity and temperature as shown in Figure (2.1) (with values found using Mackenzie (1981) formula).

As sound propagates through water, it is attenuated with distance (α_w). To obtain estimates of SSC from the ABS inversion the attenuation losses must be accounted for. The rate of attenuation varies with frequency and temperature as shown in Figure (2.2) with greater attenuation at higher frequencies than lower frequencies. In addition, greater attenuation occurs at lower water tem-

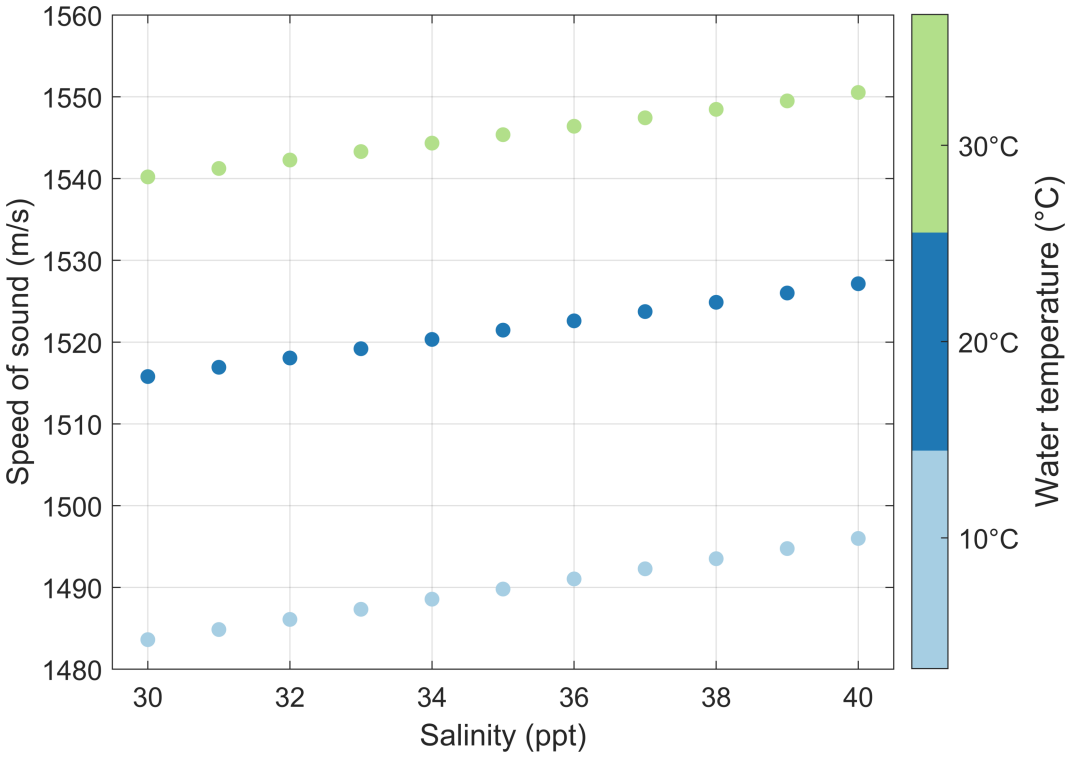

Figure 2.1: Speed of sound (m/s) (o) in water as a function of water temperature (10, 20, 30 C) and salinity (30 – 40 ppt) at a constant depth of 0 m.

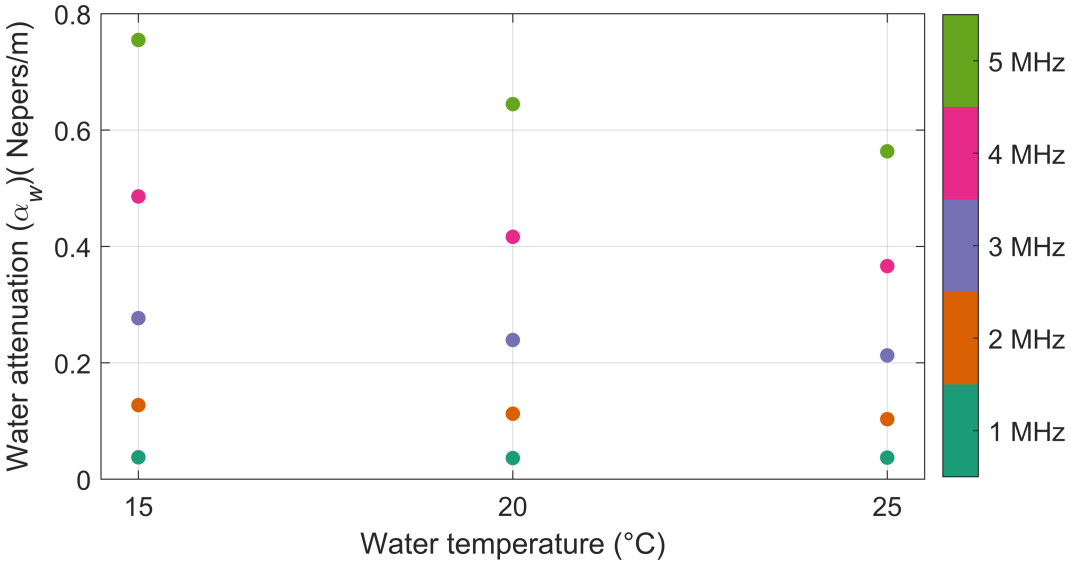

Figure 2.2: Water attenuation (α_w) (o) as a function of frequencies (corresponding to 1, 2, 3, 4, and 5 MHz) (colours) at a constant water temperature of 20°C, depth of 0 m, salinity of 25 ppt, pH of 8. Function to calculate water attenuation from Medwin and Clay (1998)

peratures, a trend applicable to understanding the water attenuation pattern over the diurnal cycle, where water temperatures are cooler during the night

versus daytime.

2.2 Introduction to acoustic backscatter

2.2.1 Scattering from a single particle

For a single spherical particle of radius (a) the measured backscattered amplitude in volts ($\hat{V}$) recorded by an ABS is given by (Wilson and Hay, 2017)

$$\hat{V} = K_{TR}\frac{f_{\infty}a}{2r^2}D^2e^{-2\alpha_w r}, \tag{2.1}$$

where K_{TR}, is the system constant, r is distance from the transducer, and D is the so-called transducer directivity which is defined as follows

$$\mathrm{D} = 2\frac{J_1\left(ka_t\sin\beta\right)}{ka_t\sin\beta}, \tag{2.2}$$

where β is the angle from the beam axis of symmetry, k is the wave number ($k = 2\pi f/c$), a_t is the transducer radius and J_1 is the first order cylindrical Bessel function (Abramowitz and Stegun, 2006; Wilson and Hay, 2017), with all other terms as previously defined. The above mentioned system parameters K_{TR}, is a measure of the transmit and receiver sensitivities of both the electronic circuits of the ABS and of the transducer (Rai and Kumar, 2015; Wilson and Hay, 2017). The directivity term D (Clay and Medwin, 1977), relates to the sensitively of the transducer to backscatter sound from various angles. Typically, both K_{TR} and a_t are obtained via a laboratory calibration.

An example illustration of a monostatic configured ABS sensor (Figure 2.3) showed the directivity of the beam is based on the backscatter of a transmitted sound wave from a single particle, relative to the axis of the acoustic beam.

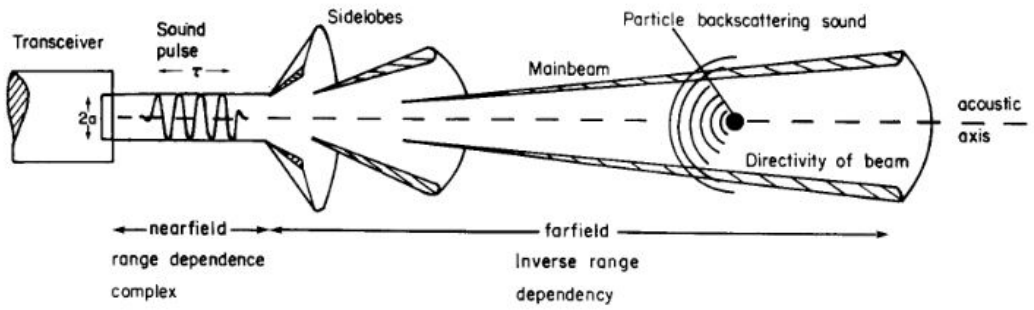

Figure 2.3: Acoustic pulse from a monostatic configured ABS device spread over the near field and far field regions, showing the backscattered sound from the particle in the acoustic beam axis. From Thorne et al. (1991).

2.2.2 Scattering from a suspension of particles

Equation (2.1) considered the case for the backscatter from a single particle. For a suspension of N spherical particles randomly distributed through a given sample volume of water, the ensemble-average backscatter in volts $\langle V^2 \rangle$ measured by the ABS is given by Wilson and Hay (2017)

$$\langle V^2 \rangle = K_{TR}^2 \frac{|f_\infty|^2 a^2}{4} \int_{r-c\tau/4}^{r+c\tau/4} \int_0^{2\pi} \int_0^{\pi} N D^4 \frac{e^{-4\alpha r}}{r^2} \sin(\beta) \mathrm{d}\beta \mathrm{d}\theta \mathrm{d}r, \tag{2.3}$$

where N is the number of particles per unit column, τ is the pulse duration in s, here α is the attenuation coefficient due to both water and sediment, such that α is given by

$$\alpha = \alpha_w + \frac{1}{r} \int_0^r N \frac{\Sigma_s}{2} \mathrm{d}r, \tag{2.4}$$

where $\Sigma_s(ka)$ is the total scattering cross-section (Wilson and Hay, 2017). Applying the commonly used assumption (Thorne and Hurther, 2014; Wilson and Hay, 2017) that the integrand in Equation (2.3) is slowly varying within $r \pm c\tau/4$, Equation (2.3) can be simplified to

$$\langle V^2 \rangle = K_{TR}^2 \frac{|f_\infty|^2 a^2}{4r^2} N e^{-4ar} \left[\frac{c\tau}{2} \right] \Psi, \tag{2.5}$$

where

$$\Psi = 2\pi \int D^4 \sin\beta \mathrm{d}\beta \approx 2\pi \left[\frac{0.96}{ka_t}\right]^2. \tag{2.6}$$

Here Ψ is the two-way equivalent beam angle (Equation 2.5). At this stage Equation (2.5) is cast in terms of N, noting that SSC (M) and N are related as

$$M = \frac{4\pi a^3 \rho_s \ N}{3} \tag{2.7}$$

where ρ_s is the density of the sediment, Equation (2.5) becomes

$$\left\langle V^2 \right\rangle^{1/2} = \frac{K}{r}\left[\frac{3c\tau M}{16\rho_s a}\right]^{1/2} |f_\infty| \, e^{-2\alpha r}, \tag{2.8}$$

where

$$K = K_{TR}\sqrt{\Psi/2\pi}. \tag{2.9}$$

Finally rearranging Equation (2.8) to make M the subject we obtain:

$$M = \frac{\langle V^2 \rangle \, 16\rho_s a r^2 e^{4\alpha r}}{3c\tau K^2 |f_\infty|^2}. \tag{2.10}$$

2.3 Inversion procedure to obtain suspended sediment concentration from acoustic backscatter

2.3.1 Iteration calculation

To solve Equation (2.10) in Section (2.2.1) to obtain estimates of M, i.e. the SSC profile, an iterative inversion processes is required. An iterative inversion

is required as M not only occurs on the left-hand-side of the equation but is also present on the right-hand-side in the sediment attenuation term (see Equation 2.4, note N and M are related via Equation 2.7).

In this study the inversion method outlined in Thorne and Hurther (2014) was adopted, which is summarised as follows. The first step in the inversion procedure is to obtain initial estimate of M by assuming (for now) that the attenuation due to sediment is zero, i.e. $\alpha_s = 0$, let this initial estimate be called M_0, which is given by

$$M_0 = \left[\frac{16\rho_s a}{3c\tau}\right] \frac{(r\Phi)^2}{k^2 f_\infty^2} e^{4\alpha_w \omega r} \left\langle V^2 \right\rangle^{1/2}. \tag{2.11}$$

Using Equation (2.10) an improved estimate of M can be obtained as

$$M_1 = M_0 e^{4\alpha_{s0}} \tag{2.12}$$

where α_s is the sediment attenuation calculated using the SSC M_0. The equation above can be generalized such that,

$$M_{i+1} = M_0 e^{4\alpha_{si}}. \tag{2.13}$$

Where α_{si} is the sediment attenuation calculated using the SSC estimate Mi. The above equation is iterated until convergence is achieved, i.e., the differences between M_{i+1} and M_i becomes small enough and satisfy some user defined convergence criteria. In this study convergence was deemed to occur when

$$\left| \frac{M_{i+1} - M_i}{M_{i+1}} \right| < 0.0001 \tag{2.14}$$

The above-mentioned inversion procedure is first applied to the very first range bin, and then applied to the next bin accounting for the sediment attenuation that occurs in the first bin. This procedure is repeated throughout the entire

$\langle V^2 \rangle$ profile accounting for the sediment attenuation that occurs in all previous bins.

The inversion relies on amongst other things the specification of the system constant K_{TR} and the scattering characteristics (f_∞ and Σ_s), the following sections outline how estimates for these terms can be derived.

2.4 ABS calibration

In this section, we describe two calibration methods that can be used to calibrate an ABS: Firstly, using a single particle to obtain K_{TR} and a_t, and secondly using a suspension of particles.

2.4.1 System calibration from a single sphere

In Section (2.2) we presented Equation (2.1) which describes the scattering from a single particle. Rearranging that equation yields

$$K_{TR} = \frac{\hat{V} 2r^2}{f_\infty a D^2} e^{2\alpha_w r}. \tag{2.15}$$

Now consider using an ABS to the measure the acoustic backscatter signal ($\hat{V}$) from a single particle of radius a place directly inline of the ABS transducer (D=1) at a known distance of r. Now, should the form function f_∞ of the that single particle be known then all the terms on the right-hand-side of the above equation would be known and K_{TR} is easily calculated.

For a tungsten carbide ball of radius a suspended in water, there is a known and definite analytical scattering series solution for the f_∞ (Hickling, 1964). The response of sound hitting a single spherical target can be split into two components (and hence different form functions): (1) an initial return data due to the immediate scattering off the front face of the sphere (the so-called

rigid response), and (2) the resonant backscatter signals received later in time, indicative of the elastic waves travelling internally within, or circumferentially around, the sphere (the so-called elastic response). Figure (2.4) illustrates the two forms of acoustic backscatter response from a tungsten carbide sphere, differentiated into the two scattering regimes.

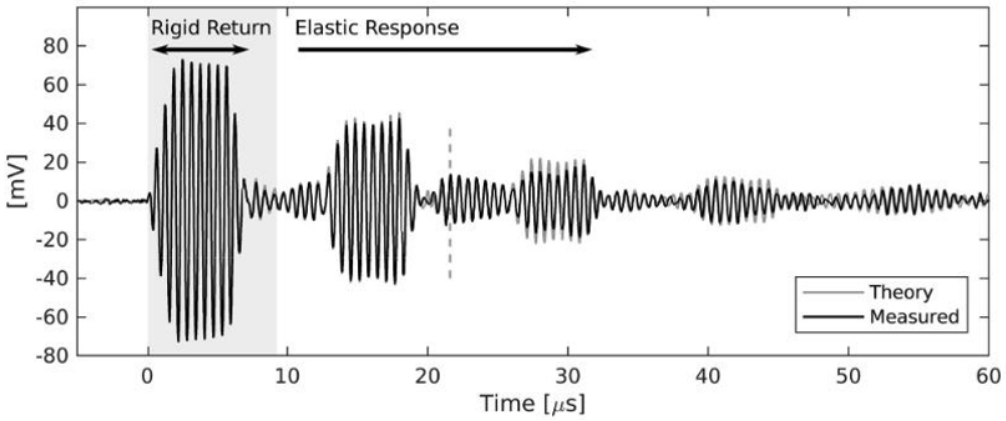

Figure 2.4: Time series of measured (black) and computed (grey) backscatter received ABS from a 16 mm diameter tungsten carbide sphere. From Wilson and Hay (2017).

As shown by (Wilson and Hay, 2017), utilizing the rigid response from the tungsten carbide sphere and corresponding analytical solution for the rigid-response f_∞ (shown in Figure 2.5) provides an ideal method for the calibration of acoustic backscatter systems. To ensure separation of the rigid response from the elastic response the following criteria must be met

$$\tau < \frac{\pi d}{c_t} \tag{2.16}$$

where, d is particle diameter and c_t is the longitudinal wave speed.

In addition to calculating K_{TR}, a single particle can also be used to determine the effective transducer radius (needed to calculate D). Consider the case in which the location of the single particle is moved in a direction perpendicular to the central beam axis. By measuring $\hat{V}$ at known angles (β) from the central

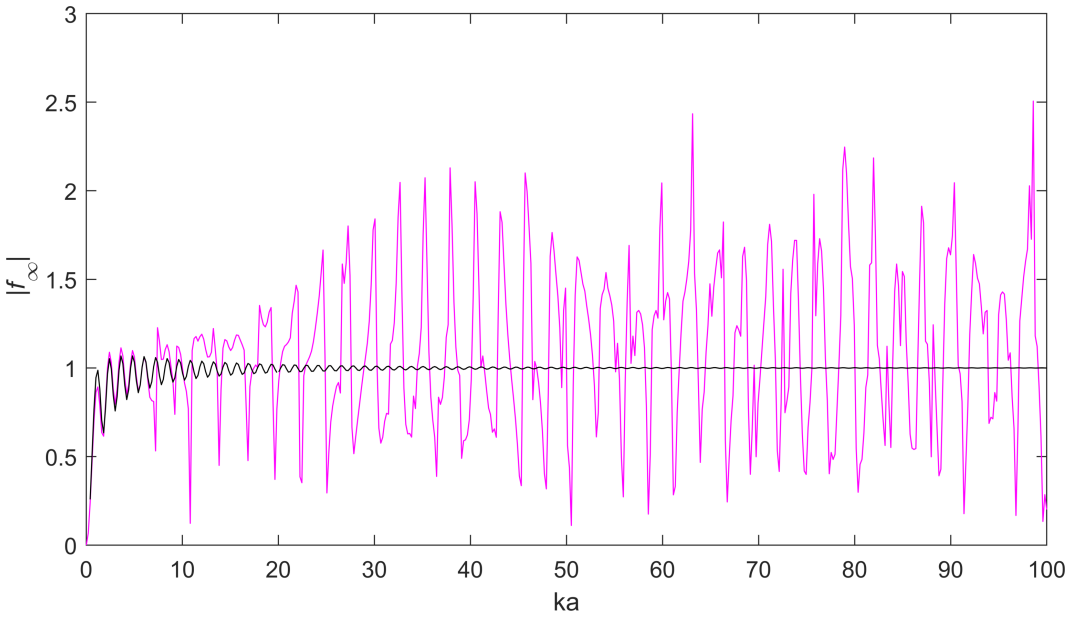

Figure 2.5: Theoretical backscatter form function f_∞ for a solid tungsten carbide ball in water for (1) the rigid response (black) and (2) the elastic response (pink).

beam axis the directivity of the transducer can be mapped (measured). Then using a_t as a fitting parameter, the analytical expression for D (Equation 2.2) can be optimized to best match the measured directivity pattern, with the optimal solution yielding a_t.

2.4.2 System calibration from a particle suspension

The system parameter K_{TR} can also be determined from the scattering from a uniform suspension of particles of known f_∞ and Σ_s (Betteridge et al., 2008). For example, glass spheres are often deemed suitable given the sphericity and uniformity of such particles (Betteridge et al., 2008; Moate and Thorne, 2009). Using glass beads sieved into $(1/4)\phi$ intervals ($\phi = -\log_2(d)$), where d is the particle diameter in mm) Moate and Thorne (2012) and Vergne et al. (2020) have successfully applied the calibration procedure of Betteridge et al. (2008). Sieving the glass beads into $(1/4)\phi$ intervals greatly simplifies the expressions for both f_∞ and Σ_s, which for a suspension of glass beads sieved into $(1/4)\phi$ intervals are given by (Betteridge et al., 2008)

$$|f_\infty| = \frac{\varsigma x^2}{1.17 + 0.95x^2} \tag{2.17}$$

$$\begin{aligned}\varsigma = &\left(1 - 0.5\mathrm{e}^{-[(x-1.5)/0.5]^2}\right)\left(1 + 0.4\mathrm{e}^{-[(x-1.5)/3.0]^2}\right) \\ &\times \left(1 - 0.5\mathrm{e}^{-[(x-5.9)/0.7]^2}\right),\end{aligned} \tag{2.18}$$

$$\Sigma_s = \chi 2\pi a^2 \tag{2.19}$$

$$\chi = \frac{0.24\varphi x^4}{0.7 + 0.3x + 2.1x^2 - 0.7x^3 + 0.3x^4} \tag{2.20}$$

$$\varphi = 1 - 0.4e^{-\left((x-5.5/2.5)^2\right)} \tag{2.21}$$

where $x = ka$. Rearranging Equation (2.8) and substitution of Equation (2.9), yields

$$K_{TR} = \frac{r\left\langle V^2\right\rangle^{1/2}}{\sqrt{\psi/2\pi}\,|f_\infty|}\left[\frac{16\rho_s a}{3c\tau M}\right]^{1/2} e^{2\alpha r}. \tag{2.22}$$

Now consider using the ABS to the measure the acoustic backscatter profile of $\langle V^2\rangle$ from a homogeneous suspension of a glass beads of a known concentration M, density ($\rho_s = 2500\,\mathrm{kg/m^3}$) and size ($a$, $(1/4)\phi$ sieved). Using the expressions for f_∞ and Σ_s, all the terms on the right-hand-side of the above equation are know and K_{TR} can be easily calculated. In comparison to the single particle calibration (Section 2.4.1) which results in a single estimate for K_{TR}, for a suspension of particles, a profile of K_{TR} is obtained. However, all going well the K_{TR} profile should be constant with range, and therefore well represented by an average value.

2.5 Obtained estimate for f_∞ and Σ_s from ABS data characteristics

For a suspension of particles for which the f_∞ and Σ_s are unknown (as is the case for a suspension of flocculated particles measured in the field), the f_∞ and Σ_s can be obtained empirically from the measurement backscatter data as follows. Multiplying both sides of Equation (2.8) by range r, taking the natural logarithm, and rearranging yields the following linear function of r:

$$\ln\left(r\langle V^2\rangle^{1/2}\right) = -2\alpha r + \ln\left(K\gamma\left|f_\infty\right|\right), \tag{2.23}$$

where

$$\gamma = \left(\frac{3c\tau M}{16\rho_s a}\right)^{1/2} \tag{2.24}$$

and

$$-2\alpha r = \ln\left(e^{-2\alpha r}\right). \tag{2.25}$$

We can undertake a linear fit to the data (measured voltages and ranges) arranged in the form given in Equation (2.23), to obtain the gradient m, and $y-$intercept (c), where

$$m = -2\alpha r \tag{2.26}$$

and

$$c = \ln\left(K\gamma\left|f_\infty\right|\right) \tag{2.27}$$

Equation (2.27) can be rearranged to yield

$$|f_\infty| = \frac{e^c}{K\gamma}, \tag{2.28}$$

noting that γ includes the mass concentration. Substituting the coefficients for the sound attenuation $\alpha = \alpha_s + \alpha_w$ into (2.25) yields

$$m = -2\alpha_s - 2\alpha_w \tag{2.29}$$

in which

$$\alpha_s = \frac{N\Sigma_s}{2}, \tag{2.30}$$

where Σ_s is the total scattering cross-section. Substituting Equation (2.30) into Equation (2.29), finally yields

$$\Sigma_s = \frac{-m - 2\alpha_w}{N}. \tag{2.31}$$

Therefore by calculating the slope and intercept of r versus, $\ln\left(r\langle V^2\rangle^{1/2}\right)$ it is possible to derive estimates of f_∞ and Σ_s. A limitation of this approach is that M must be know and be approximately constant over the range of r values used in the fit. Furthermore, a and ρ_s must also be known so that relationship between M and N can be established (see Equation 2.7).

Chapter 3

Laboratory and field methodology

3.1 Introduction

Using the theoretical background above, two different laboratory experiments were undertaken to determine the unknown calibration constants for two specific acoustic backscatter (ABS) instruments – each of which had four transducers of different frequencies, which were then deployed in a field setting. The laboratory equipment, methodology and data analysis used are described first, followed by a description of the field experiments.

3.2 ABS calibration using a single sphere

3.2.1 Laboratory apparatus

Following Wilson and Hay (2017), experiments were conducted to obtain the system constant K_{TR} and effective transducer radius a_t for two Aquatec AQUAscat1000 Acoustic backscatter sensors (hereafter denoted instrument A (serial number ABS910_170) and instrument B (serial number ABS910_043)). Each AQUAscat system could select up to five transducers (although only 4 could be used at any one time) of different acoustic frequencies ranging from

1−5 MHz which were each calibrated individually (eight transducers in total). The first set up for the preliminary trial experiments, used a transducer mounted in a horizontal plane opposite a tungsten carbide ball in a glass tank displayed in Figure (3.1).

The main set of experiments (for the single particle calibration) were conducted in a larger DOLAV 800 solid 500 L tank of internal dimensions 1120 (L) x 720 (W) x 600 (H) mm: (Figure 3.2). The change to the bigger tank ensured sufficient separation of the near field/far field along the acoustic beam (Thorne et al., 1991).

In each case the tank was filled to within 1 cm of the total depth of the tank with distilled water. A 24−hr period allowed for adequate resting time for air bubbles to disappear prior to undertaking the experiments. When not in use, the tank remained sealed by a lid to reduce contamination, for example by dust particles. For each experiment, the water temperature was measured and remained within the 18−19 °C range.

For the main calibration experimentation, a single acoustic transducer was mounted horizontally in a fixed location and the electronic ABS housing was placed outside of the tank Figure (3.2). On the opposite side of the tank a 16 mm tungsten carbide ball was mounted to a horizontal rod of length 100 mm (3 mm diameter), and then secured by a vertical rod (527 mm tall) (3 mm diameter) to a UNISENSE 3D Motorised Micromanipulator, consisting of three motor controllers connected to three motorised arms (x, y, and z directions).

3.2.2 Experimental procedure

For all experiments using the DOLAV tank, the distance from the transducer to the tungsten ball was approximately 58 cm, well within the far field of the

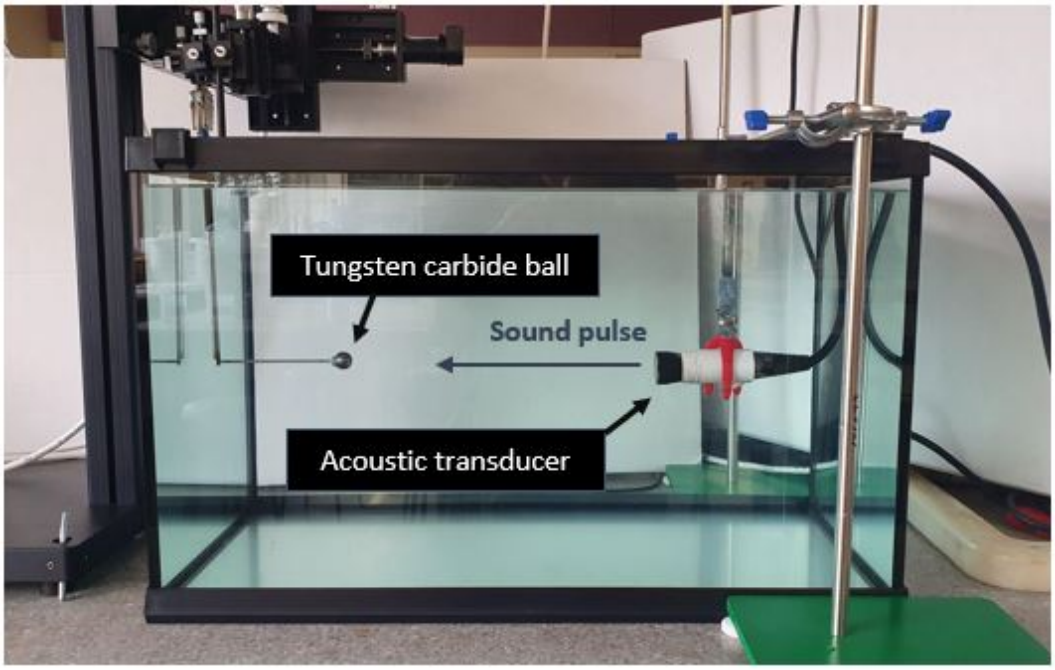

Figure 3.1: Photograph of tank set-up for the preliminary experiment. In this case a 3 MHz transducer was mounted 15 cm from back tank wall, at around a 17 cm depth and width. The tungsten carbide ball was 13.2 cm out from the adjacent tank wall. The range between the transducer to ball was 28.2 cm. The approximate split between the near field/far field term was at 20 cm from the transducer face.

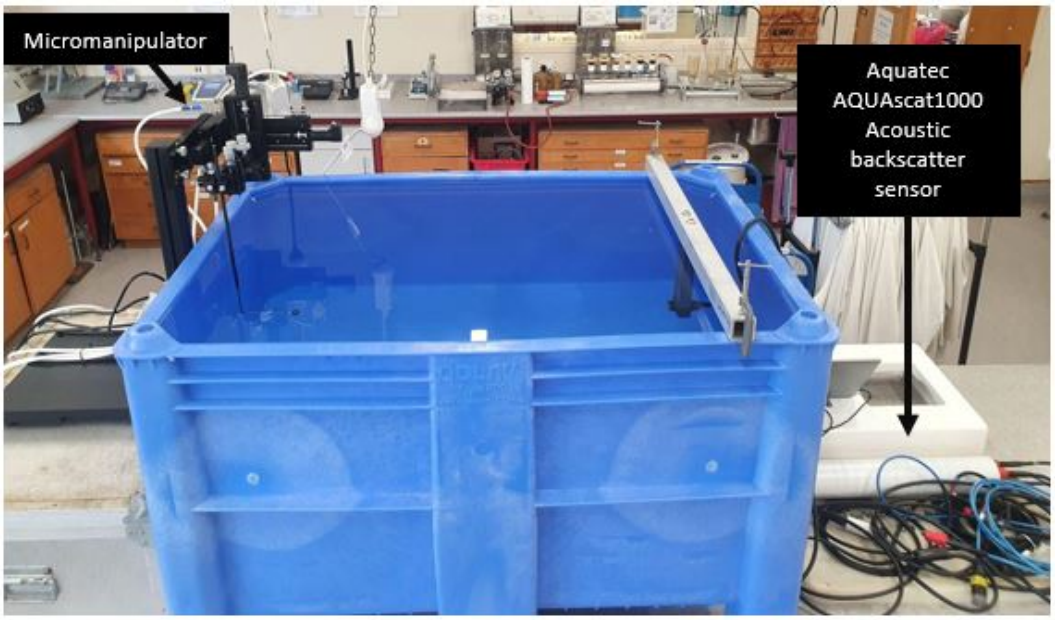

Figure 3.2: Side view of experimental set-up in laboratory with plastic DOLAV 500 L tank, instrument B, 2 MHz transducer inside tank and gear attached for the tungsten carbide ball calibration experiments.

transducers. ABS data was collected along a profile of length 64.25 cm with a bin resolution of 2.5 mm (256 bins total). The ABS sampling was 1 profile per average taken at a profiling rate of 4 Hz, amounting to a total number of 28760 stored profiles. With this setup, the ABS had a pulse duration (τ) of 3.3 μs, which was less than the 12 μs required to satisfy the criteria of Equation (2.16) (Wilson and Hay, 2017) for separable 'rigid' return and elastic responses. The planar faces of the individual transducers were aligned manually with the centre of the tungsten carbide ball target Figure (3.2). The tungsten carbide ball was then moved using the micromanipulator to traverse a 50 mm grid in both lateral (across-tank) and vertical directions, with a step resolution of 2.5 mm in both directions. The target was held in each position for 60 s and a single experiment of data collection across the full grid took approximately 10 hrs. The precise positioning of the tungsten ball allowed for identification of the location of beam axis of symmetry (β=0).

3.3 ABS calibration using a suspension of particles

These experiments were conducted in a freshwater recirculation tank with dimensions 1000 (L) x 400 (W) x 400 (H) mm equating to a tank volume of 165 L shown in Figure (3.3). Acoustic transducers were mounted at the opening from the top of the tank. The ABS devices sampled at 8 Hz for bursts of 2 minutes and 50 s within a 3 min interval. The ABS signals had a pulse duration of 3.3 μs. The bin width or transmitted pulse length was 2.5 mm over a full tank range of 0.64 m. 12 mins of backscatter data were collected from the clear water tank (i.e., without any beads). Subsequently a homogeneous suspension of particles was created. To do this 58.610 g of glass ballotini (beads) which had been sieved through a size range of 75 to 90 μm ($(1/4)\phi$) was added to the tank. The midpoint of the size aperture range of 45.7 μm, was used in subsequent calculations as the representative particle size

for the distribution of glass beads in suspension.

Figure 3.3: Laboratory experimental set-up of tank with linked ABS device for ballotini bead suspension experiments: a) front view with single 3MHz transducer mounted (B) b) side view with grouping of 1, 2, 2.5 and 4 MHz transducers mounted (A).

A recirculating pump located on the tank bottom ensured particles remained in suspension and well-mixed throughout the tank. Water samples (420, 442 and 552 ml) were collected through a tube located at mid-depth of the tank at the start of the experiment, approximately halfway through the experiment at 40 minutes, and at the end at 75 minutes. Laboratory filtering and gravimetric analysis was used to determine the concentration in the water samples. In

each case, the known volume of sample was filtered through Whatman glass microfibre filter papers which had been pre-washed and dried for approximately two hours at 105 °C. Drying was repeated overnight at 105 °C and the difference between the pre and post filtering weights of the filter paper represented the mass amount present in each water sample. The masses were converted into mg/L and the average of the three water sample concentrations determined. This final average value was used as the nominal concentration amount in solution, across all glass bead experiments.

3.4 Data processing for the laboratory calibration experiments

The ABS data was post-processed in Matlab. For the tungsten carbide ball grid routine, the position of the ball with timestamp was provided (relative to an arbitrary origin) from the files output from the micromanipulator software (SensorTrace Suite). The profiles of ABS data were averaged over the times the ball was stationary at each location (∼30 s).

For the tungsten ball laboratory experiments, the bin measuring the earliest received, maximum ABS return was located and identified as the ABS 'rigid return' signal. The measured maximum backscatter $\hat{V}$, D^2=1 (D=1, as the measured maximum backscatter occurs directly inline of the transducer (i.e. β=0)), and other known parameters including α_w, f_∞ were substituted into Equation (2.1) to find K_{TR} of each transducer (instruments A and B). In determining f_∞ the leading 240 terms in the series solution were used (Hickling, 1964).

The backscatter data was then used to determine a_t via the directivity Equation (2.2.1). To do this, the ABS return at each location was normalized by the maximum value to yield measured values for D. The measured values of

D were plotted as a function of the angle (β) of the ball relative to the transducer beam axis. Using this normalized data and corresponding β values, a_t (Section 2.2.1) was found by minimizing the differences between the predicted D (Equation 2.2) and the measured D.

To validate the K_{TR} results from the tungsten carbide ball sphere experiments, the acoustic backscatter was measured from a suspension of glass ballotini beads for each transducer of instrument A and B. The background noise ABS signal and glass bead suspension experiment ABS measurements were both burst-averaged to provide a a profile of ensemble averaged ABS voltages $\langle V^2 \rangle^{1/2}$, which was used in Equation (2.8) (Section 2.4.2). Analysis was undertaken on the profile at a range of 0.4 m through to the end of the profile at 0.64 m, to avoid the near-field zone that occurs close to the transducer. The suspension field in the tank was assumed to be homogeneous, which previous (unpublished) use of the tank showed it to be the case. $\langle V^2 \rangle^{1/2}$, M, f_∞ (Equation 2.28), Σ_s (Equation 2.31), r, c, τ, alongside the assumed ρ_s, and a, was fed into Equation (2.22) to yield K_{TR} as a function of range. After generating estimates of K_{TR} as a function of range for the glass bead suspension experiments, the mean K_{TR} was calculated.

3.5 Field site

The field experiment took place from the 5^{th} of November 2021 to the 9^{th} of November 2021. The field site was the mudflat just seaward of the mangrove forest located at the southern end of the Firth of Thames, in the North Island of New Zealand (Figure 3.4).

3.5.1 Experimental apparatus and measurements

Multiple instruments were deployed as part of a broader study (Table 3.1), although the present thesis only presents data from a subset of the instru-

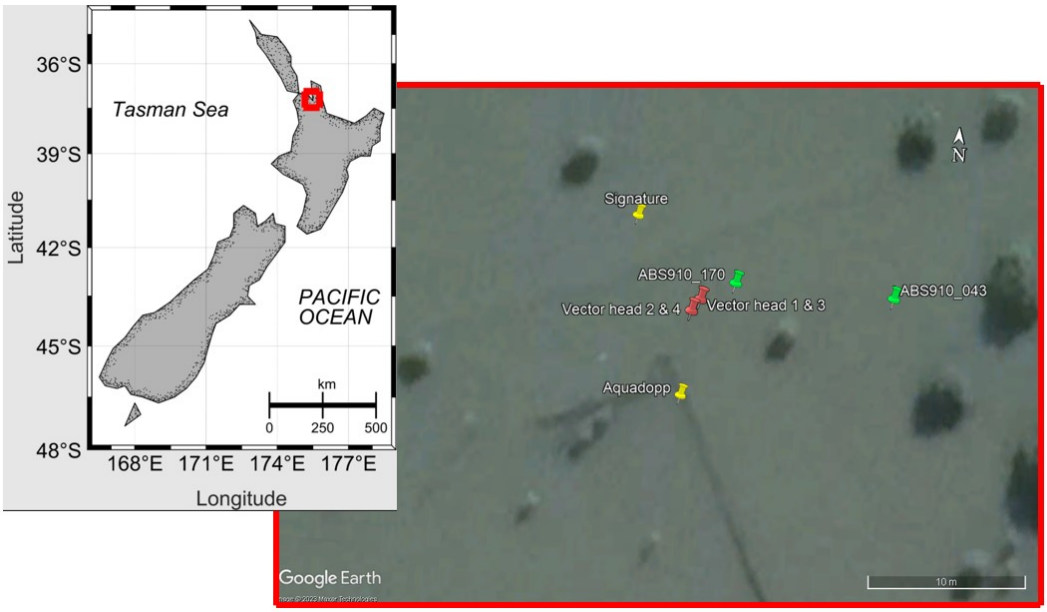

Figure 3.4: Field site location pinpointed in the Firth of Thames, North Island of New Zealand as highlighted in red. Instrument deployment at field site included (Google Earth Pro, 2023).

ments. A steel frame housed a vertical stack of four acoustic doppler velocimeters (Nortek vectors), four optical backscatter sensors (Campbell Scientific OBS3+), and four water sampling tubes. The Nortek vectors recorded the instantaneous velocity and pressure fields whilst the OBS measured the optical backscatter voltage, which was in-turn used to estimate SSC. The water sample tubes were co-located with the OBS sensors on the frame and were set to the same heights as the sampling volume of the ADVs approximately 0.15 m below the head. The frame was deployed using a retractable cantilevered, boom bridge from a sidearm of a permanent boardwalk, so minimal disturbance of the bed sediments occurred during deployment.

The frame was a few metres away from the main boardwalk. One of the two AQUAscat1000 ABS instruments (A) was deployed next to the other frame on the seabed with the transducers looking upward towards the water surface. The other ABS device (B) was mounted on a floating steel frame with all transducers pointed down towards the sea floor, located several metres further away

from the right-hand side of the main boardwalk arm. Both ABS instruments were deployed to capture acoustic backscatter data of the field sediment, using frequencies within the range of $1-5$ MHz. Water samples were collected from the tubes on the fixed steel frame as well as bed sediment samples taken to determine bed-sediment grain size in the laboratory. This water sample collection was in support of validating the SSC estimates derived from the OBS data. The data gathered from the OBS and the velocity data from the Nortek vectors was not processed as part of this thesis. Additionally, two acoustic Doppler current profilers (a Nortek Signature and Nortek Aquadopp) were deployed to provide additional flow information; however, the data are not used in this thesis.

3.5.2 Field ABS data quality control and processing

ABS data was collected in burst, with an interval between burst of 600 s (10 mins). The ABS' sampling frequency was 16 Hz for ABS instrument A and B, in total 9440 pings (individual profiles) were collected, which is equivalent to a burst length of 9 mins and 50 s with a 10 s off interval. Backscatter profiles were provided at 1 Hz (an average from 16 pings) and later further averaged over the entire burst. From this point on, all ABS data is presented in terms of the burst-averaged quantities, that is an average of 9440 individual profiles. ABS data was collected with a bin resolution of 10 mm (240 bins total). Given the ABS data was collected over six tidal cycles, the times of ABS data sampling are referred to by tides 1, 2, 3, 4, 5, and 6.

The ABS burst where instrument A and B were out of the water during low tide was removed for the analysis. In addition to the out of water bursts, the ABS data for instrument A were removed when the bin location exceeded the water depth and the data from beyond where the bed bottom was detected, for instrument B. These range intervals were determined by identifying the break in the slope of backscatter. The ABS data was squared and the mean signal

Table 3.1: Instrument details and specifications from the field site, with instrument locations pinpointed in Figure 3.4 according to colour/symbol. HAB = Height above bed.

Colour/symbol	Instrument	Sampling frequency	HAB (m)
Red	Vector head	16 Hz	0.24
	Pressure sensor	16 Hz	0.39
	OBS	16 Hz	0.09
	Sample tube		0.09
Red	Vector head	16 Hz	0.35
	Pressure sensor	16 Hz	0.32
	OBS	16 Hz	0.20
	Sample tube		0.20
Red	Vector head	16 Hz	0.55
	Pressure sensor	16 Hz	0.795
	OBS	16 Hz	0.40
	Sample tube		0.40
Red	Vector head	16 Hz	0.91
	Pressure sensor	16 Hz	0.81
	OBS	16 Hz	0.76
	Sample tube		0.76
Yellow	Nortek Signature	4 Hz	
	Nortek Aquadopp	1 Hz	0.08
Green	ABS (A) [upward looking]:	16 Hz	0.135
	1, 2, 4, & 5 MHz		
	ABS (B) [downward looking]:	16 Hz	1 – 1.2
	1, 2, 3 & 4 MHz		

calculated, the square root of this mean value was taken, giving the root mean square voltage $\langle V^2 \rangle^{1/2}$. Spikes in the ABS data were discarded by removing values that were $> 1.5\times$ the standard deviation from the mean value for the range bin.

Chapter 4

Results

4.1 Introduction

Presented first are the results from the laboratory calibration experiments with the tungsten carbide ball target which yielded values for the ABS system parameters (K_{TR} and a_t). Then, the equivalent results for the glass bead suspension experiments are presented. Finally, the system values from the calibration experiments are used in corporation with the field data from the ABS instruments, to provide estimates of the f_∞ and Σ_s. Lastly, using the f_∞ and Σ_s values derived above and the results from the ABS calibration, the ABS data was inverted to provide estimates of the SSC profile, which is then compared to the estimates derived from the OBS.

4.2 Acoustic backscattering from a single sphere

4.2.1 Rigid response vs elastic response

Figure (4.1) shows an example of the acoustic backscatter collected from the 5 MHz transducer for instrument A, from the tungsten carbide ball calibration. Two consecutive bin backscatter profiles are displayed in each panel in Figure

(4.1), with sixteen bins in total delineating the recorded ABS response corresponding to a range of 0.5686 to 0.6056 m. Each line shows the time series of backscatter, with maximum values in each case corresponding to the time when the acoustic beam was directly aligned with the tungsten ball target. Initially (range 0.5686 to 0.5760 m), was close to '0' return signal registered by the transducer indicating the acoustic pulse had not yet reached the target. In Figure (4.1), bin 236 (0.5809 m) captured the earliest received sound wave reflection by the rigid sphere coinciding with the peak acoustic signal representative of the 'rigid return' (noting this distance also corresponded to the measured distance between the front of the ball and transducer face). The lower return from the sequential bins (bins 237 and 238, ranges 0.5933 to 0.6056 m) bins indicated the 'rigid' peak die off; however, another significant peak was observed in bin 240 indicating the elastic response received by the transducer (similar to the peaks around 14-18 μs in Figure (2.4). The variable (but lower) backscatters received from the subsequent bins corresponded to the resonant backscatter reflections, after travelling around the tungsten ball, reaching the back wall of the tank, and returning to the transducer. From the analysis separating the rigid return versus the elastic response phases, the maximum ABS response was used in Equation (2.1) (Section 2.2.1) and was determined from the bins considered as part of the 'rigid return' regime. As a result, the $\hat{V}$ inputted in the theoretical calculation was consistent with rigid response form-function (black line in Figure 2.5).

Each of the transducer experiments (instrument A and instrument B) obtained time series such that shown in Figure (4.1), these are presented in Appendix A. The overall shape of the measured ABS signals across the range of bins depicted in Figure (4.1) was due to the changing lateral and vertical movements of the ball, in the competed grid scheme. Figure (4.2) is a magnified view of the acoustic backscatter from the single rigid response bin i.e., bin 236 from Figure (4.1), where the increasing and decreasing trend per peak in backscat-

ter corresponded to the vertical movements of the ball, whilst the horizontal oscillations signified movements in the lateral direction, throughout alignment with the transducer beam.

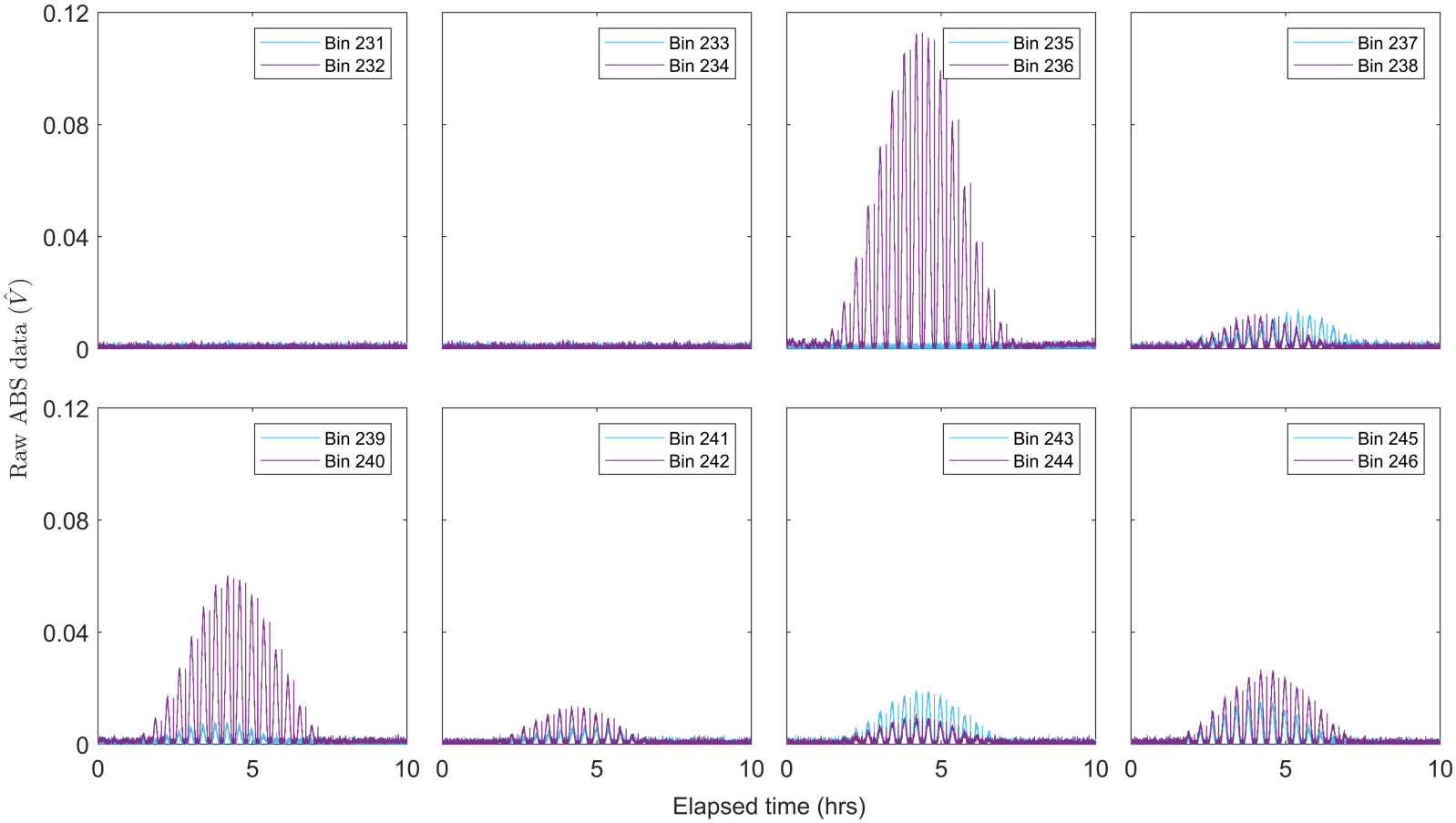

Figure 4.1: Time series of the received raw, ABS signal ($\hat{V}$) for the 5 MHz transducer of instrument A from the tungsten ball laboratory experiments. Each panel displays ABS data from two consecutive bins across a sixteen-bin range, starting at bin 231 and finishing at bin 246. The 'rigid' backscatter return from the tungsten ball was captured in bin 236 versus the elastic backscatter signals to follow, as shown in the subsequent bins.

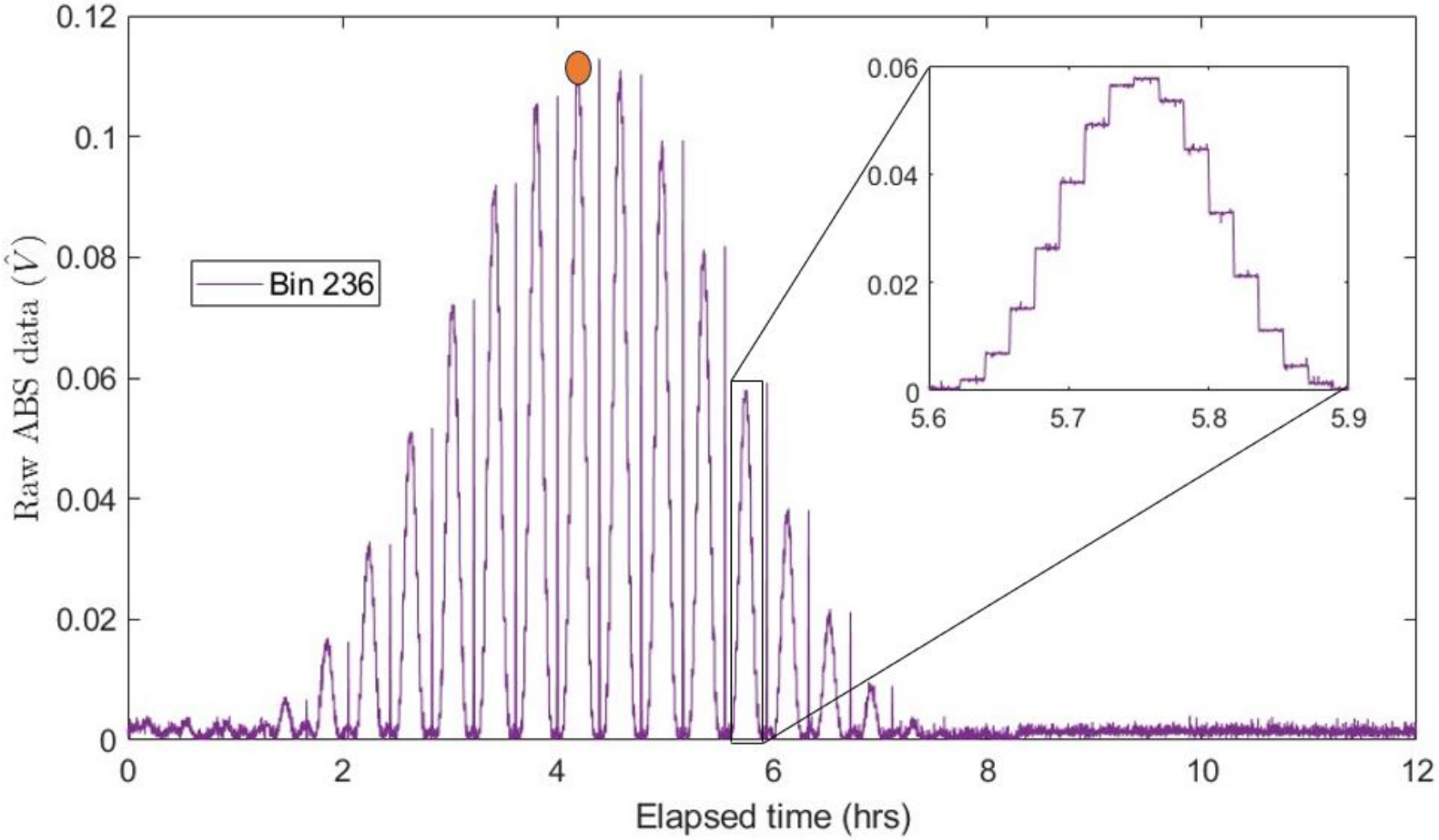

Figure 4.2: The raw ABS data ($\hat{V}$) correlating with lateral and vertical grid movements from bin 236 for 5 MHz (A), identified as the 'rigid' return peak bin.

4.2.2 a_t and K_{TR} results

An example of the pattern of backscatter recorded by the ABS as the tungsten ball was moved through the 50 mm square, lateral and vertical grid from bin 236, is shown in Figure (4.3) (for the 5 MHz transducer, instrument A). The colour bar shows the average acoustic backscatter response as a function of position (relative to an arbitrary grid origin position). In this case, the maximum return of 0.11 $\langle \hat{V} \rangle$ indicated this position corresponded to alignment with the central beam axis.

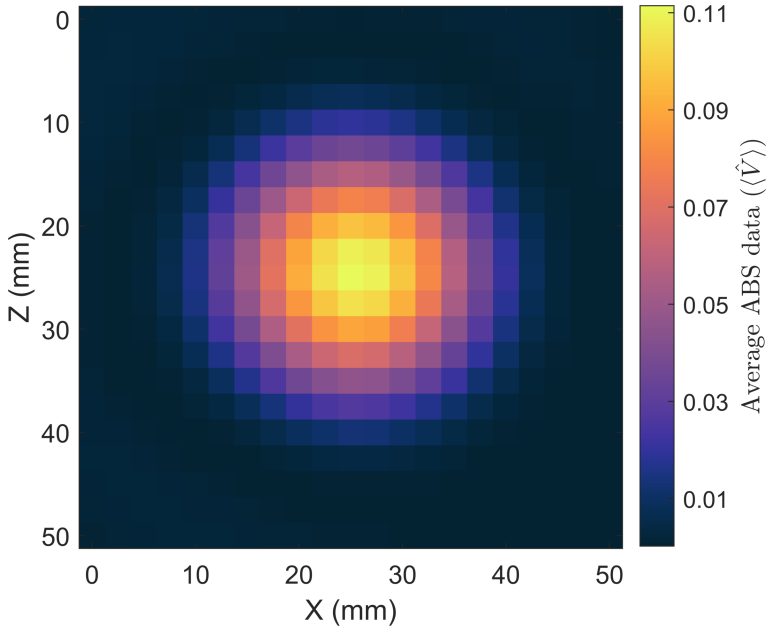

Figure 4.3: Grid cross section of ABS data ($\langle \hat{V} \rangle$) showing maximum backscatter from bin 236 for 5 MHz transducer (instrument A) from the tungsten ball experiments. Each point is an average of the backscatter over 30 s from each location at which the ball was stationary. Note the origin is arbitrary.

The raw ABS data for 5 MHz (instrument A) from the single bin (bin number = 236, range = 0.5809 m) (Figure 4.2) is shown in Figure (4.4a) as a function of position, the ABS data shown here is a location average (i.e. an average of the ABS data record while the ball was stationary). The location-averaged ABS return (orange points) shown in Figure (4.4b) is accordant with distance along the traverse from the central, maximum return. The orange dots in Fig-

ure (4.4b) were then normalized by the maximum ABS return i.e., $\hat{V}_{max}$ and then plotted, as a function of the angle from the beam axis (i.e., β), the result of which is shown in Figure (4.4c). From Figure (4.4c) it is evident that the response of the transducer is highly sensitive to the angle in which the sound comes from.

As discussed in Section (2.2.1), Equation (2.2) was then fitted to the data shown in Figure (4.4c) by using an iterative procedure (to find a_t), which minimised the sum of squared errors (SSE) between observations (i.e. the orange dots shown in Figure 4.4c) and the theoretical expression (Equation 2.2). In this example, fitting yielded $a_t = 6.2\,\text{mm}$. The ABS observations (orange dots) corresponded well to the predictive theoretical, D expression (black line in Figure (4.4c), a trend which was reflected across all the transducers that were calibrated. The calculated SSE for each fit of D for all transducers are provided in Table (4.1), which also indicates a close agreement between observed and predicted. The calculated a_t values are provided in Table (4.2).

Table 4.1: Calculated sum of squared errors (SSE) for each fit of measured D against theoretical D term for each transducer of instruments A and B, from the tungsten carbide ball laboratory experiments.

Calculated sum of squared errors (SSE)						
Transducers	1 MHz	2 MHz	2.5 MHz	3 MHz	4 MHz	5 MHz
ABS910_170	0.0029	0.00033603	0.0090	Not in use	0.0019	0.0037
ABS910_043	Not in use	0.0014	Not in use	0.0047	0.0202	Not in use

Table 4.2: Calculated a_t (m) for each transducer of A and B, from the tungsten carbide ball laboratory experiments.

Calculated a_t (m)						
Transducers	1 MHz	2 MHz	2.5 MHz	3 MHz	4 MHz	5 MHz
ABS910_170	0.01344	0.00672	0.00595	Not in use	0.00646	0.0062
ABS910_043	Not in use	0.00637	Not in use	0.00668	0.00615	Not in use

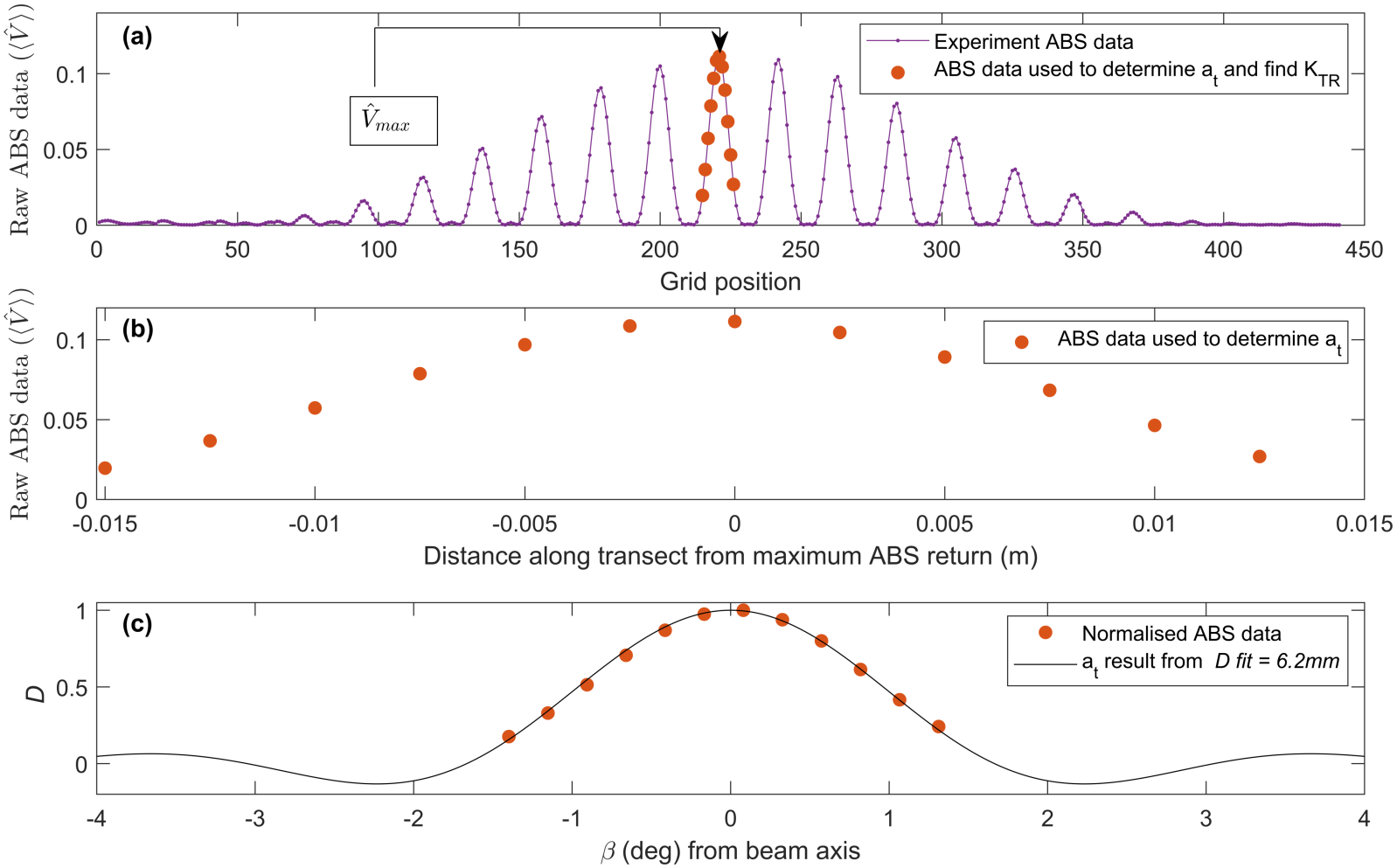

Figure 4.4: ABS data from bin 236, of the 5 MHz transducer (instrument A) from the tungsten ball laboratory experiment: (a) Transect of measured, raw ABS signal (purple dots) collected at each grid position (2.5 mm) over the total experimental grid length (50 mm), with the maximum ABS peak delineated (orange dots) (b) Location averaged ABS values (orange dots) over the measurement transect (m) from the central grid peak highlighted in (a) (c) normalised, ABS data vs theoretical model D fit (black line) at differing angles from the transducer beam axis, resulting in an estimated at of 6.6763 mm.

The maximum measured backscatter ($\hat{V}_{max}$), and other known parameters (D, f_∞, r, a, and α) were substituted into Equation (2.15) to give values for K_{TR} per transducer. The K_{TR} results calculated from the tungsten carbide ball target experiments for each transducer of instrument A and B are collated in (4.3).

Table 4.3: Calibration K_{TR} for each transducer of A and B, from the tungsten carbide ball ball laboratory experiments.

K_{TR} value						
Transducers	1 MHz	2 MHz	2.5 MHz	3 MHz	4 MHz	5 MHz
ABS910_170	19.141	6.036	11.998	Not in use	10.777	20.545
ABS910_043	Not in use	4.498	Not in use	11.968	7.655	Not in use

4.3 Particle suspension experiment

The recorded, raw backscatter signal illustrated in Figures (4.5) and (4.6) (respectively for instrument A and B) for the glass ballotini bead suspension experiments highlighted the attenuation of the ABS signature with time, over the tank water column. The signal decline was a trend observed for all transducers. A resemblance between Figures (4.5), (4.6) and (2.2) (Section 2.1) exists, as the water attenuation and at this stage, scattering attenuation due to sediment in the water, are to be factored into the depletion of the ABS response.

4.3.1 Laboratory gravimetric analysis results

Filtering of the water samples from the experiment with a suspension of glass beads provided concentrations of 188 mg/L, 199 mg/L and 188 mg/L for water samples 1, 2 and 3 respectively. The similarity between samples indicated the suspension remained well-mixed throughout the duration of the experiment,

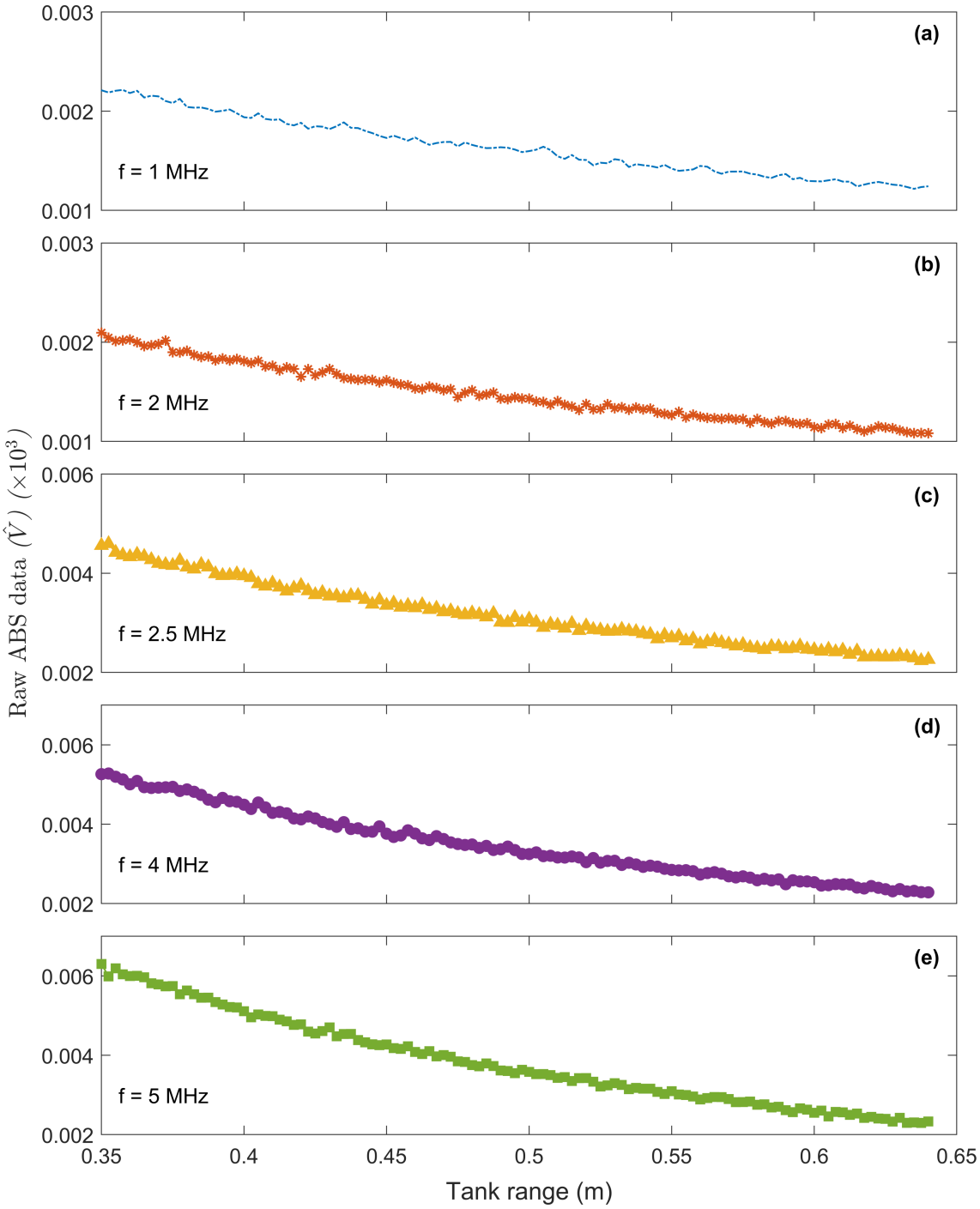

Figure 4.5: The raw ABS signal ($\hat{V}$) captured over the tank range (m) from 0.35 m to 0.64 m or across bins 162 to 256, for each transducer (1, 2, 2.5, 4, and 5 MHz) of A (coloured symbols).

and a nominal total average concentration of 195 mg/L of glass beads in solution was assumed across all experiments. Figure (4.7) mapped how the volume density (%) changed over time as a function of particle size (μm) for the glass ballotini beads in suspension. The mean d50 of the particle size, indicated as

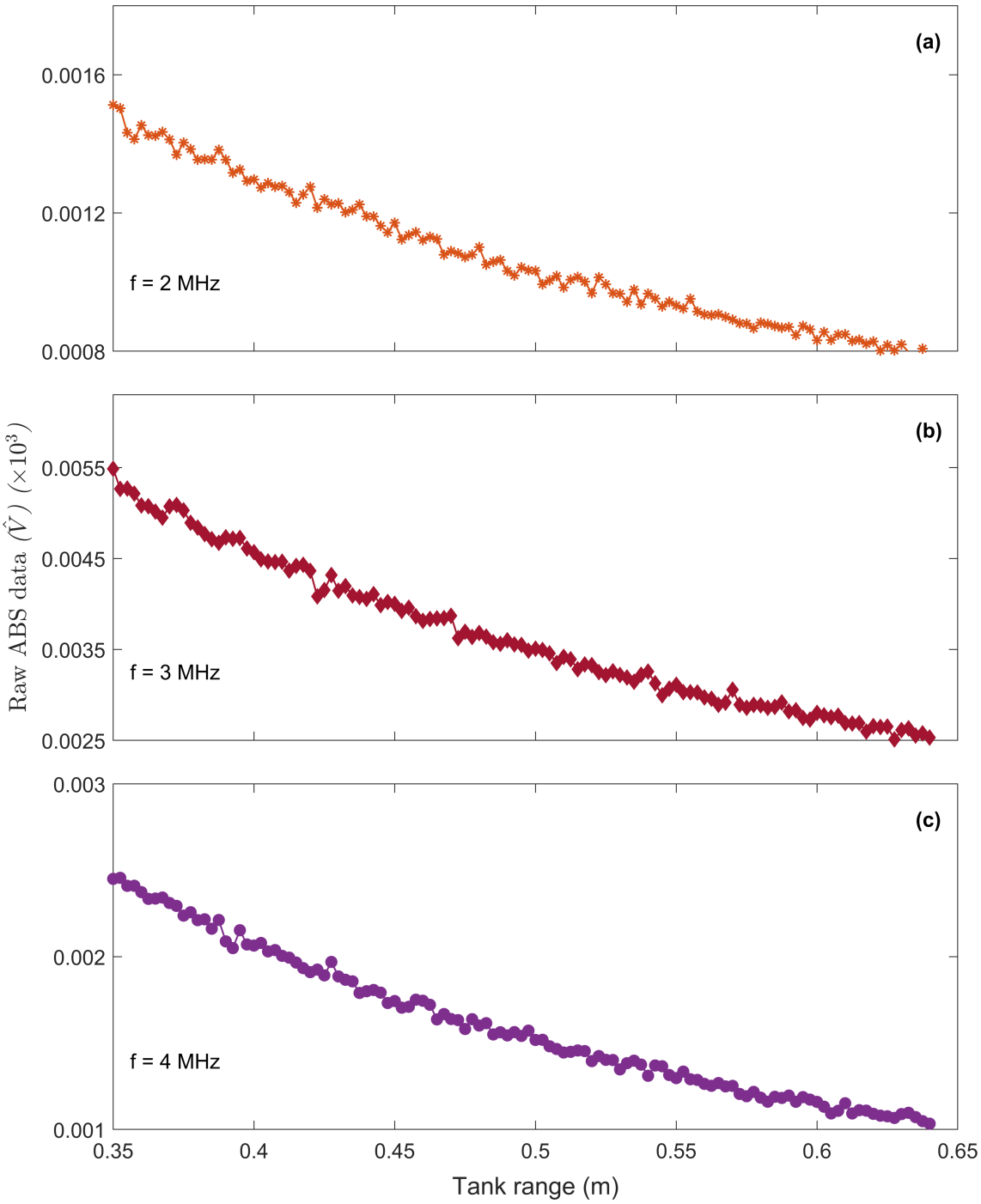

Figure 4.6: The raw ABS signal ($\hat{V}$) captured over the tank range (m) from 0.35 m to 0.64 m or across bins 162 to 256, for each transducer (2, 3, and 4 MHz) of B (coloured symbols).

the peak in Figure (4.7) based on volume density was observed at 91.4 μm, therefore the midpoint of the size aperture range of 45.7 μm was used as the estimated particle radius a.

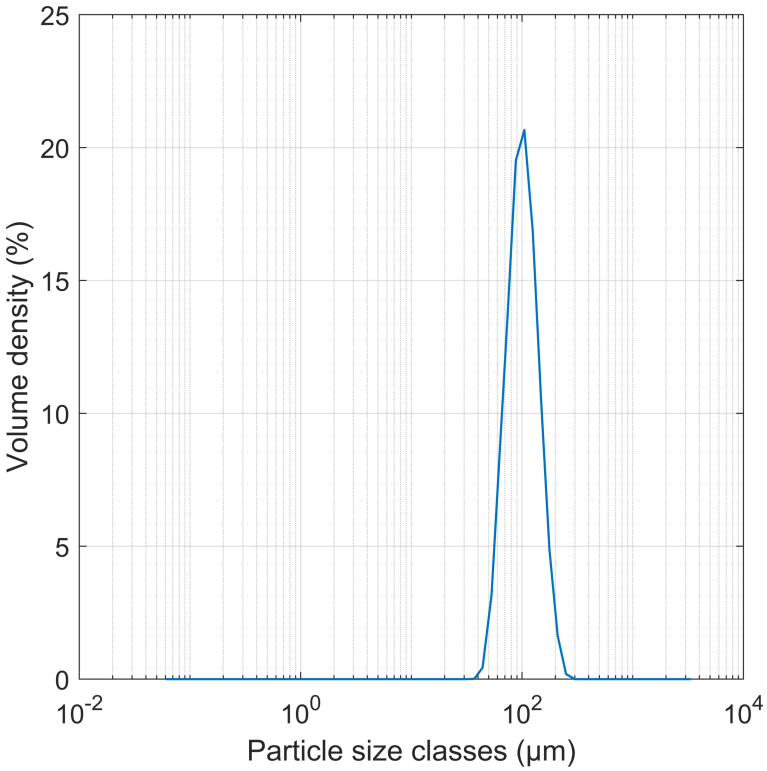

Figure 4.7: Malvern particle size analyser results (μm) on a log10 scale according to volume density (%) of the glass ballotinni bead suspension (classed as silica)

4.3.2 K_{TR} results

Figures (4.8) and (4.9) illustrated the estimates of K_{TR} as a function of range (m) for each transducer of instruments A and B. Assuming a homogenous suspension, a mean value was taken to provide a single estimate of K_{TR} for each transducer (shown by the black horizontal lines in Figures 4.8 and 4.9). For all transducers, the relative standard deviation (SD) across K_{TR} estimates along the profile length (0.4 to 0.64 m) was no more than 1.7 % of the mean value. Average K_{TR} results are summarised in Table (4.4) (instrument A) and (4.5) (instrument B) below, aggregated with SD, relative SD (%) and the minimum and maximum K_{TR} values across the tank, for each frequency.

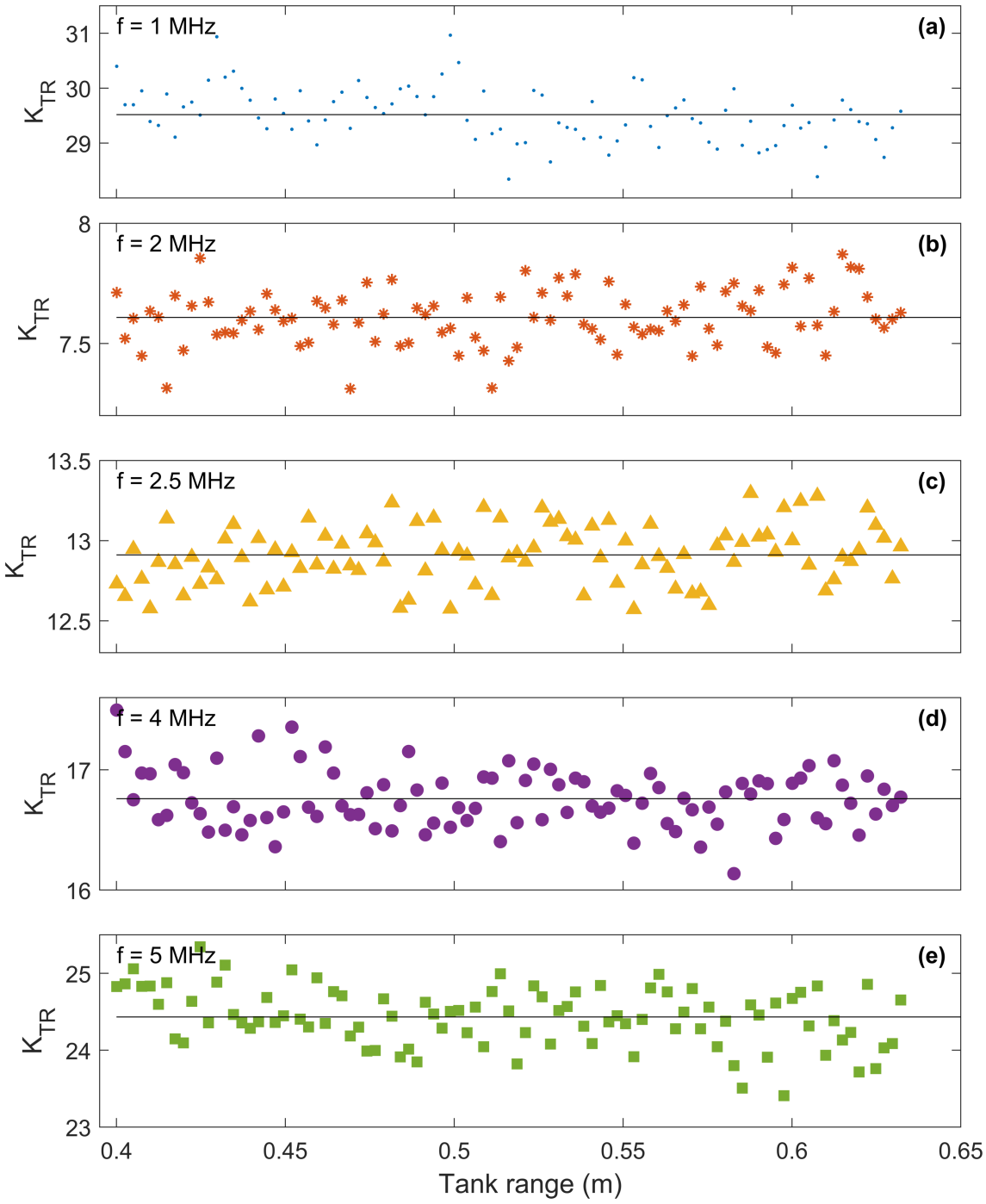

Figure 4.8: Calculated K_{TR} values for each transducer (1, 2, 2.5, 4, and 5 MHz) of A (coloured symbols) across bins 162 to 256, of the tank range (m) of 0.4 m to 0.64 m, against the average K_{TR} (black line) computed for the entire tank water column.

4.4 Comparision of K_{TR} values

The K_{TR} results for the tungsten carbide ball experiments as shown in Table (4.3), were compared to the K_{TR} values from the glass bead suspension

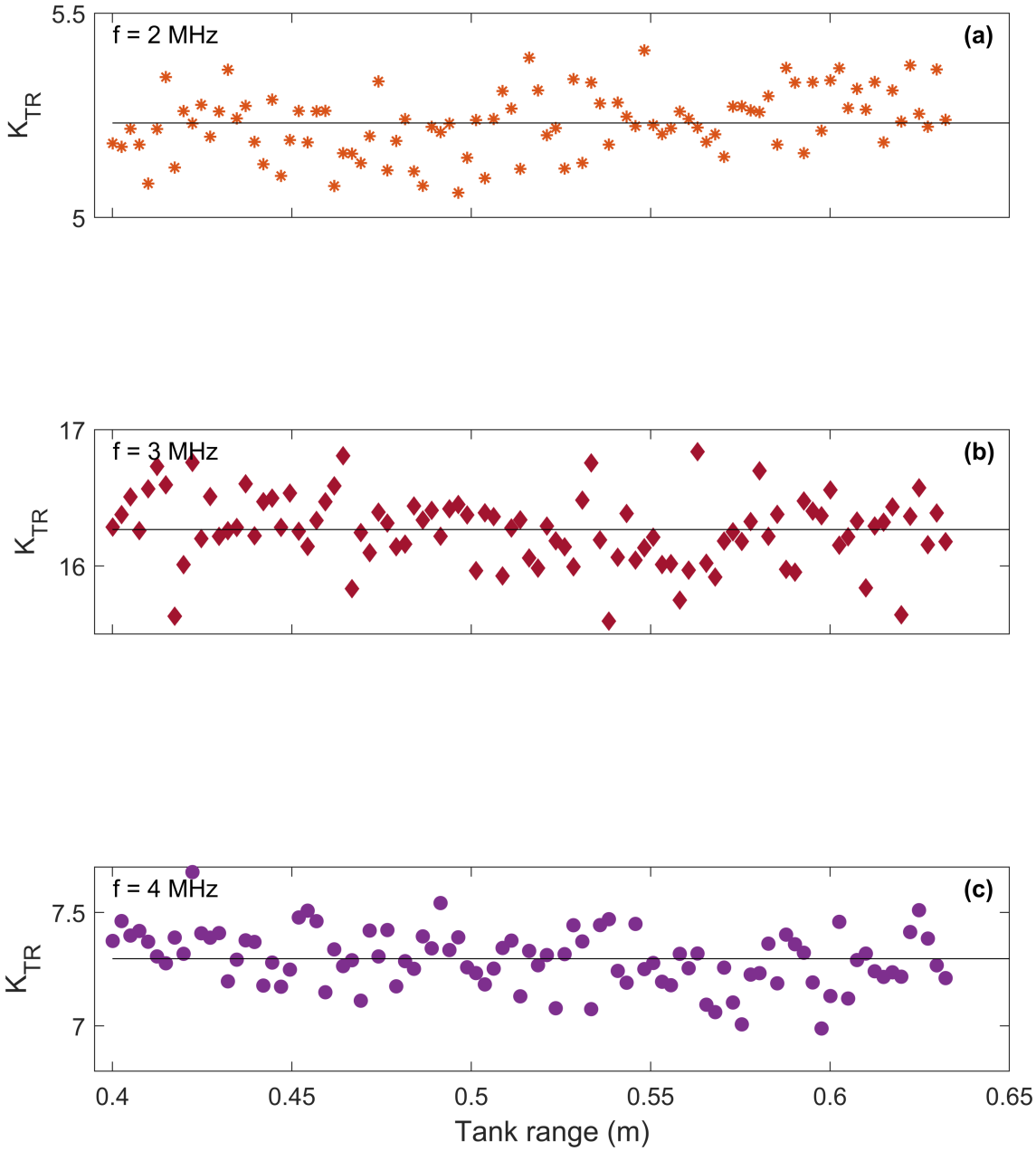

Figure 4.9: Calculated K_{TR} values for each transducer (2, 3, and 4 MHz) of B (coloured symbols) across bins 162 to 256, of the tank range of 0.4 m to 0.64 m, against the average K_{TR} (black line) computed for the entire tank water column.

experiments (Table 4.4 and 4.5). Table (4.6) and (4.7) summarise the results from instrument A and B, respectively, and percentage difference. In all but one case (4 MHz transducer, instrument B, Table 4.7), the estimates from the glass bead suspension experiments were larger, with differences ranging from 4.80 % up to 43.45 %. In terms of calculating Equation (2.8) for the particle suspension formulae, at worst the K_{TR} value of the tungsten carbide ball cal-

Table 4.4: Calculated calibration K_{TR}, standard Deviation (SD) (±), relative SD (%)) and minimum and maximum K_{TR} values for each transducer of instrument A, from the glass bead suspension experiments. Values shown are the mean value along the range ± one standard deviation.

(A)ABS910_170						
Transducers	1 MHz	2 MHz	2.5 MHz	3 MHz	4 MHz	5 MHz
Average K_{TR} value	29.5177	7.6083	12.9108	Not in use	16.7596	24.4324
(SD)	0.4899	0.1169	0.1823	Not in use	0.2391	0.3747
(Relative SD)	1.66	1.54	1.41	Not in use	1.43	1.53
[Min, max)]	[28.3431, 30.9640]	[7.3120, 7.8707]	[12.5715, 13.2960]	Not in use	[16.1361, 17.4967]	[23.4086, 25.3451]

Table 4.5: Calculated calibration K_{TR}, standard Deviation (SD) (±), relative SD (%)) and minimum and maximum K_{TR} values for each transducer of instrument B, from the glass bead suspension experiments. Values shown are the mean value along the range ± one standard deviation.

(A)ABS910_043						
Transducers	1 MHz	2 MHz	2.5 MHz	3 MHz	4 MHz	5 MHz
Average K_{TR} value	Not in use	5.2312	Not in use	16.2667	7.296	Not in use
(SD)	Not in use	0.0786	Not in use	0.2533	0.1242	Not in use
(Relative SD)	Not in use	1.50	Not in use	1.56	1.70	Not in use
[Min, max)]	Not in use	[5.0606, 5.4089]	Not in use	[15.5943, 16.8378]	[6.9885, 7.6775]	Not in use

ibration experiments would translate to an SSC value with a 43.45 % margin of error, in the case of the 4 MHz transducer (instrument A) (Table 4.6).

The single sphere calibration experiment K_{TR} terms, are to be implemented moving forward, with the reasons for the differences between the two experimental K_{TR} values discussed in detail in Section 5 (Discussion). We chose to select the K_{TR} values derived from the single sphere calibration method as it not only provides an estimate of K_{TR} but also allows for a direct estimate of a_t. Determining a_t from a suspension of particles is not possible.

Table 4.6: Laboratory calculated, K_{TR} values from the tungsten carbide ball, single sphere experiments and glass bead particle suspension experiments for instrument A, with (% difference.)

K_{TR} values						
Transducers	1 MHz	2 MHz	2.5 MHz	3 MHz	4 MHz	5 MHz
Tungsten carbide ball	19.141	6.036	11.998	Not in use	10.777	20.545
Glass ballotinni beads	29.5177	7.6083	12.9108	Not in use	16.7596	24.4324
Difference (%)	42.65	23.05	7.33	Not in use	43.45	17.29

Table 4.7: Laboratory calculated, K_{TR} values from the tungsten carbide ball, single sphere experiments and glass bead particle suspension experiments for instrument B, with (% difference).

K_{TR} values						
Transducers	1 MHz	2 MHz	2.5 MHz	3 MHz	4 MHz	5 MHz
Tungsten carbide ball	Not in use	4.498	Not in use	11.968	7.655	Not in use
Glass ballotinni beads	Not in use	5.2312	Not in use	16.2667	7.296	Not in use
Difference (%)	Not in use	15.07	Not in use	30.45	4.80	Not in use

4.5 Acoustic backscatter from the field

Time series of the burst-averaged ABS field data $\langle V^2 \rangle$ from the field experiments are shown in Figures (4.10) and (4.11), corresponding to instruments A and B, which were deployed upward and downwards-looking, respectively. For both instruments with different orientations, for most tides acoustic backscatter return was similar and largest closest to the bed, indicating the gradient in return was predominantly owing to the resuspension of bed material. The very large backscatter reading at 0 m (range) for each burst averaged backscatter profile of Figures (4.10) and (4.11) was due to the initial "ringing" of the ejected backscatter pulse off the transducer face and should be neglected.

In general, values were largest for the first tide, during which surface waves were largest (Figure 4.12b, significant wave height, $H_S \approx 0.25\,\mathrm{m}$). Moderate resuspension was also observed for tides 3 and 5 owing to the combination of surface waves ($H_S \approx 0.12\,\mathrm{m}$) and shallower water depths (Figure 4.12a). Given the similarity in backscatter pattern from A and B (Figures 4.10 and 4.11), and noting one transducer (1 MHz, channel 1) failed for the downward-looking instrument, for clarity, henceforth the data analysis will focus on the ensemble scattering characteristics and ABS inversion for the upward-facing instrument, A.

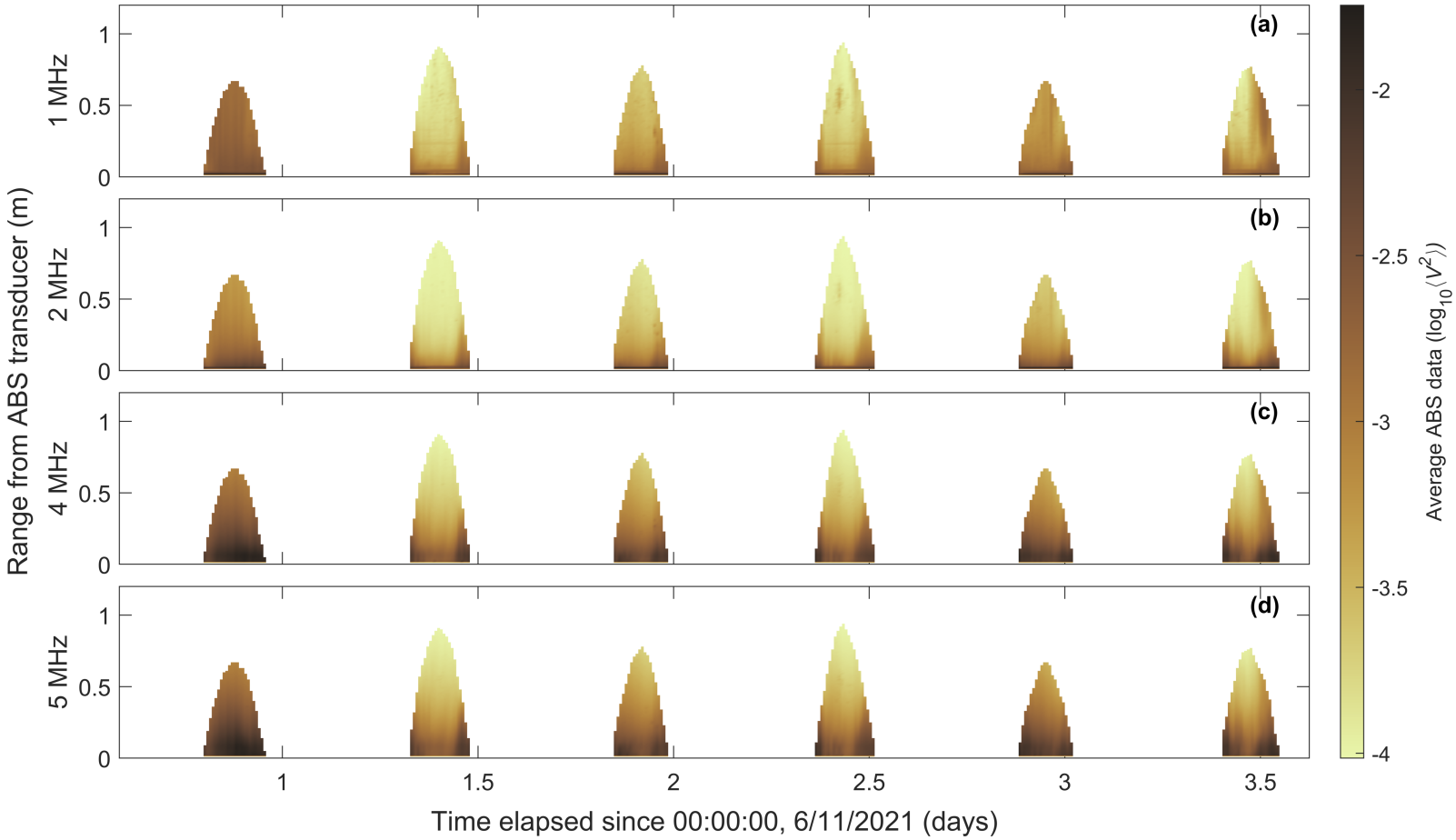

Figure 4.10: Time series of burst averaged field ABS ($\log_{10}\langle V^2\rangle$) profiles over six tidal cycles for instrument A positioned at the seabed, looking upwards (a) 1 MHz, channel 1 (b) 2 MHz, channel 2 (c) 4 MHz, channel 3 and (d) 5 MHz, channel 4.

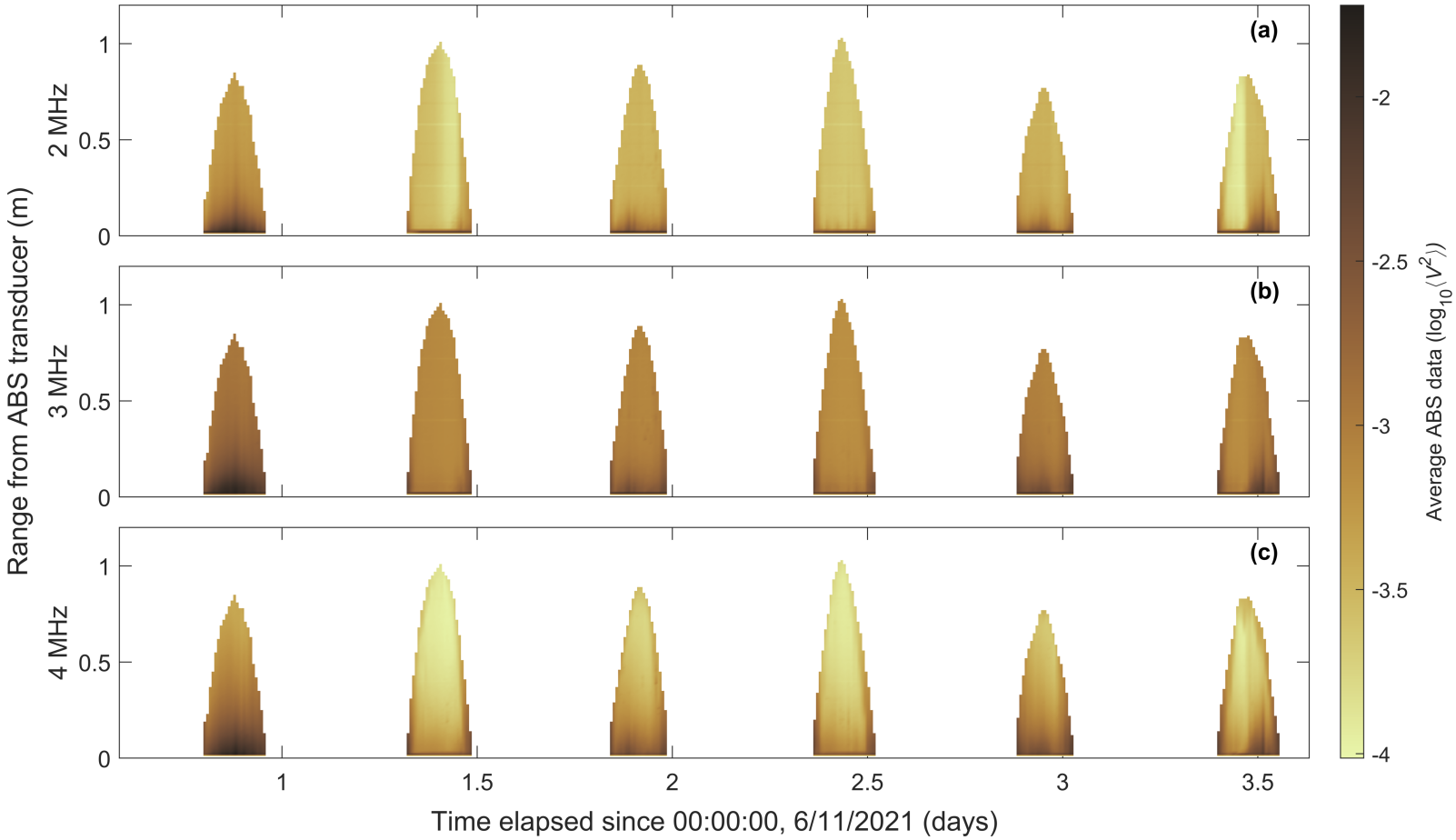

Figure 4.11: Time series of burst averaged ABS ($\log_{10}\langle V^2 \rangle$) profiles over six tidal cycles for instrument B positioned at the water's surface, looking downwards (a) 2 MHz, channel 2 (b) 3 MHz, channel 3 and (c) 4 MHz, channel 4.

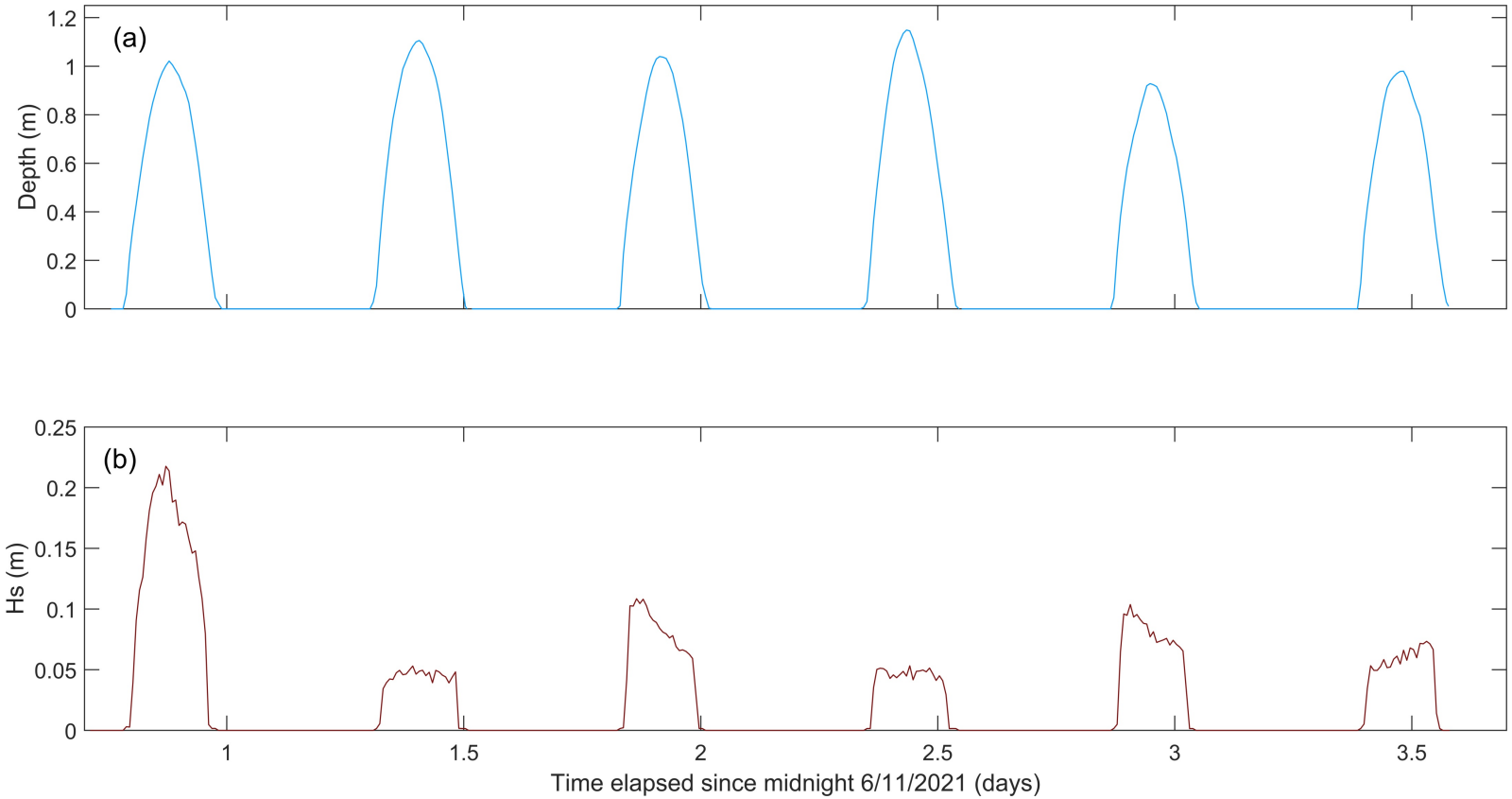

Figure 4.12: (a) significant wave height (H_s) (m) and (b) water depth (m), from the field deployment period. Data provided by T. Biesly.

4.5.1 Scattering characteristics obtained from field data

To obtain f_∞ and Σ_s from the field data, the acoustic backscatter was plotted in the form shown in Equation (2.23) (Section 2.5). The slope (m) and intercept (c) gained from fitting the data when present in this form are then used, in collaboration with estimates of M (or conversely N) to estimate values for f_∞ (Equation 2.28) and Σ_s Equation (2.31) for the particles in suspension for each ABS burst. To solve equations Equation (2.28) and Equation (2.31) and obtain estimates of f_∞ and Σ_s, M and N are required. In this study the suspended sediment concentration (M) comes from the SSC estimates derived from the optical backscatter sensors (M_{OBS}). To convert between M to N, Equation (2.7) must be used and to do that the particle size (a) and particle density (ρ_s) are required. For this study, obtaining the in-situ particle size spectra and particle density distribution was not possible as these are extremely difficult to measure, particularly at the SSC typically found at the study. Given this we took the pragmatic approach and assumed that the mean bed-sediment particle (size) was representative of the suspended particle size. Furthermore, a nominal density of 2600 kg/m^3 was assumed. From previous work at the field site the mean bed diameter $d50$ was measured to be 8 μm, therefore a of 4μm was used (Lovett, 2017).

As mentioned in Section (2.5), a potential limitation in deriving estimates of f_∞ and Σ_s, is that M must be known and be approximately constant over the range of r values used in the fit. This limitation is explored in Figure (4.13), which shows the time-series of M_{OBS} measured at four locations during the field experiment. The figure shows that SSC in the near-bed region were typically greater than those observed higher in the water column. The results all also indicate that above 0.4 m the SSC found in the water column are roughly constant, with only minor differences in SSC measured at 0.4 and 0.76 m above the bed. Consequently, the average SSC value from these two

heights were used to calculate M and subsequently used in the derivation of f_∞ and Σ_s. As we shall see later, the ABS data used in the derivation of f_∞ and Σ_s also comes from a similar location in the water column.

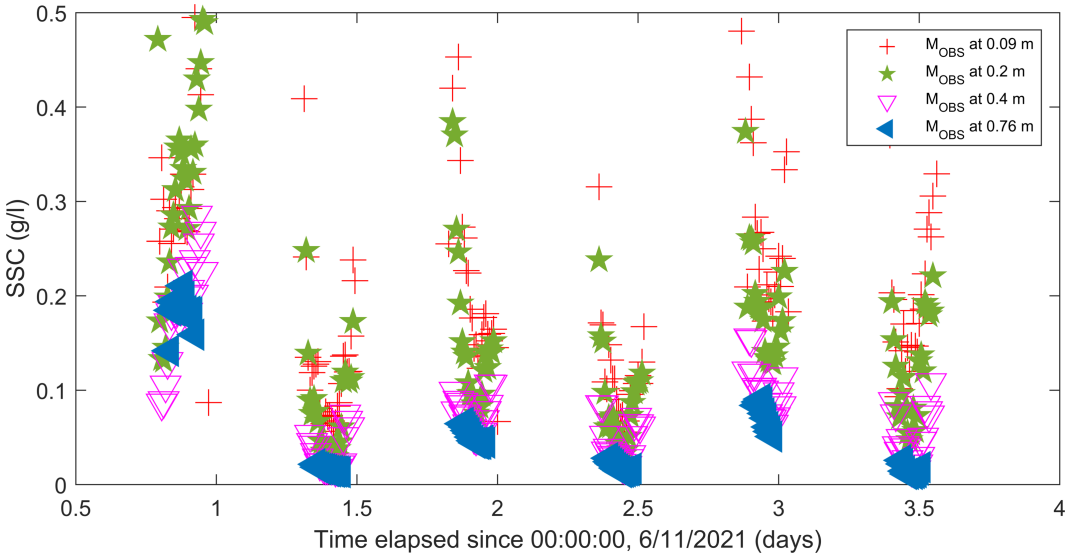

Figure 4.13: Time series of SSC over the field measurement time, captured by four OBS instruments distinguished by colour (red, green, pink and blue) and corresponding to heights (0.09, 0.2, 0.4 and 0.76 m) where each were stationed in the water column.

Table 4.8: R^2 margin of error for each of the four OBS instruments used in the field sampling, calibrated against bed sediment samples collected from the field. HAB = Height above bed.

OBS instrument (HAB (m))	Laboratory R^2 (Gain setting 1) (Gain setting 2)
0.76	0.99 , 0.97
0.4	1.00, 0.98
0.2	0.98, 0.98
0.09	0.99, 0.99

The error derived from the laboratory calibration of the OBS instruments from each height, derived from bed sediment samples collected in the field are summarised in Table (4.8). The OBS sensor calibrations were of a high quality

with $R^2 > 0.97$.

Examples of the linear fit to Equation (2.23) for six bursts are shown in Figures (4.14) to (4.19) for a range of fit qualities, as assessed by an R^2 value. Noting the standard linear fit technique (Thorne and Buckingham, 2004) was only applied to ranges $r > 0.3\,\mathrm{m}$ to ensure the backscatter analysed was in the far-field zone. For instrument A, the average $\langle V^2 \rangle^{1/2}$ was predicted to decrease with increasing range from the transducer. In general, for all figures shown the fits were of a better quality for the higher frequency transducers – which show negative slopes m, as expected. Conversely, fits for the lower frequency transducers (1 and 2 MHz) were more variable and sometimes positive slopes were noted as observed for both transducers in Figures (4.16) and (4.17). This result was most obvious in Figures (4.16) for the 1 MHz fit line (blue).

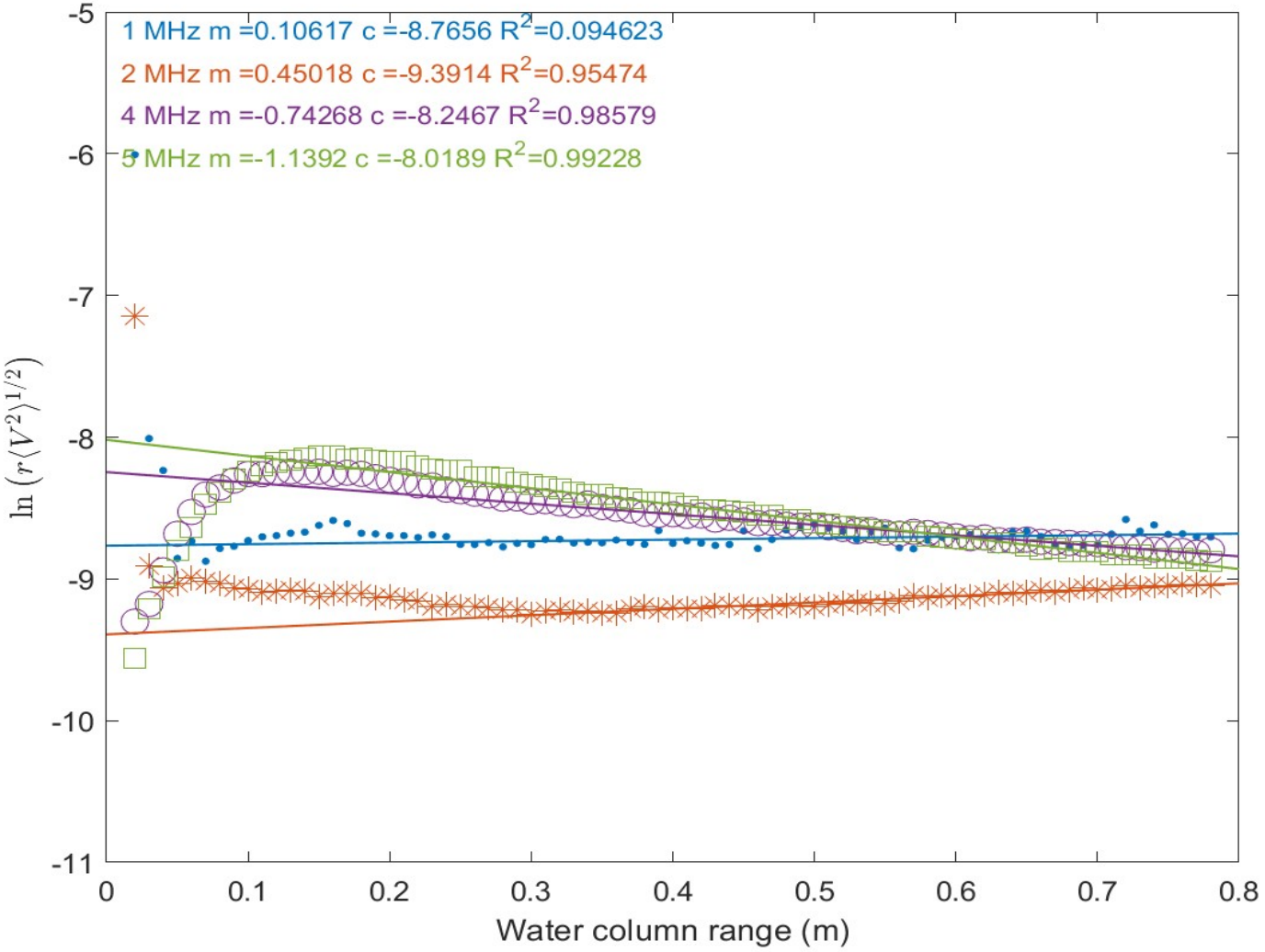

Figure 4.14: Linear fit of $\ln\left(r\langle V^2\rangle^{1/2}\right)$ vs r (m) for burst 194 (07/11/21, 22:10:00) of instrument A, with m, c and R^2 values. $\ln\left(r\langle V^2\rangle^{1/2}\right)$ observations are represented by the symbols corresponding to frequency (1 MHz, dots, 2 MHz, stars, 4 MHz, circles, and 5 MHz, squares) by colour.

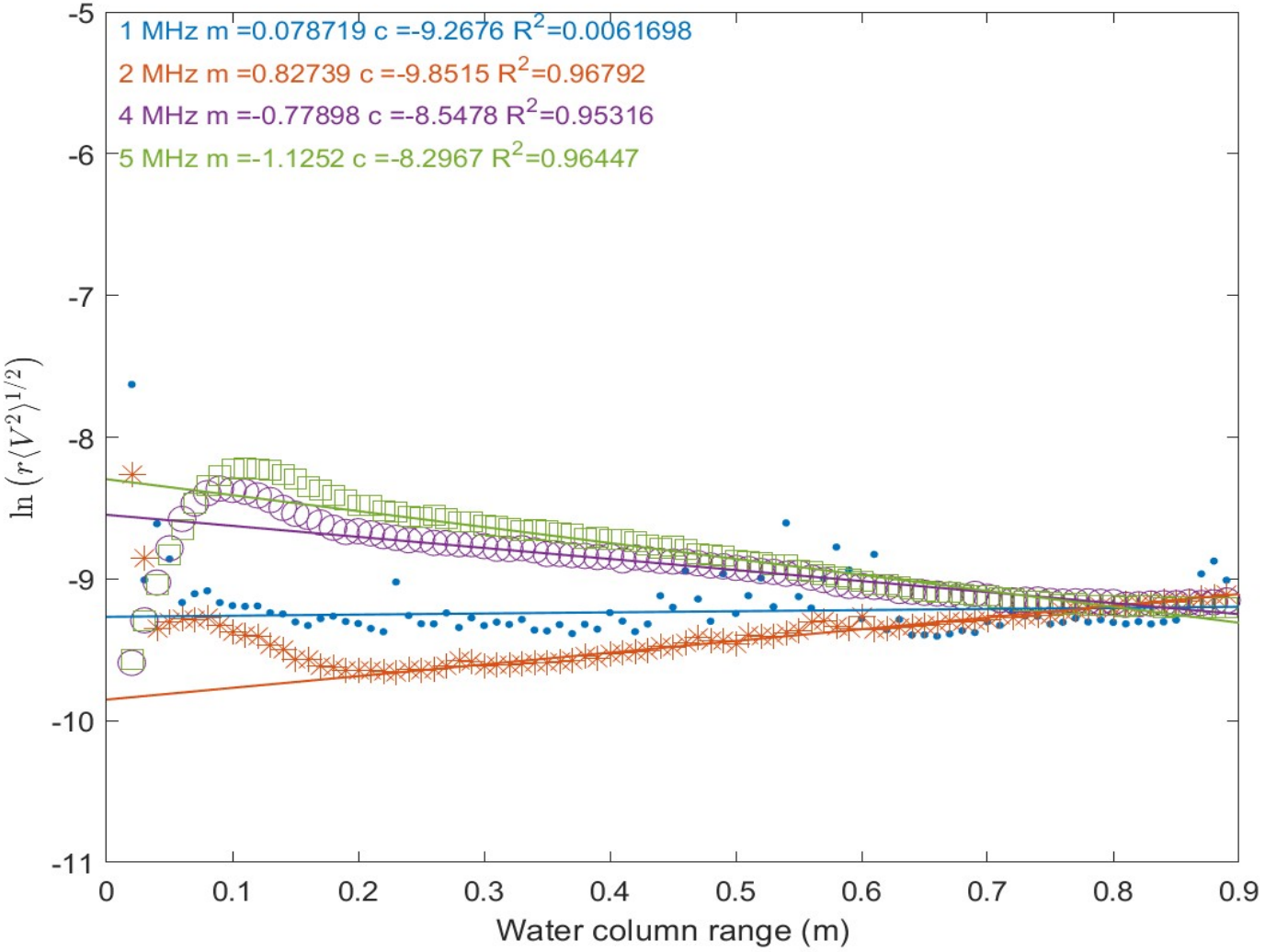

Figure 4.15: Linear fit of $\ln\left(r\langle V^2\rangle^{1/2}\right)$ vs r (m) for Burst 265 (08/11/21, 10:00:00) of instrument A, with m, c and R^2 value. $\ln\left(r\langle V^2\rangle^{1/2}\right)$ observations are represented by the symbols corresponding to frequency (1 MHz, dots, 2 MHz, stars, 4 MHz, circles, and 5 MHz, squares) by colour.

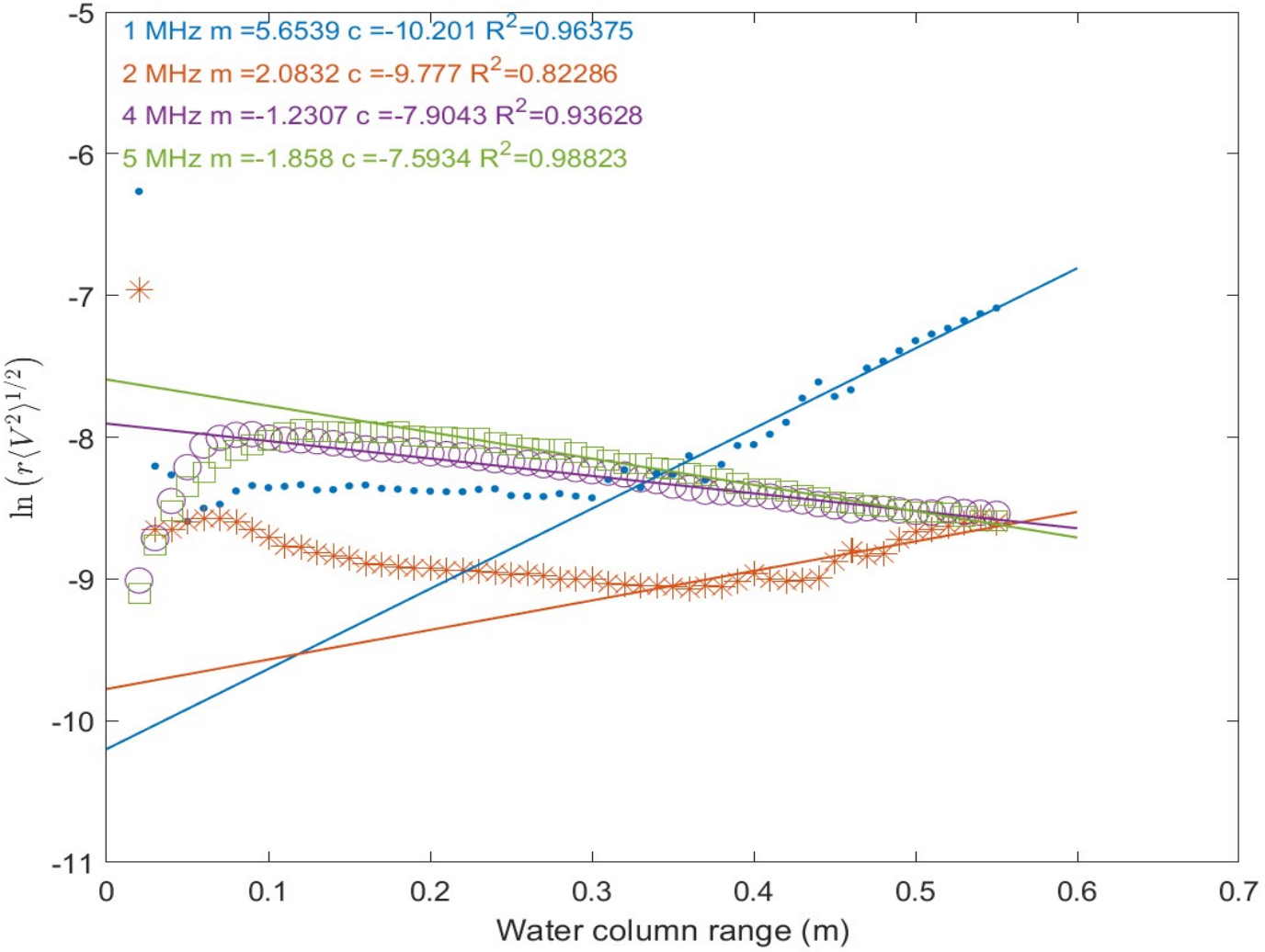

Figure 4.16: Linear fit of $\ln\left(r\langle V^2\rangle^{1/2}\right)$ vs r (m) for Burst 346 (08/11/21, 23:30:00) of instrument A, with m, c and R^2 value. $\ln\left(r\langle V^2\rangle^{1/2}\right)$ observations are represented by the symbols corresponding to frequency (1 MHz, dots, 2 MHz, stars, 4 MHz, circles, and 5 MHz, squares) by colour.

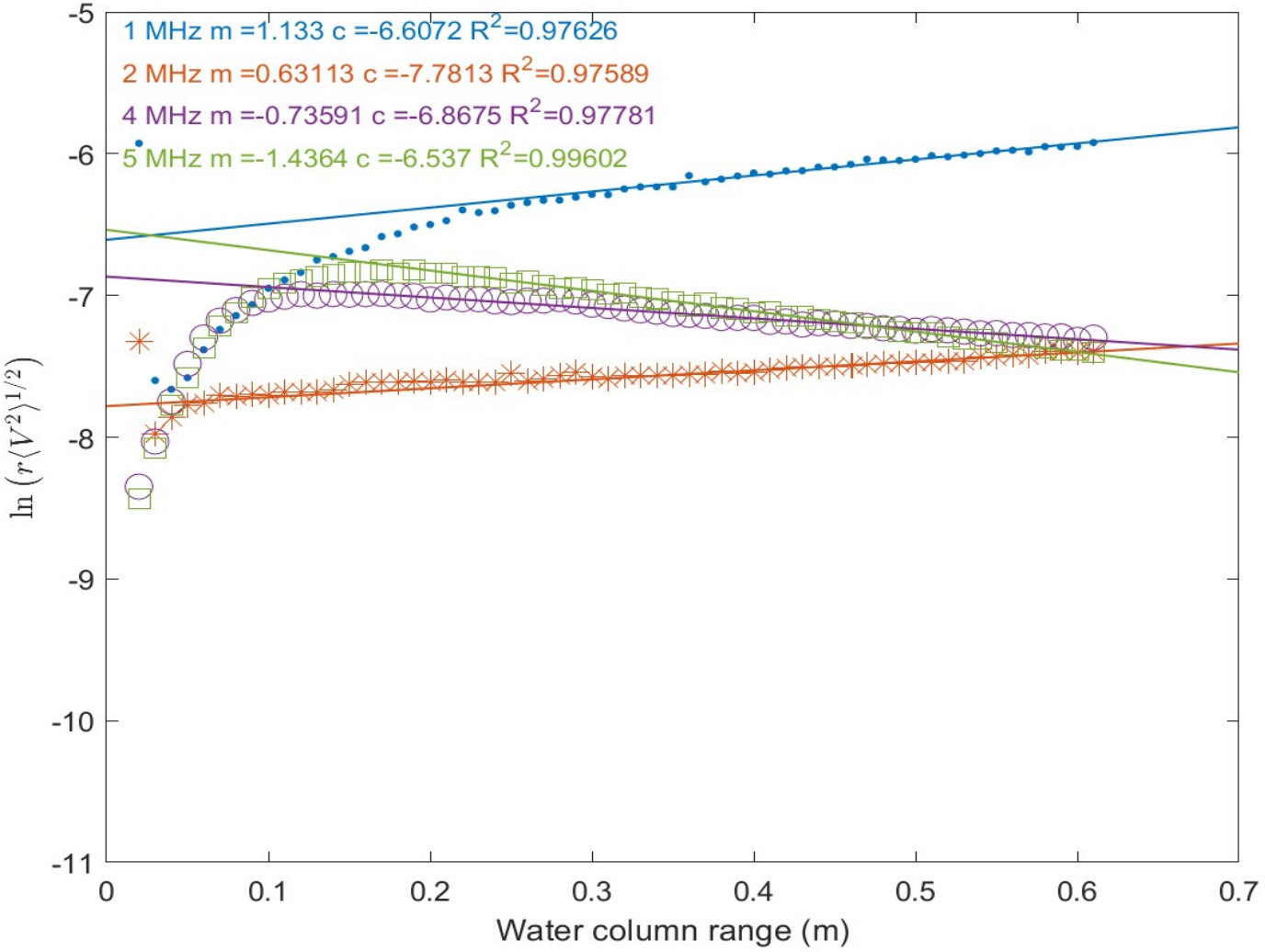

Figure 4.17: Linear fit of $\ln\left(r\langle V^2\rangle^{1/2}\right)$ vs r (m) for Burst 40 (06/11/21, 20:30:00) of instrument A, with m, c and R^2 value. $\ln\left(r\langle V^2\rangle^{1/2}\right)$ observations are represented by the symbols corresponding to frequency (1 MHz, dots, 2 MHz, stars, 4 MHz, circles, and 5 MHz, squares) by colour.

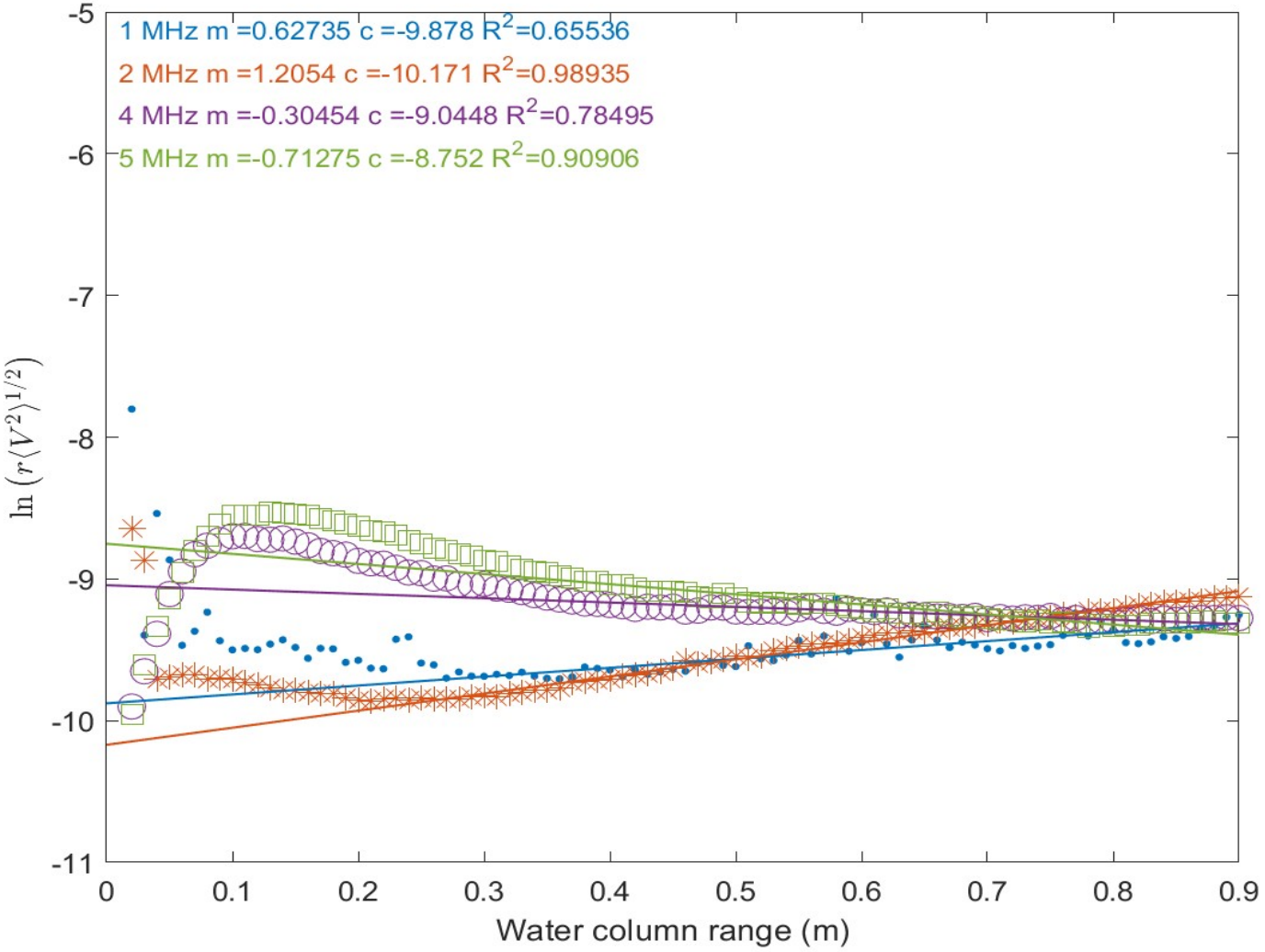

Figure 4.18: Linear fit of $\ln\left(r\langle V^2\rangle^{1/2}\right)$ vs r for Burst 120 (07/11/21, 09:50:00) of instrument A, with m, c and R^2 value. $\ln\left(r\langle V^2\rangle^{1/2}\right)$ observations are represented by the symbols corresponding to frequency (1 MHz, dots, 2 MHz, stars, 4 MHz, circles, and 5 MHz, squares) by colour.

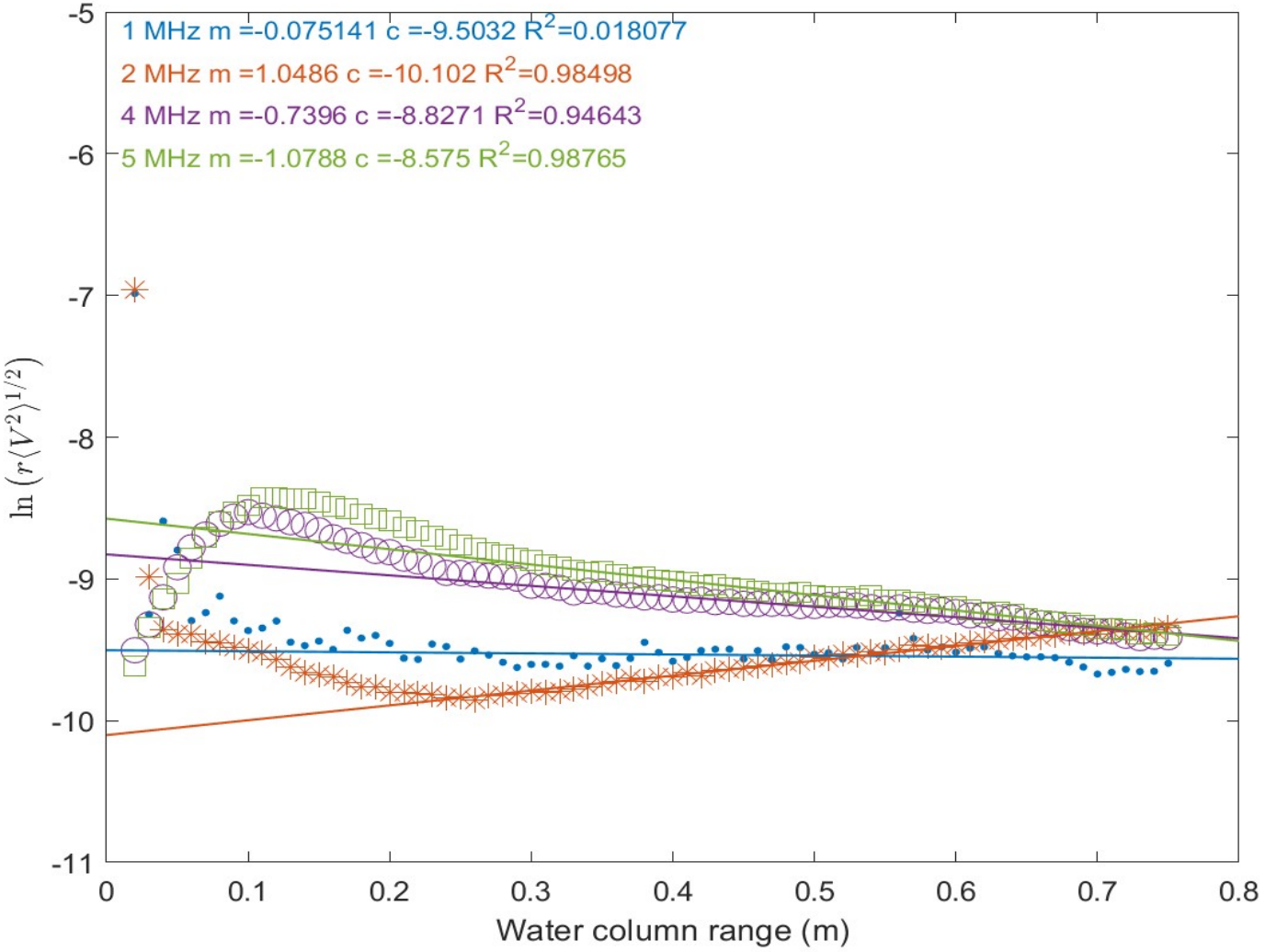

Figure 4.19: Linear fit of $\ln\left(r\langle V^2\rangle^{1/2}\right)$ vs r (m) for Burst 415 (09/11/21, 11:00:00) of instrument A, with m, c and R2 value. $\ln\left(r\langle V^2\rangle^{1/2}\right)$ observations are represented by the symbols corresponding to frequency (1 MHz, dots, 2 MHz, stars, 4 MHz, circles, and 5 MHz, squares) by colour.

The linear fit acquired c and m with fit quality attribute R^2, are summarised in Figure (4.20) along with the obtained scattering characteristic estimates, and complementary SSC estimates obtained from the OBSs. The u-shaped curve to the M_{OBS} over time suggested increasing SSC with water depth above the bed, aligned with the field ABS readings displayed in Figures (4.10) and (4.11). The overall shape was coordinated with tidal flow, where greater rates of sediment were suspended into the water column when the water depths were low, possibly indicating resuspension by waves (Figure 4.20). Aside from tide one, the measured SSC measured by the OBS over the experimental duration were generally low (less than 0.3 mg/L), verifiable by the ABS field data and wave conditions discussed above (Section 4.5).

In general, the c intercepts were aligned with the u-shaped trend in the tidal variation of SCC measured by the OBS, with 4 and 5 MHz obtaining higher magnitude c values. Whereas the slope m values were less in phase with the OBS SSC measurements and 4 and 5 MHz attained the most negative order gradients (Figure 4.20). The f_∞ estimations across the time series had a similar trend shape like the M_{OBS} values, but the Σ_s values showed no discernable pattern. The 4 and 5 MHz transducers appeared to produce greater f_∞ values and larger Σ_s values relative to the other transducers across the field measurements (Figure 4.20). For 1 and 2 MHz, f_∞ values were no greater than 0.02, whereas for 4 and 5 MHz, they tended to be greater than 0.02. In general, for tide 1 the f_∞ values for all transducers were larger than those calculated for the tides, specifically the range of f_∞ values for 4 and 5 MHz was between 0.03 to 0.05. The linear fits judging by the R^2 values were less well fitted under tides 2, 3, 4 and 6, particularly for 1 and 2 MHz (Figure 4.20). Overall, the Σ_s range of values for all transducers calculated across the measurement campaign were very small, around 1×10^{-11}.

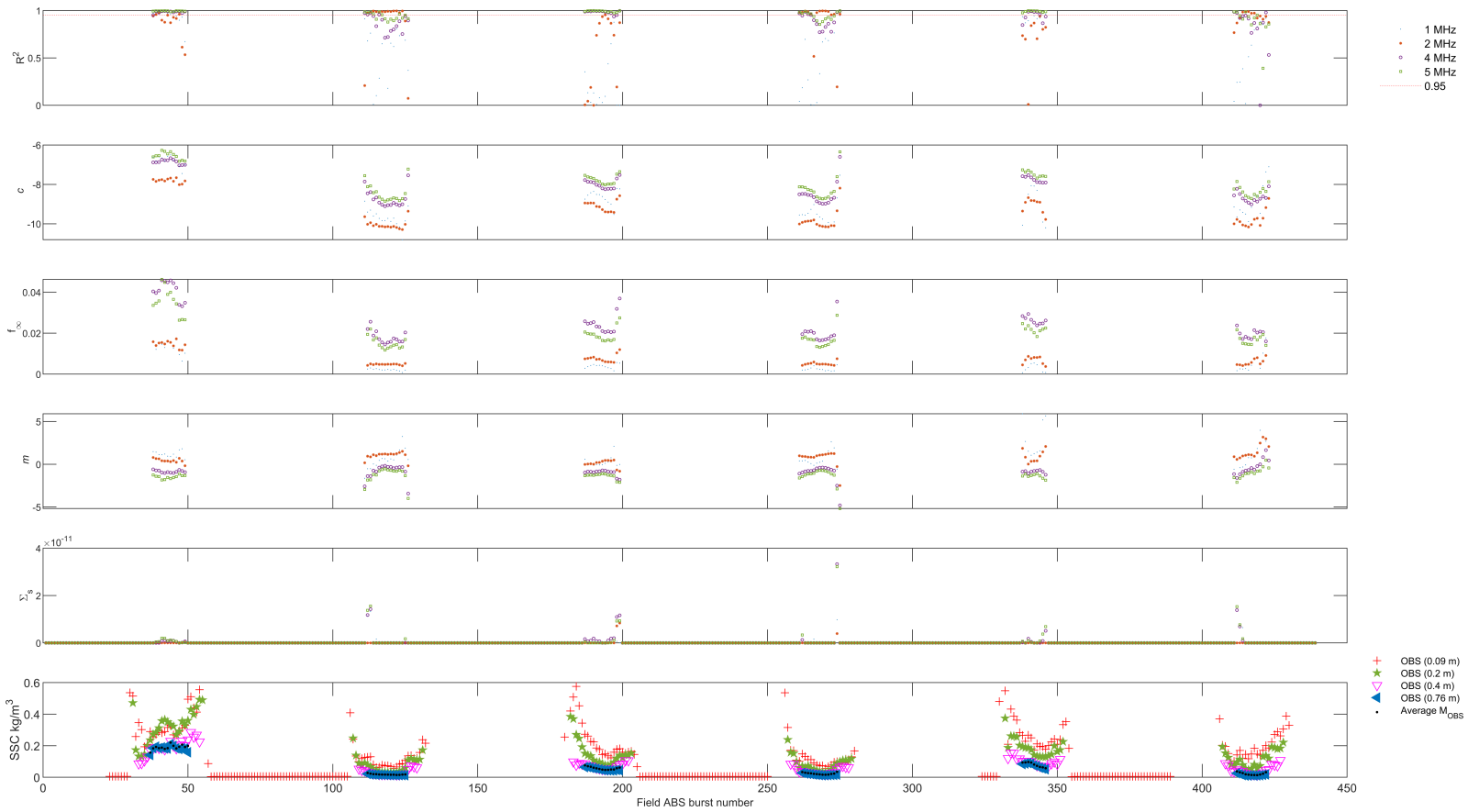

Figure 4.20: Time series of all field burst averaged data ($\langle V^2 \rangle^{1/2}$) derived parameters of slope m and intercept c values, and individual, time-varying f_∞ and Σ_s values from the four days of field measurements for each transducer (1, 2, 4 and 5 MHz) (colours) of A. Plus, the burst averaged M_{OBS} measurements collected from each OBS device stationed on the steel frame installed at the field site adjacent to the ABS instrumentation, and the averaged M_{OBS} concentrations from the top two M_{OBS} profiles (pink and blue OBS) used for calculation of f_∞ and Σ_s are plotted (black dots).

Following the linear fit analysis, Figure (4.21) below shows the burst which met a fit quality threshold of $R^2 > 0.95$ (Figure 4.21) and the matching m and c values. In total, across the processed bursts, the 1 MHz transducer obtained ten bursts satisfying $R^2 > 0.95$ and $r > 0.5$, the 2 MHz transducer had thirty-six, the 4 MHz transducer equaled forty-two and finally the 5 MHz transducer, fifty-three bursts. There is a greater proportion linear fits deemed acceptable for implementation in the following inversion analysis for the higher frequency transducers (4 MHz and 5 MHz). The tallied amount and burst numbers for each transducer of instrument A, supposing the threshold of $R^2 > 0.95$, are given in Table (B.1) (Appendix (B)). Clearly as is seen in Figure (4.21), the m and c results still largely maintain the overall data pattern correlated to the M_{OBS} tidal profiles (Figure 4.20) even after reducing the selection of ABS data for inversion analysis.

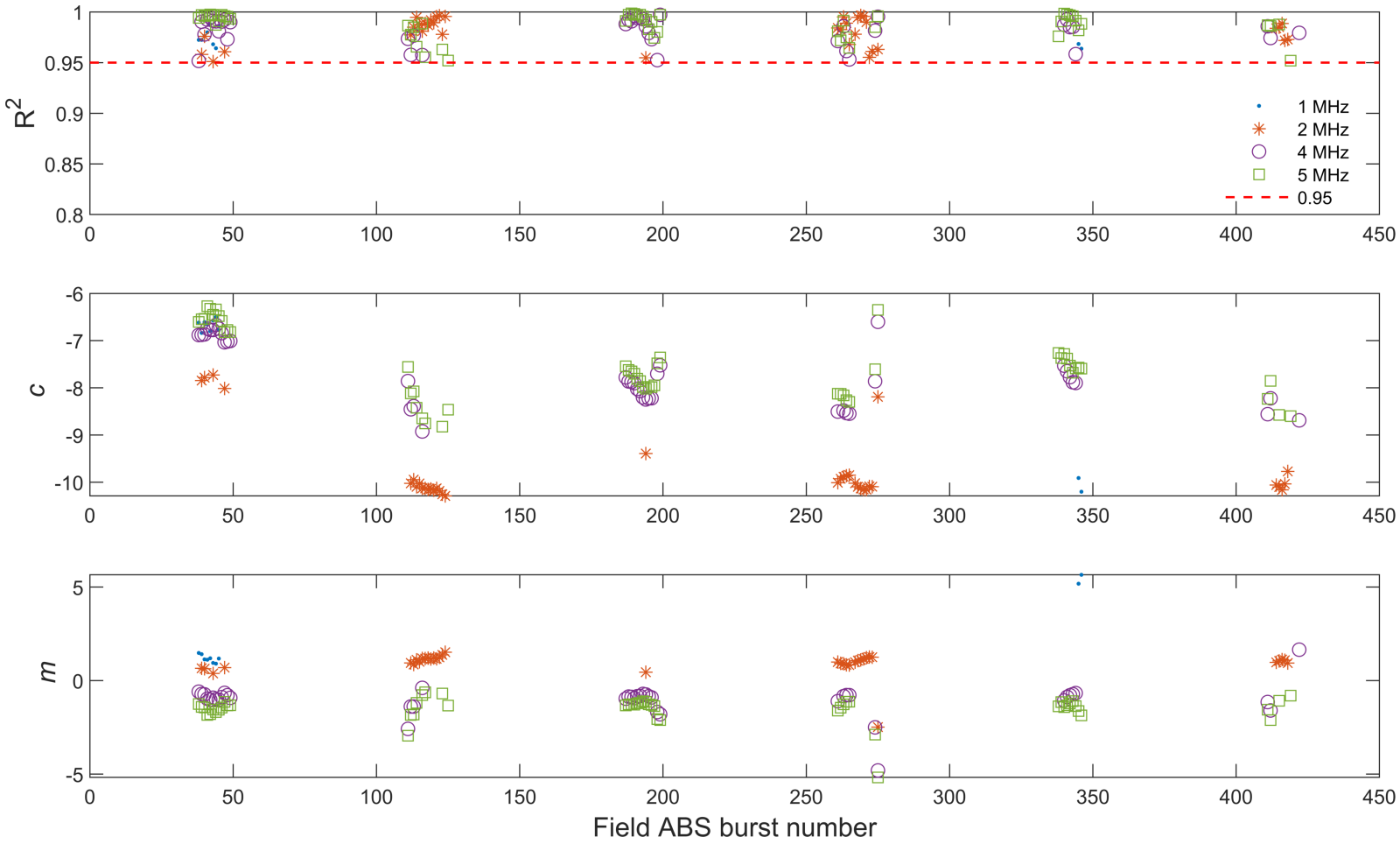

Figure 4.21: Field burst files with an $R^2 > 0.95$ and the relative, calculated c values and m values for transducers 1, 2, 4, and 5 MHz (colours) (A).

4.6 SSC inversion methods for field ABS data

4.6.1 Linear fit analysis of f_∞ and Σ_s

Once f_∞ and Σ_s were obtained for field bursts with $R^2 > 0.95$ and $r > 0.5$, the profiles of SSC (kg/m^3) in the water column were achieved by an inversion of the ensemble-averaged ABS data (method 1) per burst and for each transducer, as described in Section (2.3.1). Example inversion results are shown in Figures (4.22) to (4.27), for the same bursts corresponding to the linear fits shown in Figures (4.14) to (4.19).

As before, the results demonstrate a range of fit qualities. Considering the significant spiking in the raw ABS readings for the 2, 4 and 5 MHz transducers of Figures 4.22 and 4.23 for bursts 194 and 265, the despiking method (Section 3.5.2) worked well based on the ensemble average profiles of M_{ABS}. Figures (4.22) and (4.23) showed the estimates derived for the inversion of the ABS data M_{ABS}, compared very well with the M_{OBS} values. For both Figures (4.22) and (4.23), the 4 and 5 MHz transducers produced the most closely matched sequence of M_{ABS} SSC profiles for the field data proportional to the field M_{OBS}. Both Figure (4.22) and (4.23) indicated that the M_{OBS} observations from higher in the water column are closely matched by the inversion results M_{ABS} estimates.

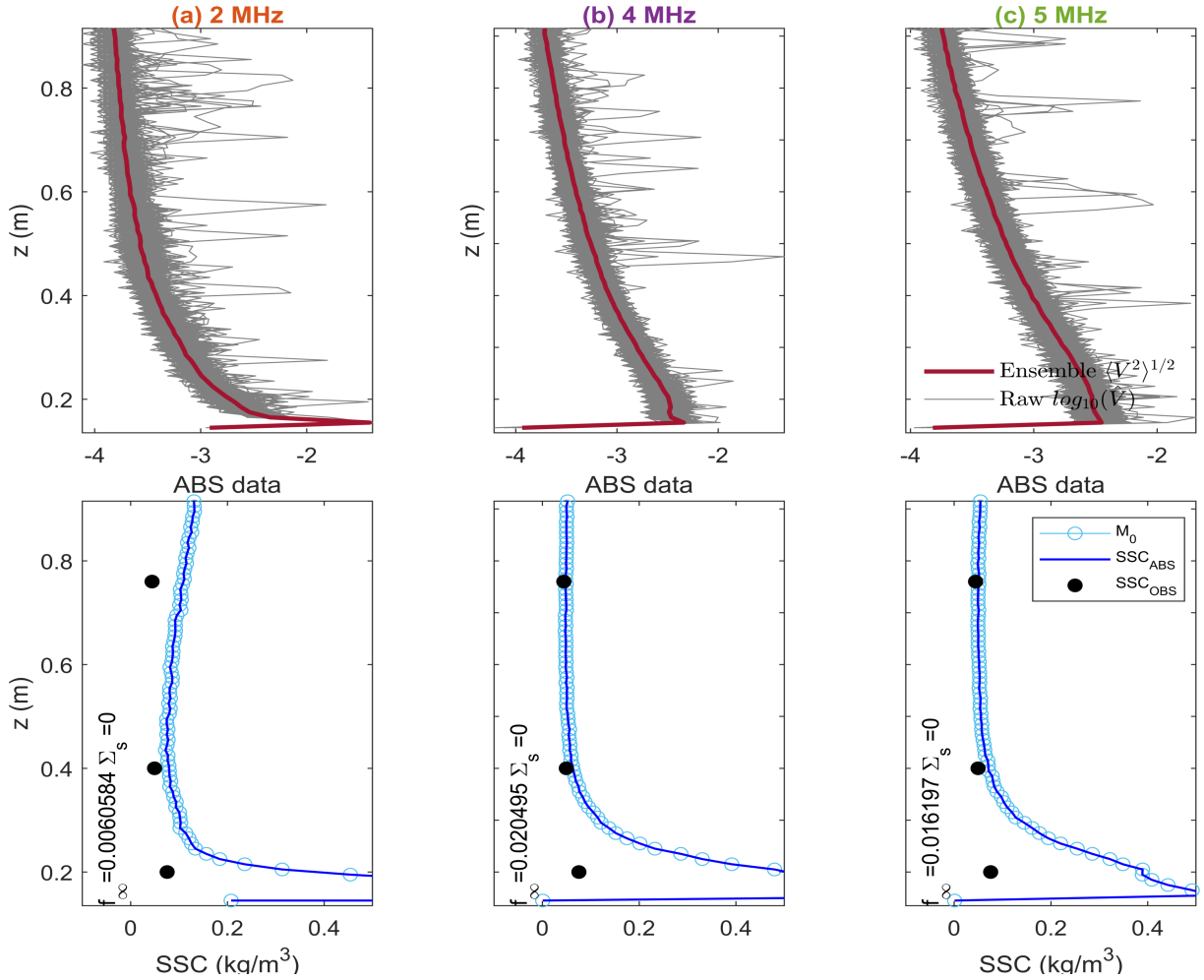

Figure 4.22: Vertical water column (z, (m)) starting at 0.135 m above the bed, where (A) was positioned showing the raw $log_{10}(\hat{V})$ (grey line) and ensemble averaged ($\langle V^2 \rangle^{1/2}$) ABS (brown line) for transducer frequencies (2, 4, and 5 MHz, A) (a – c). Profiles of M_0 (light blue 'o'), and M_{ABS} (dark blue '-') are derived from the ensemble averaged individual f_∞ and Σ_s for each transducer, for Burst 194. The M_{OBS} measurements (black 'o') are shown at the relevant heights in the water column, for Burst 194 (07/11/21, 22:10:00).

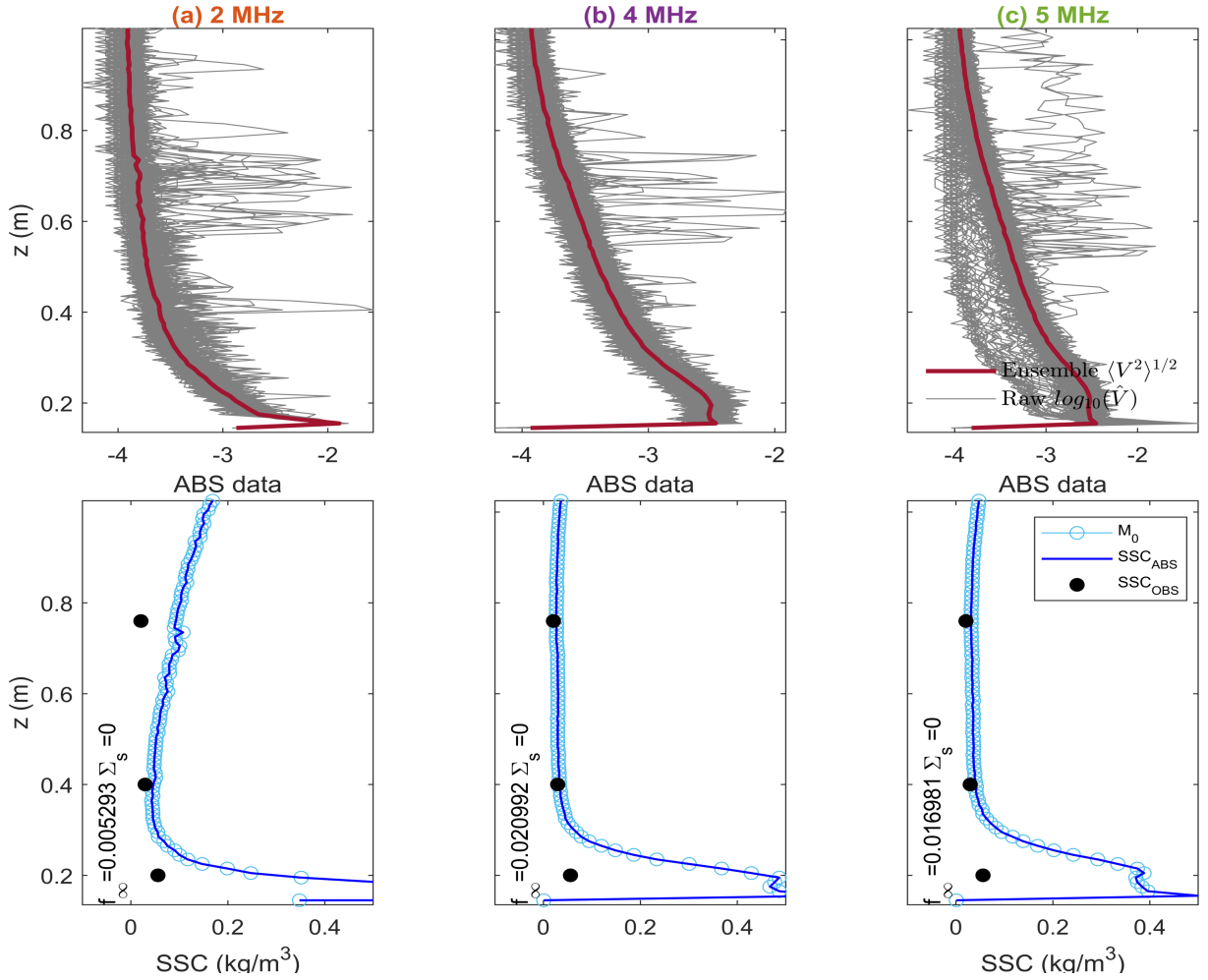

Figure 4.23: Vertical water column (z, (m)) starting at 0.135 m above the bed, where (A) was positioned showing the raw $log_{10}(\hat{V})$ (grey line) and ensemble averaged ($\langle V^2 \rangle^{1/2}$) ABS (brown line) for transducer frequencies (2, 4, and 5 MHz, A) (a – c). Profiles of M_0 (light blue 'o'), and M_{ABS} (dark blue '-') are derived from the ensemble averaged individual f_∞ and Σ_s for each transducer, for Burst 265. The M_{OBS} measurements (black 'o') are shown at the relevant heights in the water column, for Burst 265 (08/11/21, 10:00:00).

The results corresponding to bursts when the linear fits of specific transducers were poor (Figure 4.24 and 4.25, bursts 346 and 40) although satisfying $R^2 > 0.95$, do not appear to provide reliable inversion results. This conclusion is evident as the M_{ABS} estimates do not compare favourably with M_{OBS}. For Burst 346 (Figure 4.24), the 1 MHz transducer achieved an $R^2 = 0.96$ (Section 4.5.1) yet a positive slope from the linear fit procedure. In the inversion stage, these values resulted in a profile which intersected with the initial M_{OBS} estimate but failed to align with the upper SSC observations. On the contrary, for the 5 MHz transducer, the bottom part of the M_{OBS} profile was missed but the M_{ABS} estimates begin to converge with the upper M_{OBS} observations. For Figure (4.25), the predicted M_{ABS} values obtained for the 1 and 2 MHz transducers failed to match the profile from the OBS sensors. The divergence from the M_{OBS} estimates was more pronounced for the lower frequency transducers (1 and 2 MHz) relative to 4 and 5 MHz, where the M_{ABS} profile began to skew towards the OBS estimate at 0.4 m and continue ultimately towards the uppermost M_{OBS} estimate. The 4 and 5 MHz of Burst 40 (Figure 4.25) plus 5 MHz transducer of Burst 346 (Figure 4.24) related to the previous figures by tending to fit the upper water column M_{OBS} observations more whilst missing the M_{OBS} estimate closest to the bed (0.2 m).

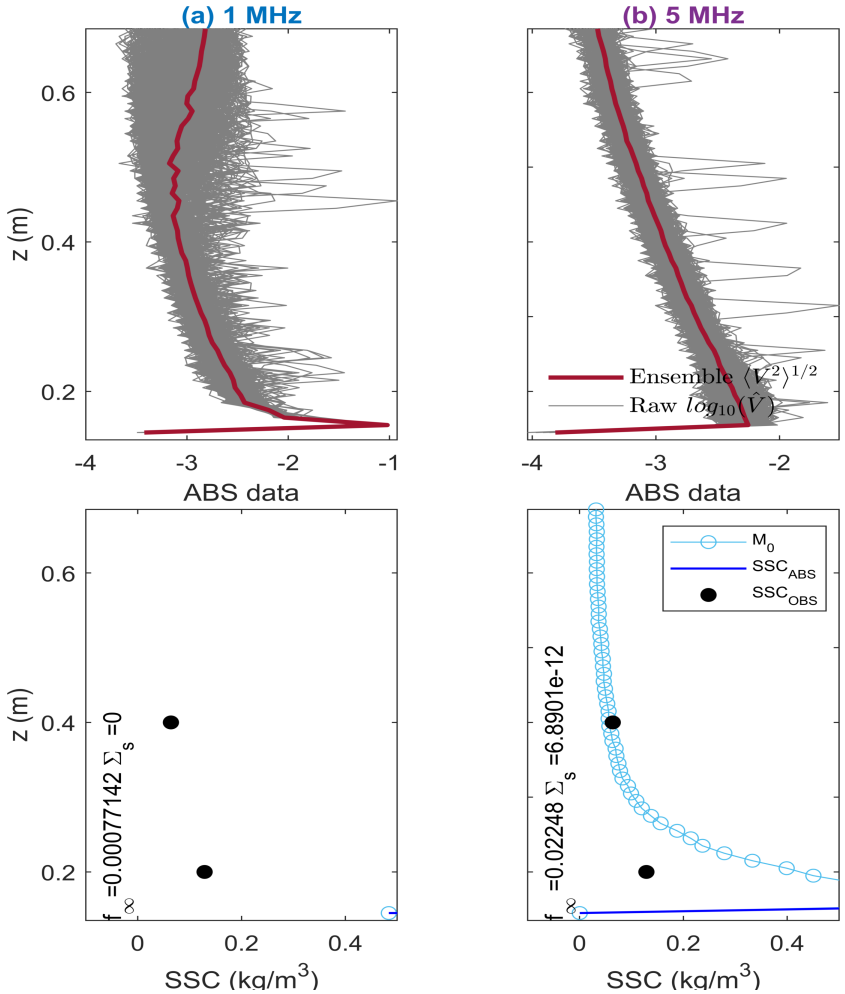

Figure 4.24: Vertical water column (z, (m)) starting at 0.135 m above the bed, where (A) was positioned showing the raw $log_{10}(\hat{V})$ (grey line) and ensemble averaged ($\langle V^2 \rangle^{1/2}$) ABS (brown line) for transducer frequencies (1 and 5 MHz, A) (a – b). Profiles of M_0 (light blue 'o'), and M_{ABS} (dark blue '-') are derived from the ensemble averaged individual f_∞ and Σ_s for each transducer, for Burst 346. The M_{OBS} measurements (black 'o') are shown at the relevant heights in the water column, for Burst 346 (08/11/21, 23:30:00).

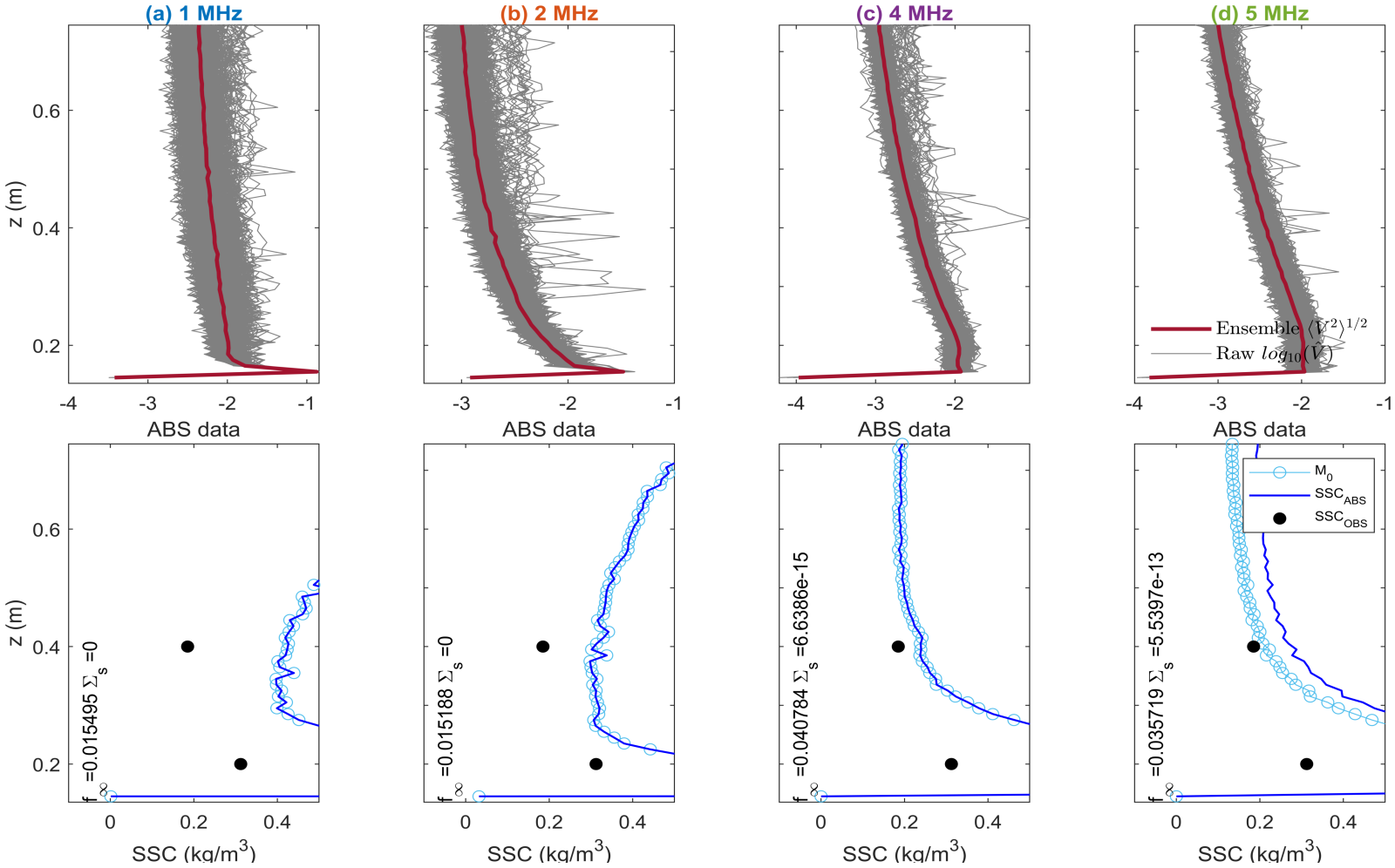

Figure 4.25: Vertical water column (z, (m)) starting at 0.135 m above the bed, where (A) was positioned showing the raw $log_{10}(\hat{V})$ (grey line) and ensemble averaged ($\langle V^2 \rangle^{1/2}$) ABS (brown line) for transducer frequencies (1, 2, 4, and 5 MHz, A) (a – d). Profiles of M_0 (light blue 'o'), and M_{ABS} (dark blue '-') are derived from the ensemble averaged individual f_∞ and Σ_s for each transducer, for Burst 40. The M_{OBS} measurements (black 'o') are shown at the relevant heights in the water column, for Burst 40 (06/11/21, 20:30:00).

For Figure (4.26) of Burst 120, of the four transducers presented – only 2 MHz fulfilled $R^2 > 0.95$, yet the 1, 4 and 5 MHz transducer M_{ABS} profiles appear to resolve the OBS measurements quite well. The 1 MHz transducer obtained the lowest R^2 value (Section 4.5.1) but the 4 and 5 MHz transducers both obtained higher R^2. However, for Figure (4.27) (Burst 415), were only 2 and 5 MHz surpassed the $R^2 > 0.95$ criteria, and indeed the 1 MHz transducer with the worst R^2 value of 0.018077 (Section 4.5.1) fail to produce an inversion result; however, the 4 MHz with $R^2 > 0.95$, nonetheless showed a very similar M_{ABS} profile to the adjacent 5 MHz M_{ABS} profile, which compared favorably to the M_{OBS}.

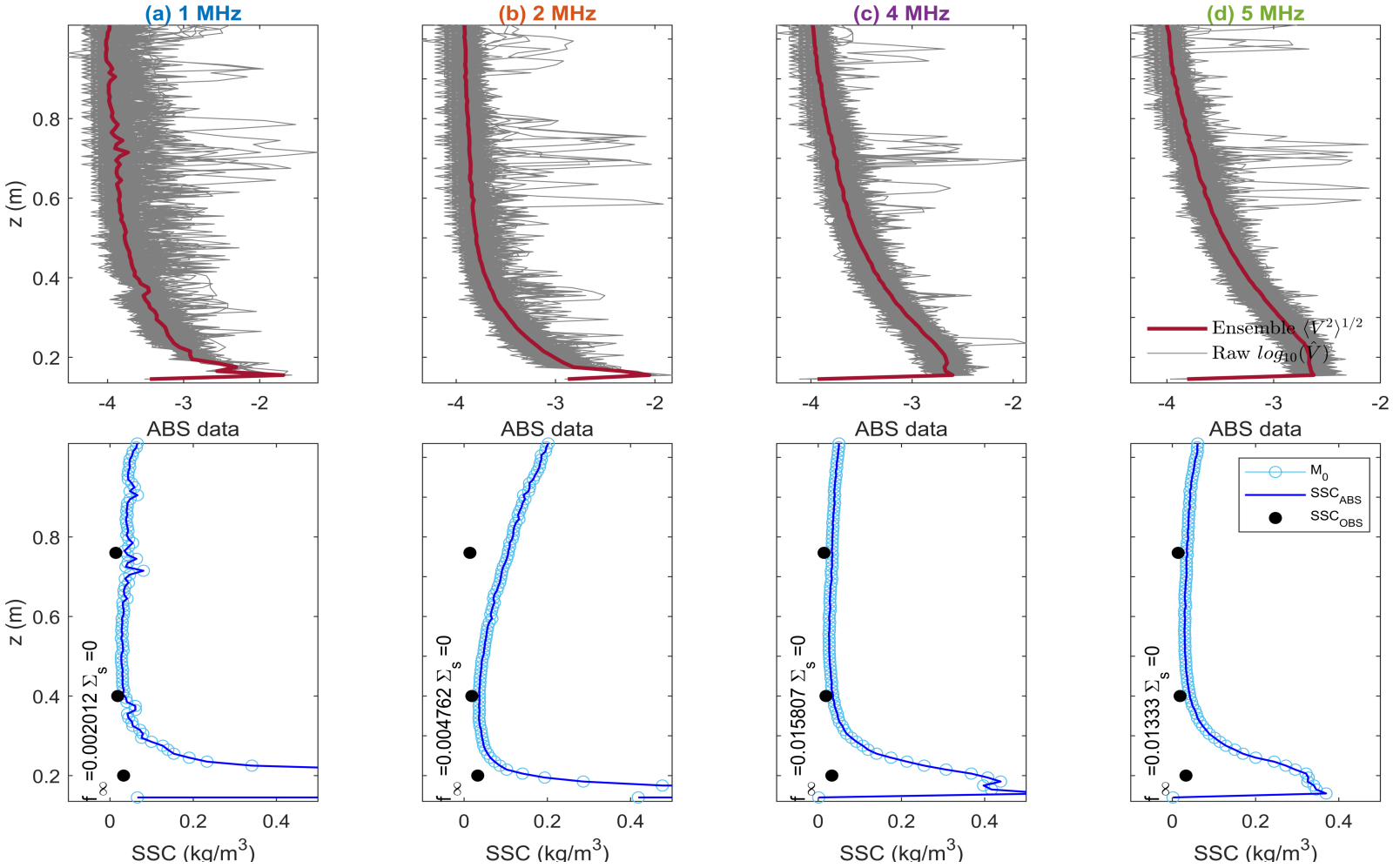

Figure 4.26: Vertical water column (z, (m)) starting at 0.135 m above the bed, where (A) was positioned showing the raw $log_{10}(\hat{V})$ (grey line) and ensemble averaged ($\langle V^2 \rangle^{1/2}$) ABS (brown line) for transducer frequencies (1, 2, 4, and 5 MHz, A) (a – d). Profiles of M_0 (light blue 'o'), and M_{ABS} (dark blue '-') are derived from the ensemble averaged individual f_∞ and Σ_s for each transducer, for Burst 40. The M_{OBS} measurements (black 'o') are shown at the relevant heights in the water column, for Burst 120 (07/11/21, 09:50:00).

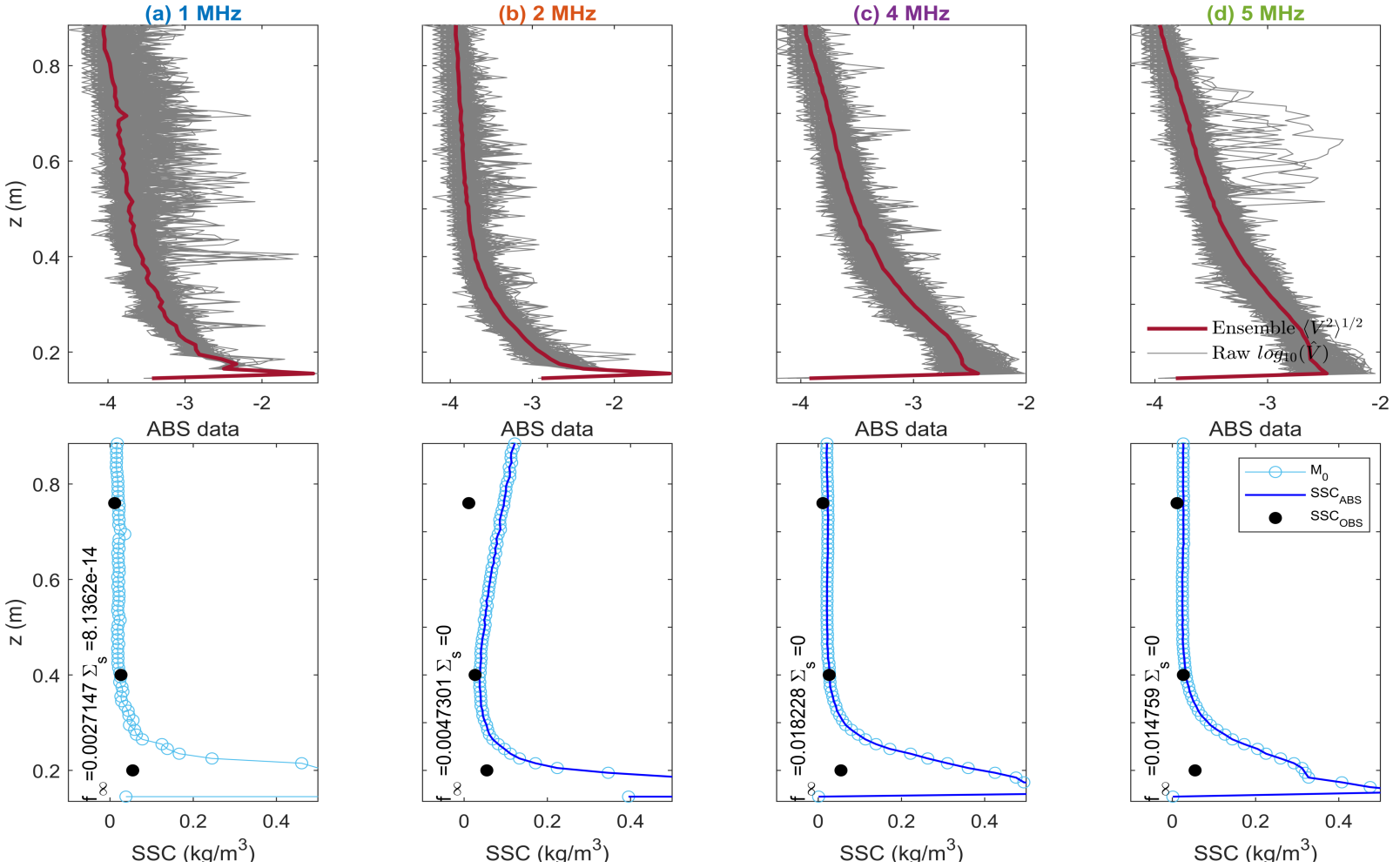

Figure 4.27: Vertical water column (z, (m)) starting at 0.135 m above the bed, where (A) was positioned showing the raw $log_{10}(\hat{V})$ (grey line) and ensemble averaged ($\langle V^2 \rangle^{1/2}$) ABS (brown line) for transducer frequencies (1, 2, 4, and 5 MHz, A) (a – d). Profiles of M_0 (light blue 'o'), and M_{ABS} (dark blue '-') are derived from the ensemble averaged individual f_∞ and Σ_s for each transducer, for Burst 415. The M_{OBS} measurements (black 'o') are shown at the relevant heights in the water column, for Burst 415 (09/11/21, 11:00:00).

The squared error (SE) between M_{ABS} and M_{OBS} estimates for the linear fit inversion method and the combined, sum of squared errors (SSE), at each height in the vertical profile coordinating to where the OBS instruments were positioned in the water column at the field site is represented in Figure (4.28) below for each transducer. As well as the number of OBS instrument heights used in the SSE calculation, which in the case of the linear fit derived M_{ABS} profiles, the water depth was $r > 0.5$ therefore, no SSE values were based on calculation from one height. Across all transducers, the errors appear to be lower, higher in the water column for OBS (0.4 and 0.76 m) and the error tended to increase with an increasing water depth or number of OBS height samples, due to greater SSE values overall.

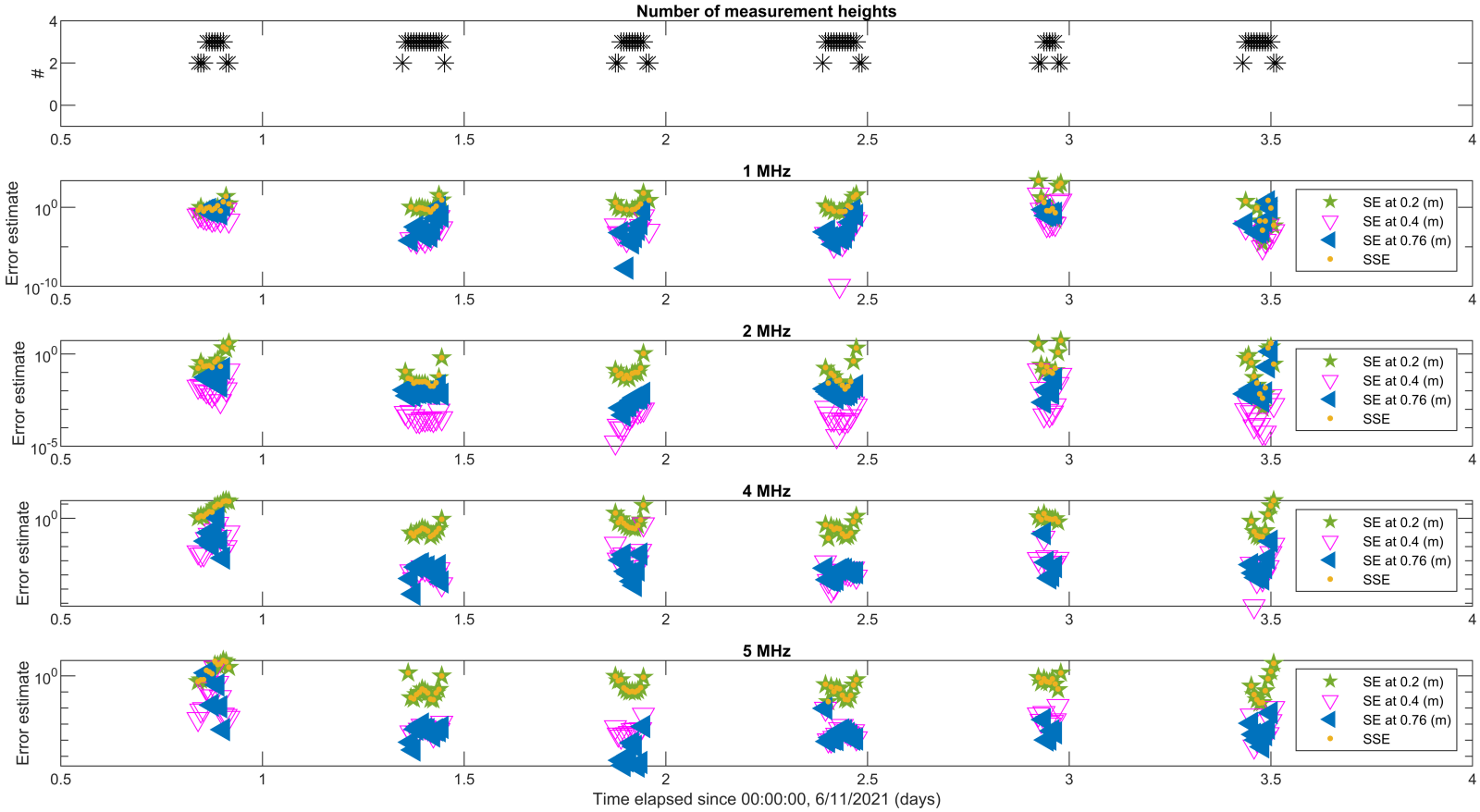

Figure 4.28: Time series of linear fit inversion method associated error between M_{ABS} and M_{OBS} profiles taken at each OBS field instrument deployment height at (m) above bed, per burst for each transducer (1, 2, 4, and 5 MHz).

4.6.2 Ensemble-average f_∞ and Σ_s analysis

In this section we explore a second method of inverting the ABS data, in which an average pair of f_∞ and Σ_s values are used. This average pair is simply the average of all individual f_∞ and Σ_s values (obtained for each burst) from inversion method 1.

The individual values for f_∞ and Σ_s (method 1) along with the average values (method 2) are shown in Figure (4.29) and summarised in Table (4.9). The values shown in Table (4.6) were then used in the inversion for all burst (for the corresponding frequency). The idea here is that we are exploring the sensitivity of the inversion to f_∞ and Σ_s and investigating if a single f_∞ and Σ_s pair is universally applicable.

Table 4.9: Average f_∞ and Σ_s for 1, 2, 4 and 5 MHz transducers (A) used in inversion method 2.

Transducers	1 MHz	2 MHz	4 MHz	5 MHz
[f_∞ and Σ_s]	[0.0117, 0]	[0.0060, 0]	[0.0295, 2.6956e-12]	[0.0232, 2.3448e-12]

The results from this approach are summarised in Figures (4.30) to (4.33), which corresponded to the same bursts shown in Figures (4.22) to (4.25).

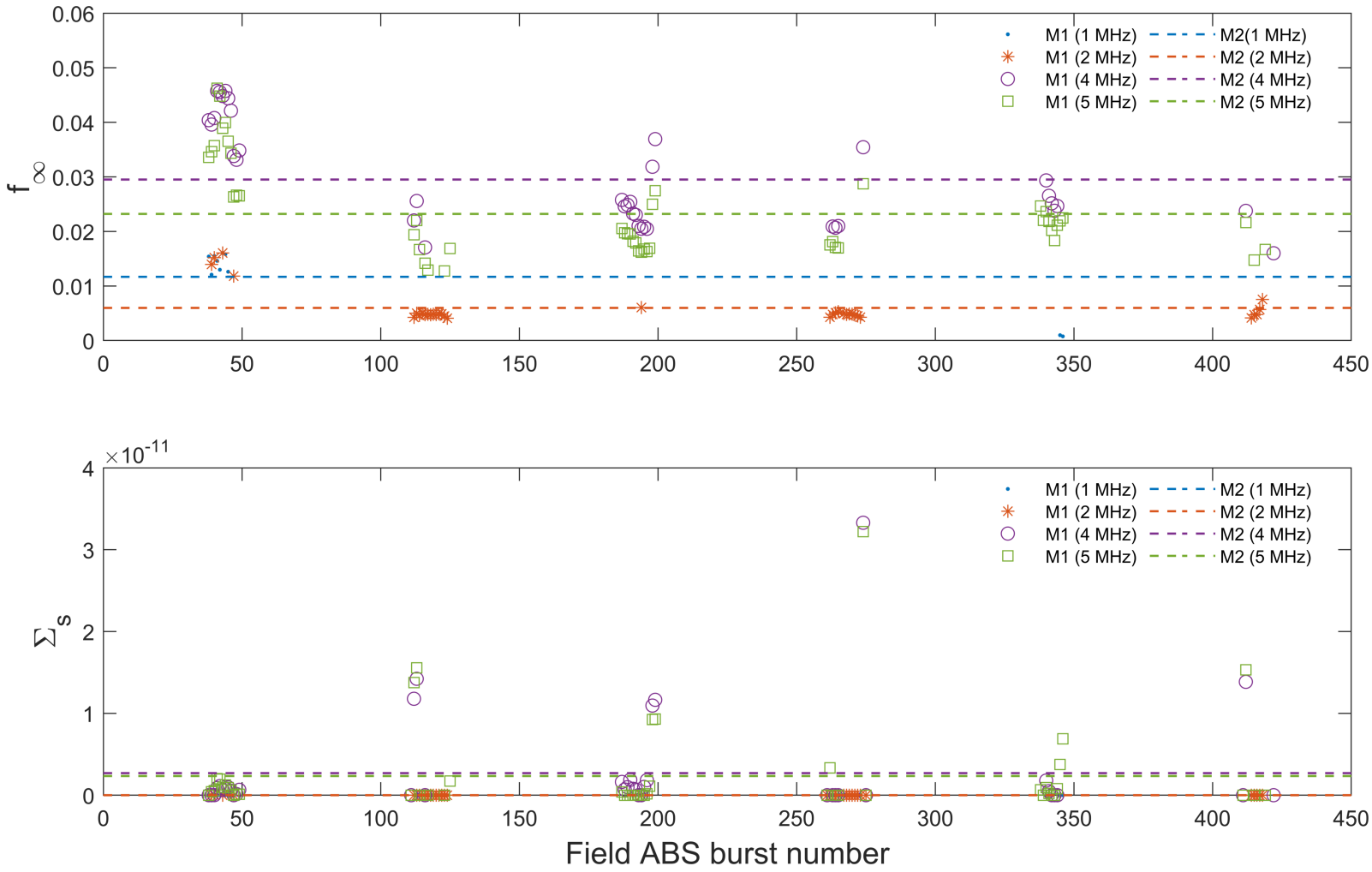

Figure 4.29: Individual, time-varying f_∞ and Σ_s values (method 1 (M1)) calculated from field bursts with $R^2 > 0.95$, and the average f_∞ and Σ_s values (method 2 (M2)) signaled by the dashed lines for each frequency (1, 2, 4, and 5 MHz transducers, A) (colours).

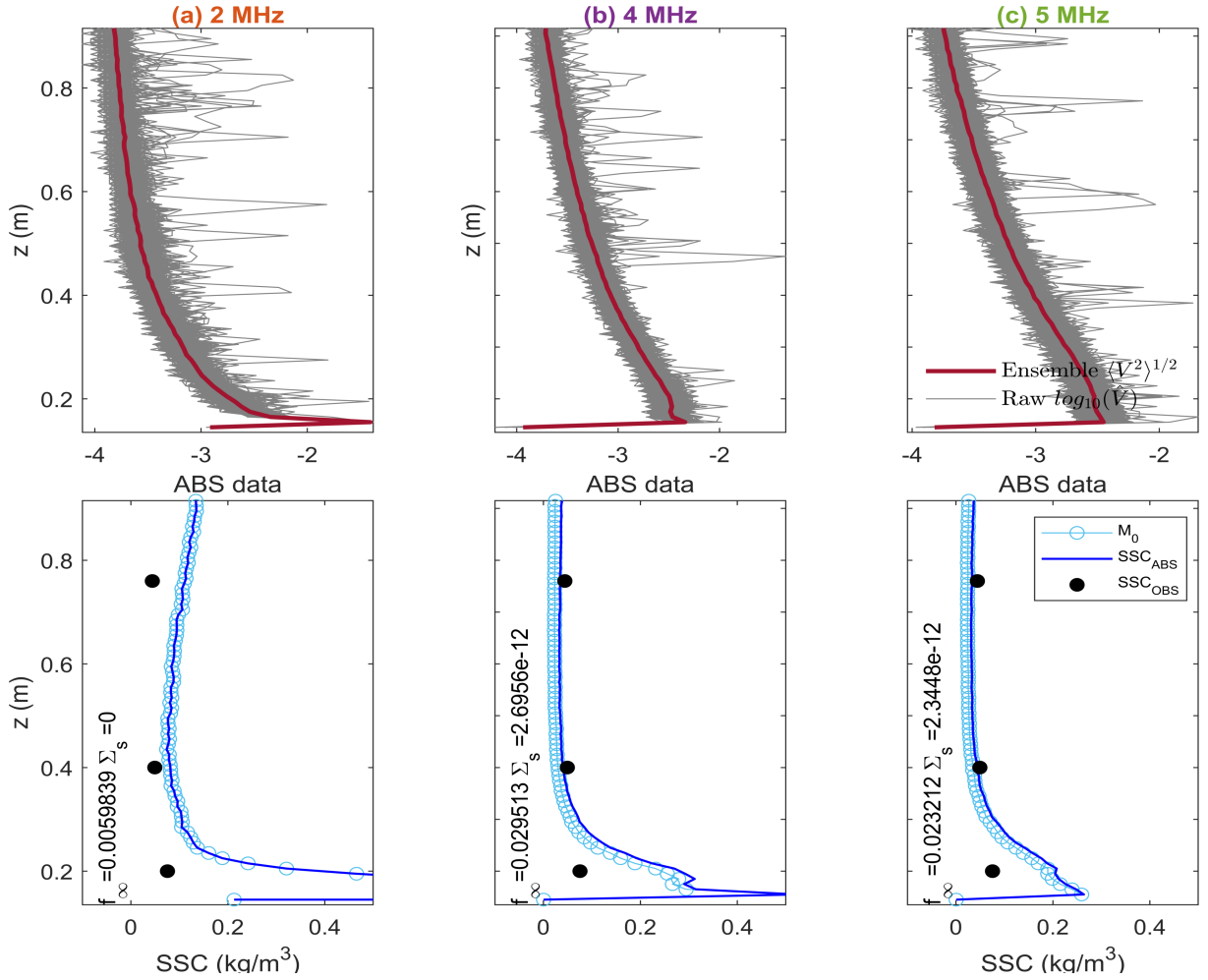

Figure 4.30: Vertical water column (z, (m)) starting at 0.135 m above the bed, where (A) was positioned showing the raw $log_{10}(\hat{V})$ (grey line) and ensemble averaged ($\langle V^2 \rangle^{1/2}$) ABS (brown line) for transducer frequencies (2, 4, and 5 MHz, A) (a – c). Profiles of M_0 (light blue 'o'), and M_{ABS} (dark blue '-') are derived from an averaged pair of f_∞ and Σ_s for each transducer, for Burst 194. The M_{OBS} measurements (black 'o') are shown at the relevant heights in the water column, for Burst 194 (07/11/21, 22:10:00).

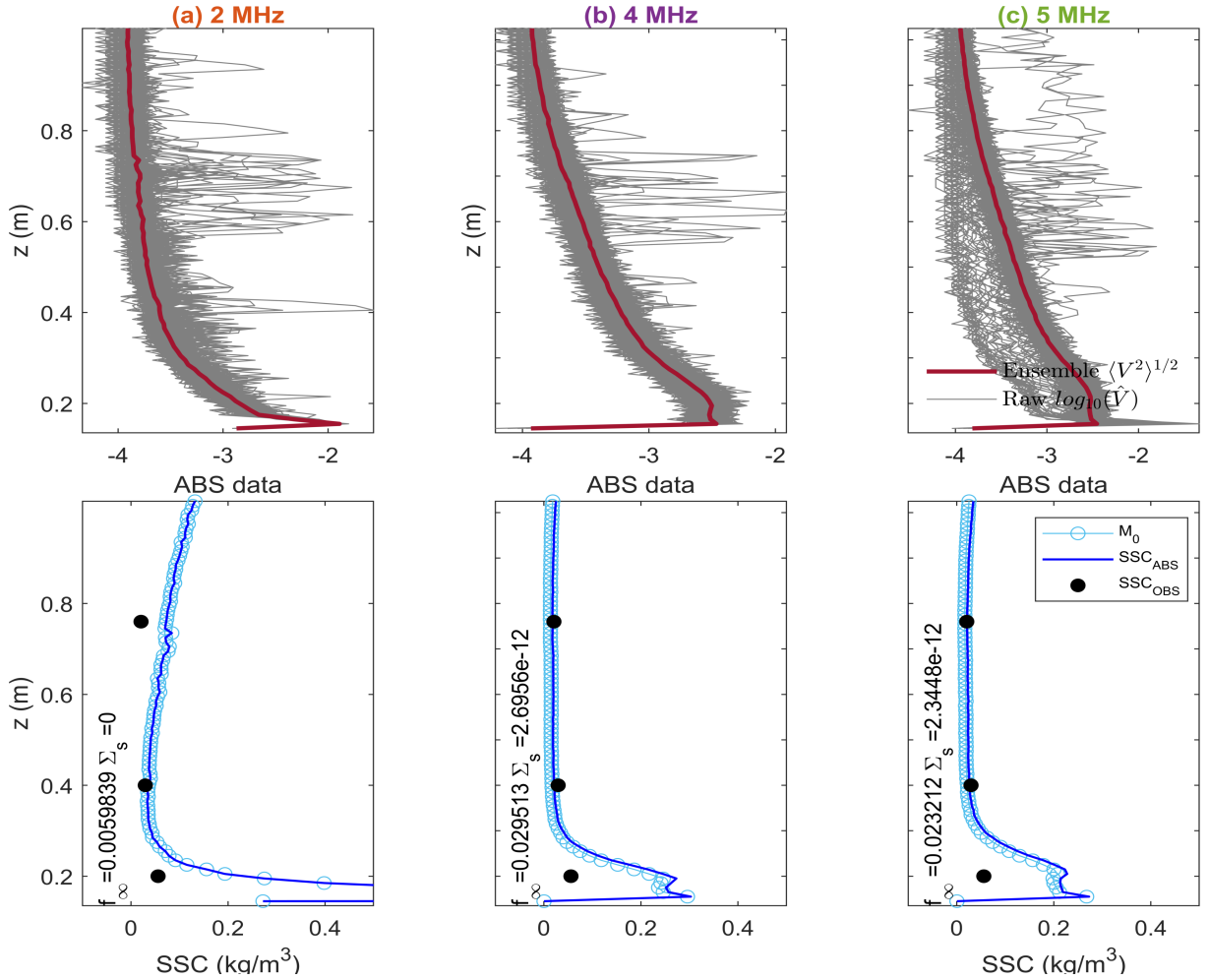

Figure 4.31: Vertical water column (z, (m)) starting at 0.135 m above the bed, where (A) was positioned showing the raw $log_{10}(\hat{V})$ (grey line) and ensemble averaged ($\langle V^2 \rangle^{1/2}$) ABS (brown line) for transducer frequencies (2, 4, and 5 MHz, A) (a – c). Profiles of M_0 (light blue 'o'), and M_{ABS} (dark blue '-') are derived from an averaged pair of f_∞ and Σ_s for each transducer, for Burst 265. The M_{OBS} measurements (black 'o') are shown at the relevant heights in the water column, for Burst 265 (08/11/21, 10:00:00).

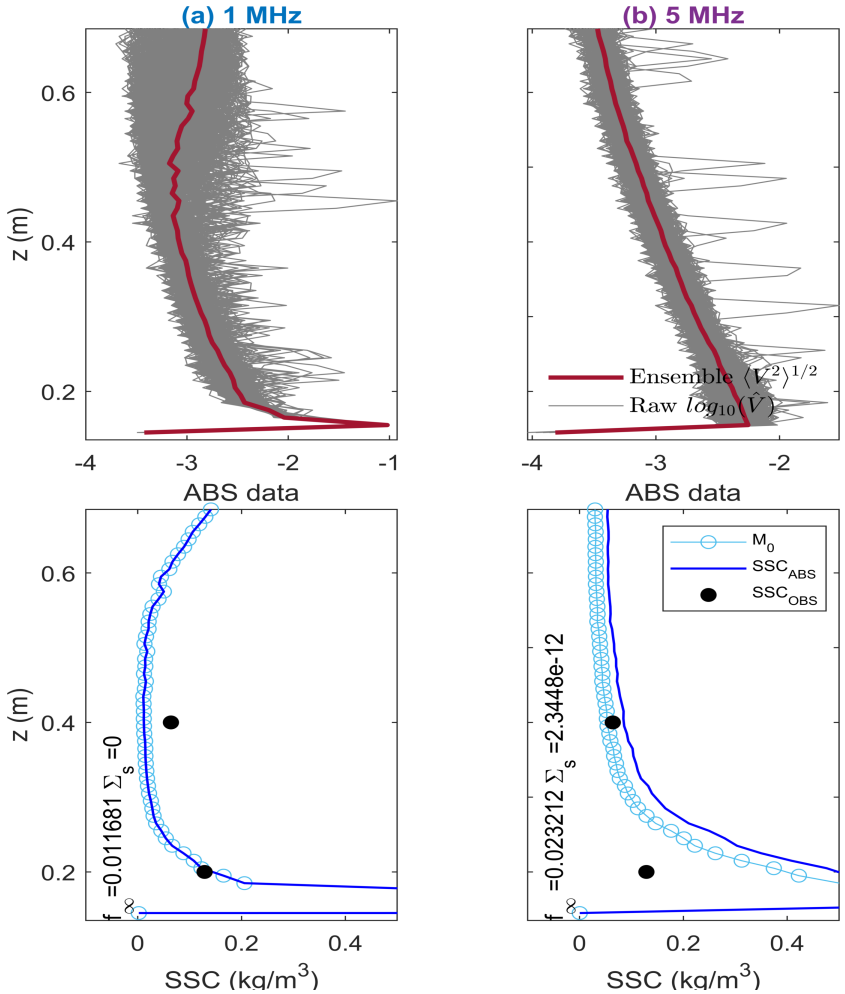

Figure 4.32: Vertical water column (z, (m)) starting at 0.135 m above the bed, where (A) was positioned showing the raw $log_{10}(\hat{V})$ (grey line) and ensemble averaged ($\langle V^2 \rangle^{1/2}$) ABS (brown line) for transducer frequencies (1 and 5 MHz, A) (a – b). Profiles of M_0 (light blue 'o'), and M_{ABS} (dark blue '-') are derived from an averaged pair of f_∞ and Σ_s for each transducer, for Burst 346. The M_{OBS} measurements (black 'o') are shown at the relevant heights in the water column, for Burst 346 (08/11/21, 23:30:00).

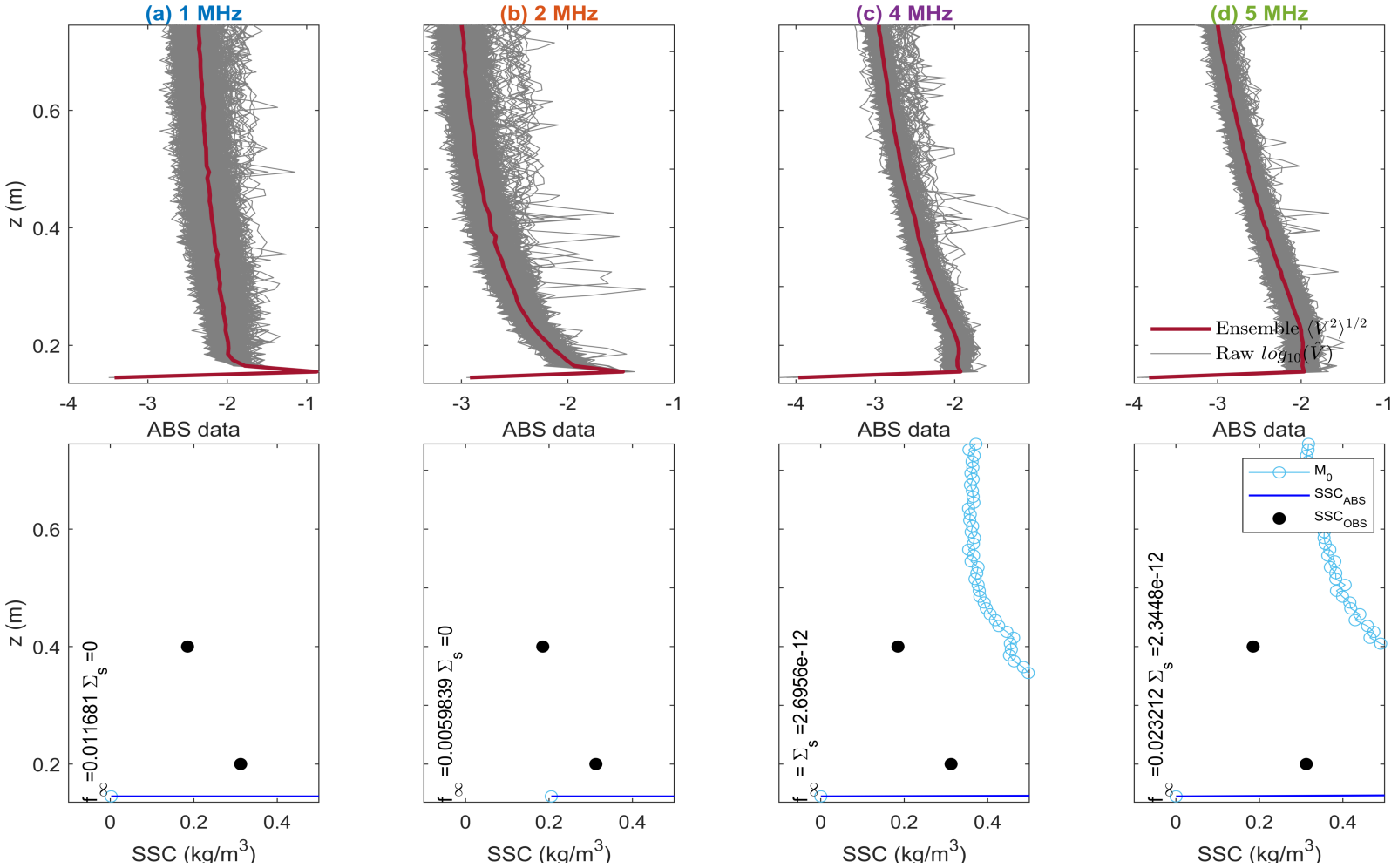

Figure 4.33: Vertical water column (z, (m)) starting at 0.135 m above the bed, where (A) was positioned showing the raw $log_{10}(\hat{V})$ (grey line) and ensemble averaged ($\langle V^2 \rangle^{1/2}$) ABS (brown line) for transducer frequencies (1, 2, 4, and 5 MHz, A) (a – d). Profiles of M_0 (light blue 'o'), and M_{ABS} (dark blue '-') are derived from an averaged pair of f_∞ and Σ_s for each transducer, for Burst 40. The M_{OBS} measurements (black 'o') are shown at the relevant heights in the water column, for Burst 40 (06/11/21, 20:30:00).

Figures (4.30) and (4.31) (burst 194 and 265) showed the inversion results that best matched the M_{OBS} estimations. For these bursts, M_{ABS} in the mid to upper part of the water column was better matched to the M_{OBS} concentrations than M_{ABS} estimates from lower in the water column. The discrepancies between estimated M_{ABS} profiles derived from this inversion are related to the difference in the individually calculated per burst, f_∞ and Σ_s values (method 1) and the averaged values used here (Table 4.9). At burst times when there was a reasonable agreement between the M_{ABS} and the M_{OBS} profiles, the f_∞ average values for the 2, 4 and 5 MHz transducers were very close to the individually calculated f_∞ like for bursts 194 and 265 (Figures 4.30 and 4.31).

The approximate error estimates between the M_{ABS} and the M_{OBS} profiles for this average inversion method are presented in Figure (4.34), and are similar to the trend observed in Figure (4.28), with larger errors between the predicted M_{ABS} and the measured M_{OBS} calculated lower in the water column. Also shown in Figure (4.34), are a worse set of SE and SSE for the 1 and 2 MHz transducers, specifically during the first tidal cycle.

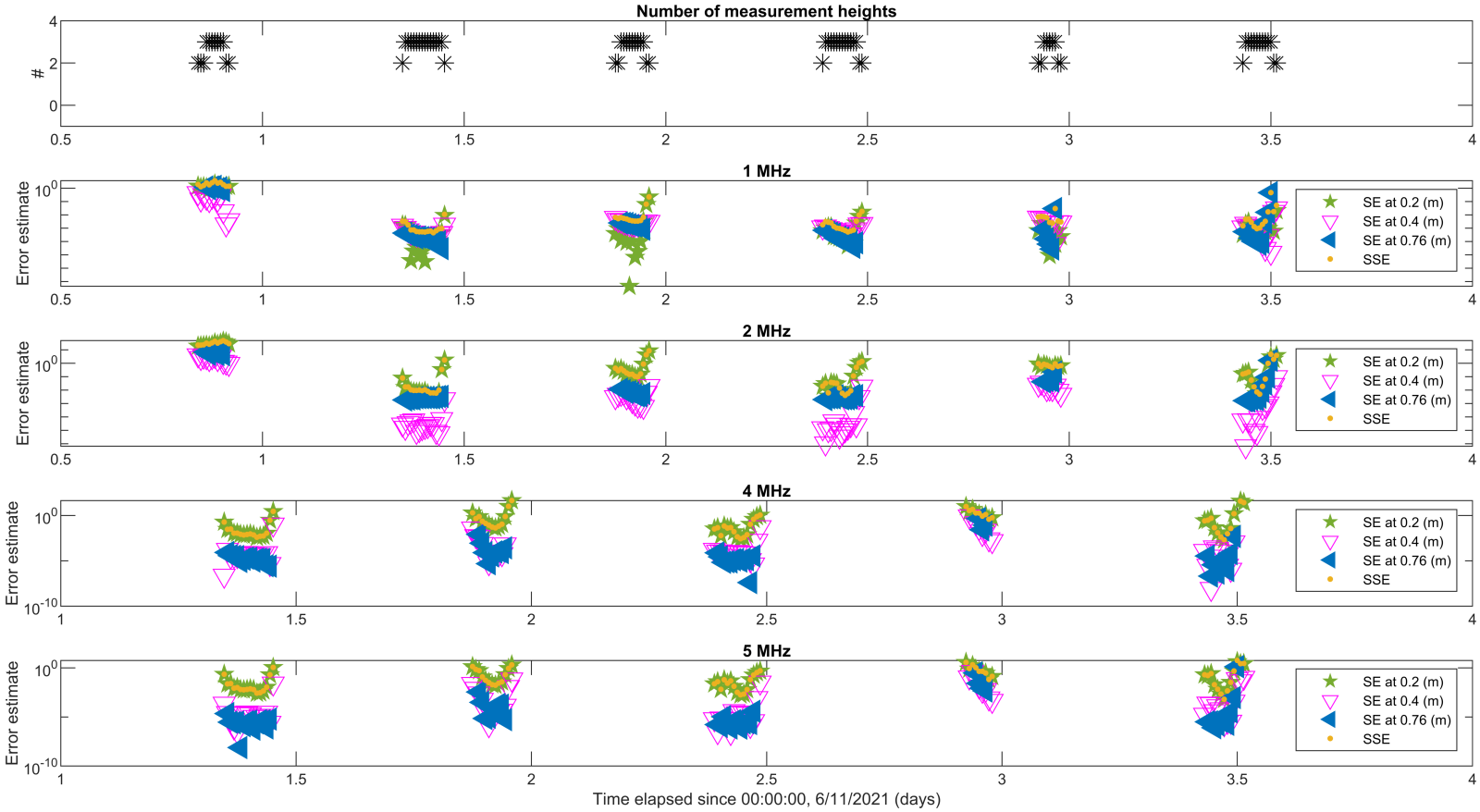

Figure 4.34: Time series of average inversion method associated error between M_{ABS} and M_{OBS} profiles taken at each OBS field instrument deployment height at (m) above bed, per burst for each transducer (1, 2, 4, and 5 MHz)

Chapter 5

Discussion

This thesis explored a relatively new method for calibration of acoustic transducers to an off-the-shelf ABS instrument. Calibration results were then used to invert the acoustic backscatter signal obtained in a field experiment at the Firth of Thames, to obtain estimates of suspended sediment concentrations along a vertical profile.

The UNISENSE 3D Motorised Micromanipulator was found to be a robust positioning and conveyor system for the single sphere calibration procedure. The automated execution of the grid-wise experiments programmed by the Micromanipulator, minimised the risk of human error from manually operating the Micromanipulator supporting the tungsten ball in 2.5 mm step motions in both the z and x axes. This experimental apparatus design was comparable to the movable stage used in the calibration study of a fixed tungsten carbide ball by Wilson and Hay (2017). The high quality fit of the theoretical expression to the data in the directivity Equation (2.2) (Section 2.2.1) for all frequencies, indicates this resolution was probably sufficient for the determination of the effective transducer radii (which were all close to the nominal values provided by the instrument manufacturer).

K_{TR} was expected to vary between the contrasting MHz frequencies from the differing sets of transducers used across both ABS instruments, a result col-

lated in Table (4.6) and (4.7) (Section 4.4). Both ABS laboratory calibration methods were undertaken using a 2.5 mm pulse length for the beam path, which allowed for direct comparison between the two sets of K_{TR} terms. Similarly, the lack of a significant trend or deviation of K_{TR} with range across the glass bead suspension experiments (Section 4.3.2, Figures 4.8 and 4.9) was an observation aligned with the experimental results of Betteridge et al. (2008). As a result, Betteridge et al. (2008) drew the conclusion that the suspension was homogenous. Their conclusion, also applicable to this study, supported the calculation of an average K_{TR} value for each transducer from the ballotini bead suspension experiments. Comparison of the two sets of K_{TR} terms from the single sphere and particle suspension experiments, the error margins ranged from 4.8 to 43.45%. The precise reasons for the differences between the two different estimates of K_{TR} constants are unknown; however, there may be several factors contributing to the difference which are detailed below.

For the tungsten carbide ball experiments, a grid step size of 2.5 mm may have been too coarse to resolve the position of the absolute maximum ABS peak in the 'rigid return' bin. Further experiments using the same process but with a smaller grid increment or larger tungsten ball may help to fine tune these results. This technique builds on the short pulse methodology of Wilson and Hay (2017), in refining estimation of the K_{TR} term.

Additionally, assumptions and simplifications were made in determining variables used in the calculation of K_{TR} (Equation 2.22). The glass ballotini beads may not have been exactly spherical in shape, perhaps misfitting the analytical solution. The experiments with glass beads also rely on the assumption of a perfectly homogenous suspension throughout the tank and over time.

Any inaccuracies in the values of K_{TR} will propagate through the inversion analyses into concentration M_{ABS} estimates. Given the greater level of ex-

perimental control over the single target experiments, these K_{TR} were used in the subsequent inversion. Despite the uncertainty, the inverted M_{ABS} profiles from the processed field bursts of Section (4.6), for both inversion methods (see Section 4.6.1 and Section 4.6.2), generally agreed with the M_{OBS} estimates.

After laboratory calibration of the ABS instruments, A and B, the burst-averaged ABS data gathered from the water column at the field site was used to estimate the scattering characteristics f_∞ and Σ_s of the particles in the field. These values were used to address the important question, whether there exist universal set of f_∞ and Σ_s values which function effectively to invert ABS field data and generate accurate SSC estimates. The intercept c and gradient m, derived from the direct linear fit plots of the $\ln\left(r\langle V^2\rangle^{1/2}\right)$ were used in the calculation of the unknown f_∞ and Σ_s for the particles suspended in the field site, noting those calculations also use the laboratory-derived K_{TR} values along with the SSC estimates derived for the OBS, an assumed a of $4\mu m$ and a nominal density ρ_s of 2600 kg/m^3.

The estimates of f_∞ and Σ_s values generally exhibited u-shaped curves with greater values at low water depths at the start and the end of the tide (Figure 4.20). The f_∞ was generally bigger during the first tide relative to the later part of the experiment, reflecting the change from more energetic to less energetic conditions. Indicating a possible change in the scattering nature of the suspended particles. These c and m coefficient results likely reflect the hydrodynamic conditions at the field site where an unusual lack of wave energy (Lovett, 2017) from days two to four, stimulated insufficient SSC quantities for significant attenuation of the sound per m. On the contrary, the differing c values on day one of field recording compared to the rest of the measurement period was likely due to a period of increased surface wave activity and entrainment of particles in suspension of a different shape or size. The advantage to the field conditions was, the environment was more conducive for estimating

the f_∞ from the backscatter of the suspended particles. Indeed, Wilson and Hay (2017) suggest two sets of measurement conditions are required to obtain reliable estimates of f_∞ and Σ_s. Specifically, estimating f_∞ in a low particle concentration at a narrow range versus estimating Σ_s from a high particle concentration over a broad interval range. In addition, the f_∞ values depend on the speed of sound which is slower in cooler temperatures, which if not accounted for could be a potential source of error.

Results using the time-varying f_∞ and Σ_s terms (calculated for each processed burst file in which the total range, $r > 0.5\,\text{m}$ and $R^2 > 0.95$) in the inversion process (Section 2.3.1), demonstrated on many occasions, the resulting M_{ABS} profile was able to reasonably represent the measurements obtained from the OBS sensors (Figures 4.22 and 4.23). In some cases, the M_{ABS} better matched the upper M_{OBS} measurements (Figure 4.25) than the low other ones, a result illustrated in Figure (4.28). These results most likely reflect how f_∞ and Σ_s were derived. Recall that f_∞ and Σ_s where in part derived using the M_{OBS} estimates collected at the two upper most locations in the water column. Hence, the derived values of f_∞ and Σ_s appear to be a better representation of the scattering characteristics in the upper part of the water column compared to the lower part, this in turn implies that f_∞ and Σ_s may vary through the water column. This could reflect vertical changes in the nature (size, shape, density) of the particles in suspension. There were also a few cases, for which the inversion routine simply does not perform well (Figure 4.24 and 4.25). For these scenarios, 1 and 2 MHz tended to perform worse than the 4 and 5 MHz transducers. This result questioned whether the acoustic sensitivity of the 1 and 2 MHz frequencies to the particles in suspension was sufficient to produce a valid estimates of f_∞ and Σ_s and hence M_{ABS} obtained from the inversion. The above observation relates to scattering efficiency that varies as a function of frequency as it depends on the ratio on the acoustic wavelength to the size of particles in suspension (Sahin et al., 2020).

The sensitivity of the inversion results to the values used for the form function and total cross section scattering area, f_∞ and Σ_s, respectively was examined. The mean values across the duration of the experiment were calculated from those derived for each burst (as in Section 4.5.1) and the inversion procedure was undertaken using the mean values (Section 4.6.2). Results of the inversion were variable: at times the M_{ABS} of the suspension agreed with the M_{OBS} observations within the water column (Figures 4.30 and 4.31), but the bottom M_{OBS} were not well predicted by M_{ABS} estimates (Figure 4.32). A result, summarised in Figure (4.34). Notably, the M_{ABS} values were closer to M_{OBS} observations when the average scattering properties were close to the f_∞ and Σ_s values derived for that specific burst (Figures 4.30 and 4.31). While at other times, the inverted M_{ABS} profiles diverged from the M_{OBS} profiles (Figure 4.33). The inconsistency in the M_{ABS} profiles over the experiment series via the average scattering properties, implies over time there are changes in sediment properties such as particle size, or inherent changes to the nature of the scattering particles. In the case of Figure (4.33) (Burst 40), from tide 1, which occurred during a period of increased wave activity compared to the following days and subsequent burst times, the average f_∞ and Σ_s did a particularly poor job in producing an accurate, M_{ABS} profile. Thus, we conclude that the use of a single pair of universal f_∞ and Σ_s scattering properties is not recommended.

The present analysis used the simplification that the particle radius a and density ρ_s were equivalent to those of the primary particles in suspension, and these primary particles were the same as the bed sediment material. Consequently, the derivation of f_∞ and Σ_s and the sequent inversion neglects the process of flocculation and presence of floc constituents, which may alter the suspended particle size distribution over time. However, given the cohesive nature of the sediment, it is highly likely flocs were present in the water col-

umn at some points in the tidal cycle, consistent with observations from other studies at this location (Lovett, 2017). Keeping in mind, a recent study by Fromant et al. (2017) expanded on the effect of flocs in the inversion of ABS data, by factoring a mean porosity value over the particle size distribution into the backscattering model. In addition, it is likely the suspension contained a distribution of particle sizes different to the radii of the disaggregated bed sediment. Temporal fluctuations in particle size distribution or a composition of bimodal particles of sand, silt and clay are common in rivers like the setting studied by Vergne et al. (2020). Future work should consider this. Nonetheless, when considering all the simplifications made, the potential for experiment error, and the inherent difficulty associated with in-situ estimates of SSC the inversion methods 1 and 2 still performed reasonably well for many bursts, in generating reliable profiles of SSC.

Another possible approach to determining f_∞ and Σ_s without using the linear fit method (Section 4.5.1), is to find values per burst of f_∞ and Σ_s that minimize the difference between the results from the M_{OBS} measurements and the estimates M_{ABS} derived from the inversion. The results are presented in Figures (5.1) to (5.4) for the same bursts discussed previously.

In contrast to the results of the first two inversion methods (Section 4.6), the inversion results across all Figures from (5.1) to (5.4) showed a close match between M_{ABS} and M_{OBS} profiles, particularly for the bottom measurement location (0.2 m). Burst 194 and 265 of Figure (5.1) and (5.2), produced a tight M_{ABS} profile along the water column in line with the M_{OBS} measurements. However, all M_{ABS} profiles for all transducers, experienced an unrealistic increase in predicted SSC in the upper water column when reaching 0.9 – 1 m. The results shown in Figures (5.3) and (5.4) show a similar trend, in that M_{ABS} agrees nicely with the M_{OBS} in the lower part of the water column, but "blows up" producing unrealistic SSC estimates.

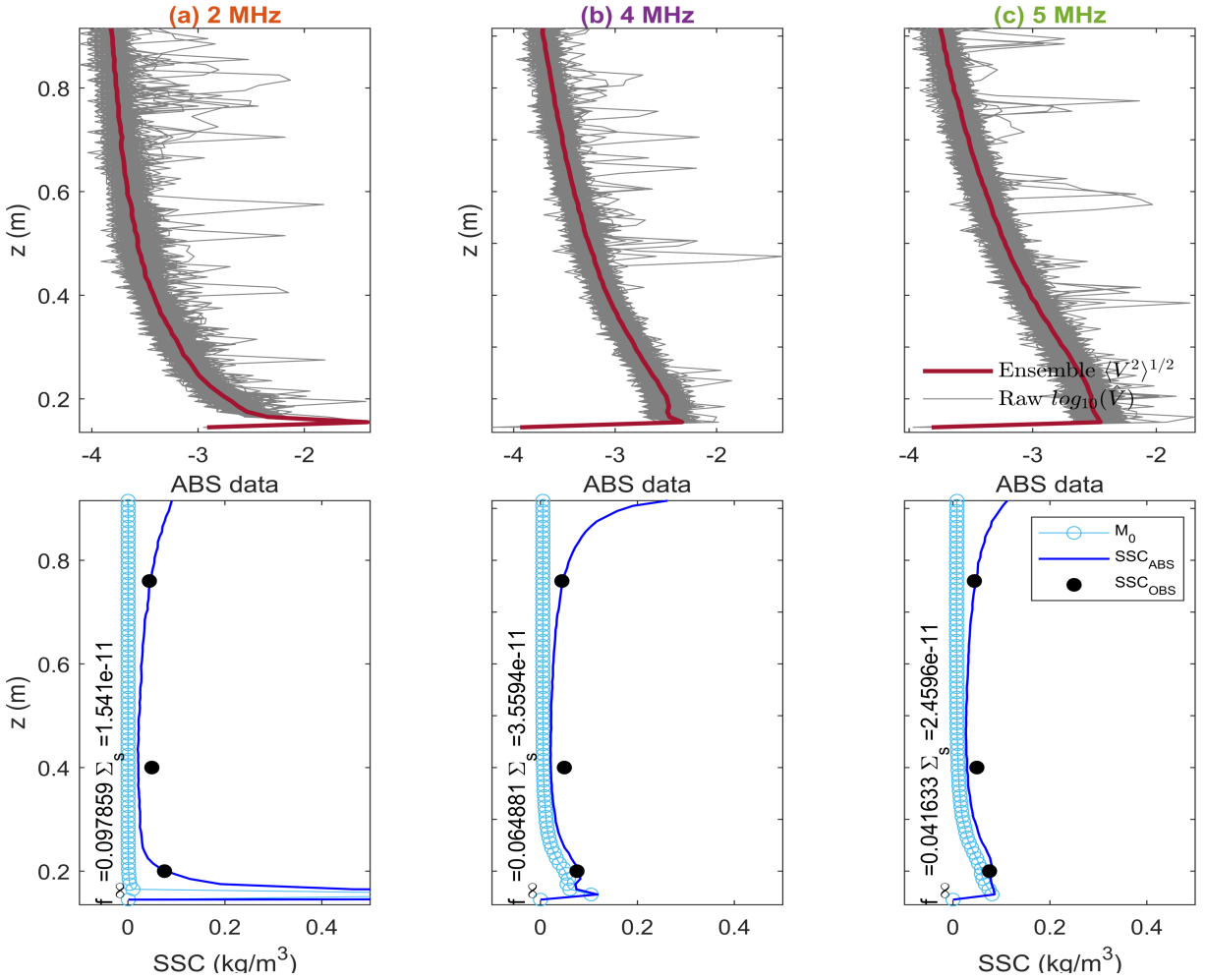

Figure 5.1: Vertical water column (z, (m)) starting at 0.135 m above the bed, where (A) was positioned showing the raw $log_{10}(\hat{V})$ (grey line) and ensemble averaged ($\langle V^2 \rangle^{1/2}$) ABS (brown line) for transducer frequencies (2, 4, and 5 MHz, A) (a – c). Profiles of M_0 (light blue 'o'), and M_{ABS} (dark blue '-') are derived from an optimised pair of f_∞ and Σ_s for each transducer, for Burst 194. The M_{OBS} measurements (black 'o') are shown at the relevant heights in the water column, for Burst 194 (07/11/21, 22:10:00).

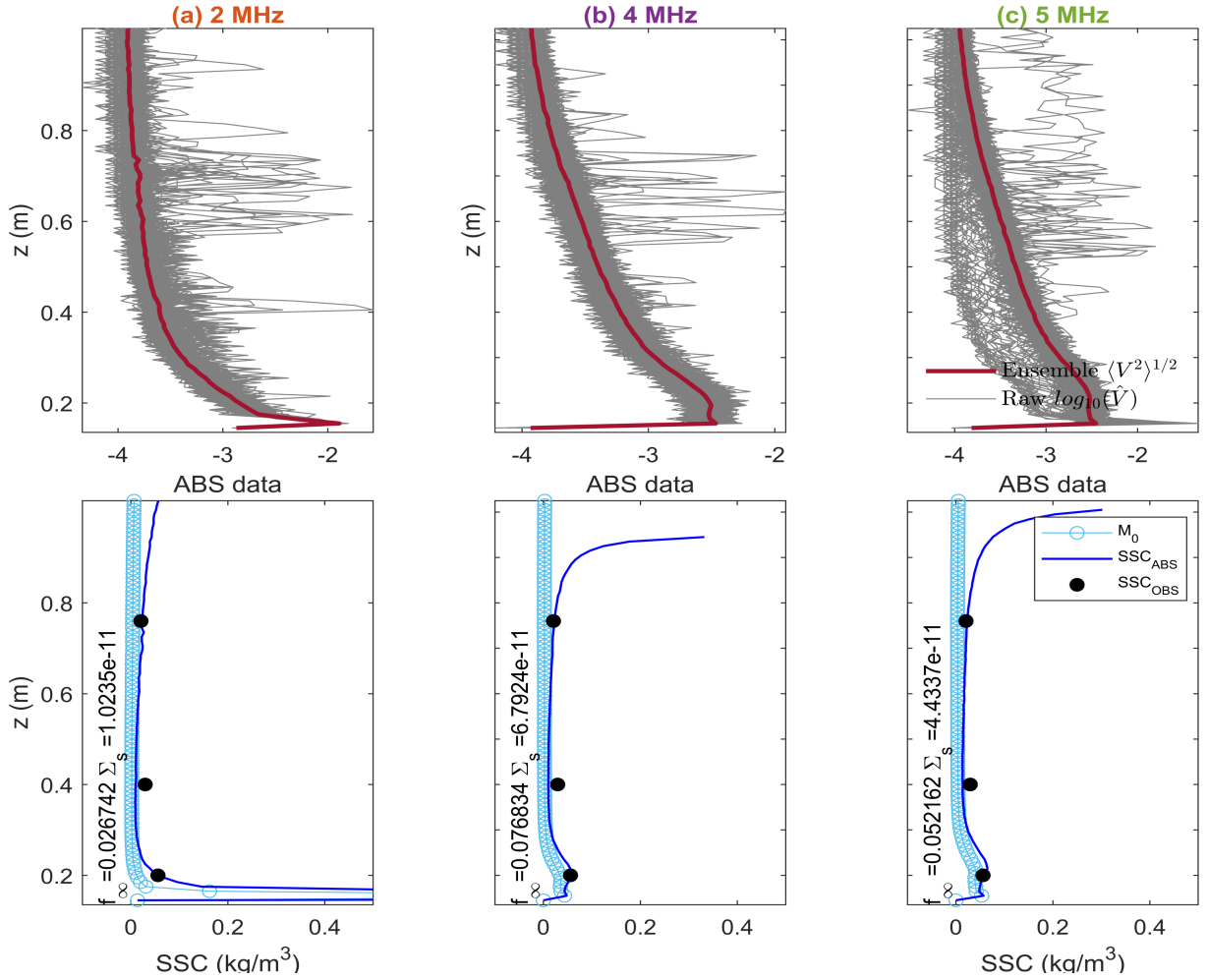

Figure 5.2: Vertical water column (z, (m)) starting at 0.135 m above the bed, where (A) was positioned showing the raw $log_{10}(\hat{V})$ (grey line) and ensemble averaged ($\langle V^2 \rangle^{1/2}$) ABS (brown line) for transducer frequencies (2, 4, and 5 MHz, A) (a – c). Profiles of M_0 (light blue 'o'), and M_{ABS} (dark blue '-') are derived from an optimised pair of f_∞ and Σ_s for each transducer, for Burst 265. The M_{OBS} measurements (black 'o') are shown at the relevant heights in the water column, for Burst 265 (08/11/21, 10:00:00).

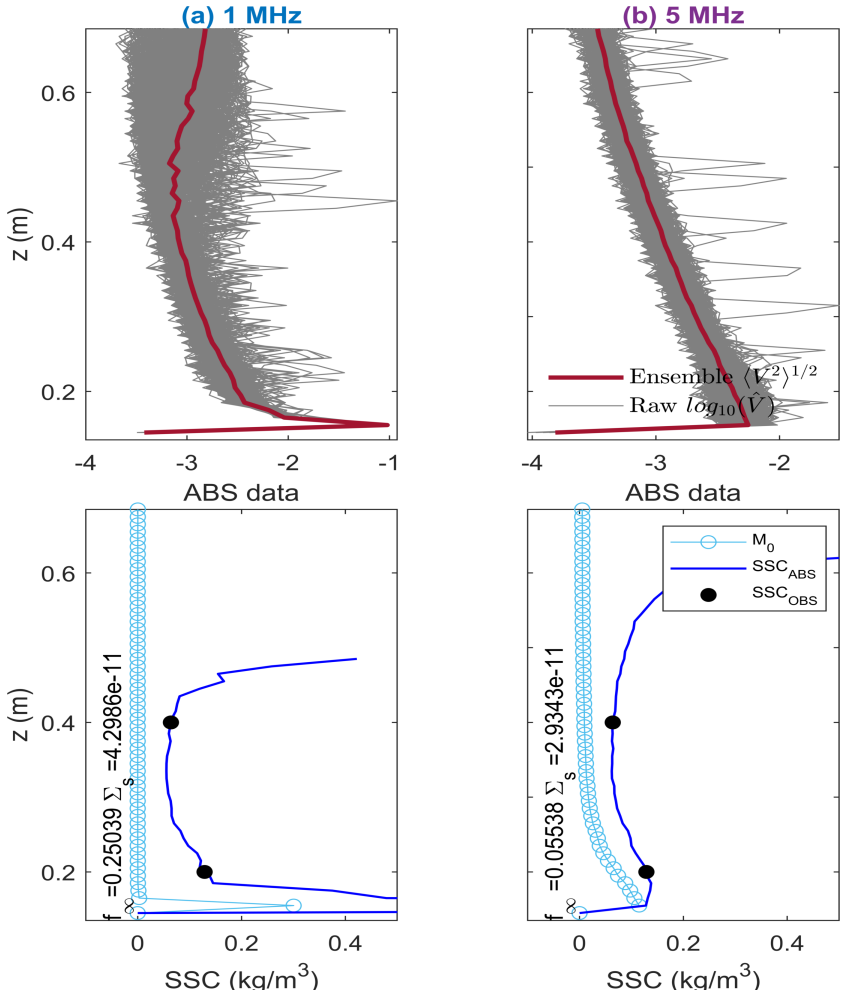

Figure 5.3: Vertical water column (z, (m)) starting at 0.135 m above the bed, where (A) was positioned showing the raw $log_{10}(\hat{V})$ (grey line) and ensemble averaged ($\langle V^2 \rangle^{1/2}$) ABS (brown line) for transducer frequencies (1 and 5 MHz, A) (a – b). Profiles of M_0 (light blue 'o'), and M_{ABS} (dark blue '-') are derived from an optimised pair of f_∞ and Σ_s for each transducer, for Burst 346. The M_{OBS} measurements (black 'o') are shown at the relevant heights in the water column, for Burst 346 (08/11/21, 23:30:00).

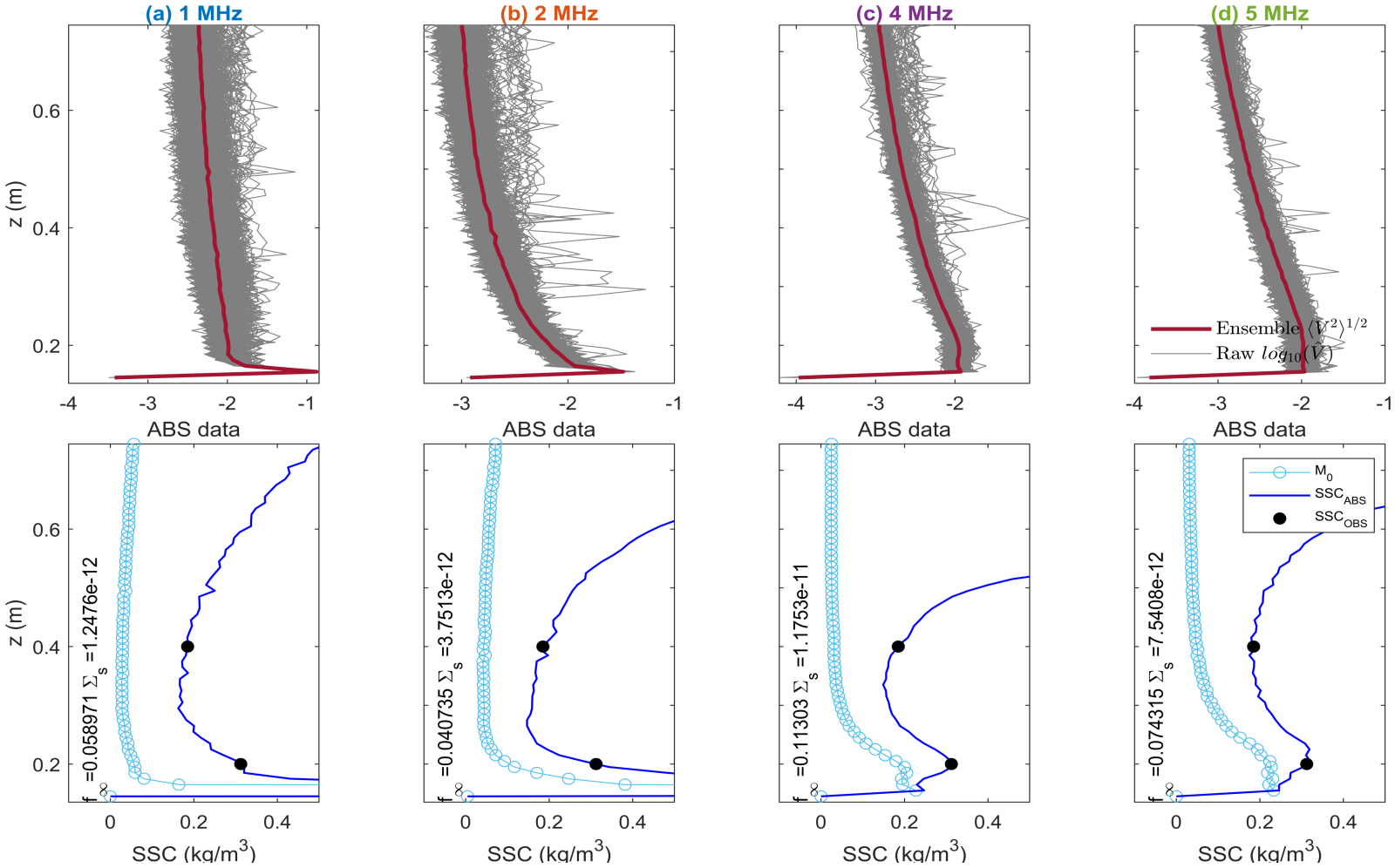

Figure 5.4: Vertical water column (z, (m)) starting at 0.135 m above the bed, where (A) was positioned showing the raw $log_{10}(\hat{V})$ (grey line) and ensemble averaged ($\langle V^2 \rangle^{1/2}$) ABS (brown line) for transducer frequencies (1, 2, 4, and 5 MHz, A) (a – d). Profiles of M_0 (light blue 'o'), and M_{ABS} (dark blue '-') are derived from an optimised pair of f_∞ and Σ_s for each transducer, for Burst 40. The M_{OBS} measurements (black 'o') are shown at the relevant heights in the water column, for Burst 40 (06/11/21, 20:30:00).

A likely explanation to this recurrent "blowing up" result is the fine tuning of the f_∞ and Σ_s values to suit the bottom M_{OBS} concentrations in this inversion method (3); caused the summed attenuation in the iterative stage to assume a higher Σ_s value than present in the upper water column. This argument is supported by the representative Σ_s values of the particle suspension, which lies between the linear fit inversion method (1) (see Section 4.6.1) and the optimised scattering characteristics inversion method (3).

For the optimised f_∞ and Σ_s inversion method discussed, the error between the calculated M_{ABS} profile and M_{OBS} measured profile (Figure 5.5), is the opposite of the error trends noted for the last two inversion methods (Sections 4.6.1 and 4.6.2). The M_{ABS} estimates obtaining the greatest error relative to the M_{OBS} observations, are from higher in the water column. As a result of this method's direct modifying of the f_∞ and Σ_s scattering properties, to better reflect the M_{OBS} measurements from lower in the water column.

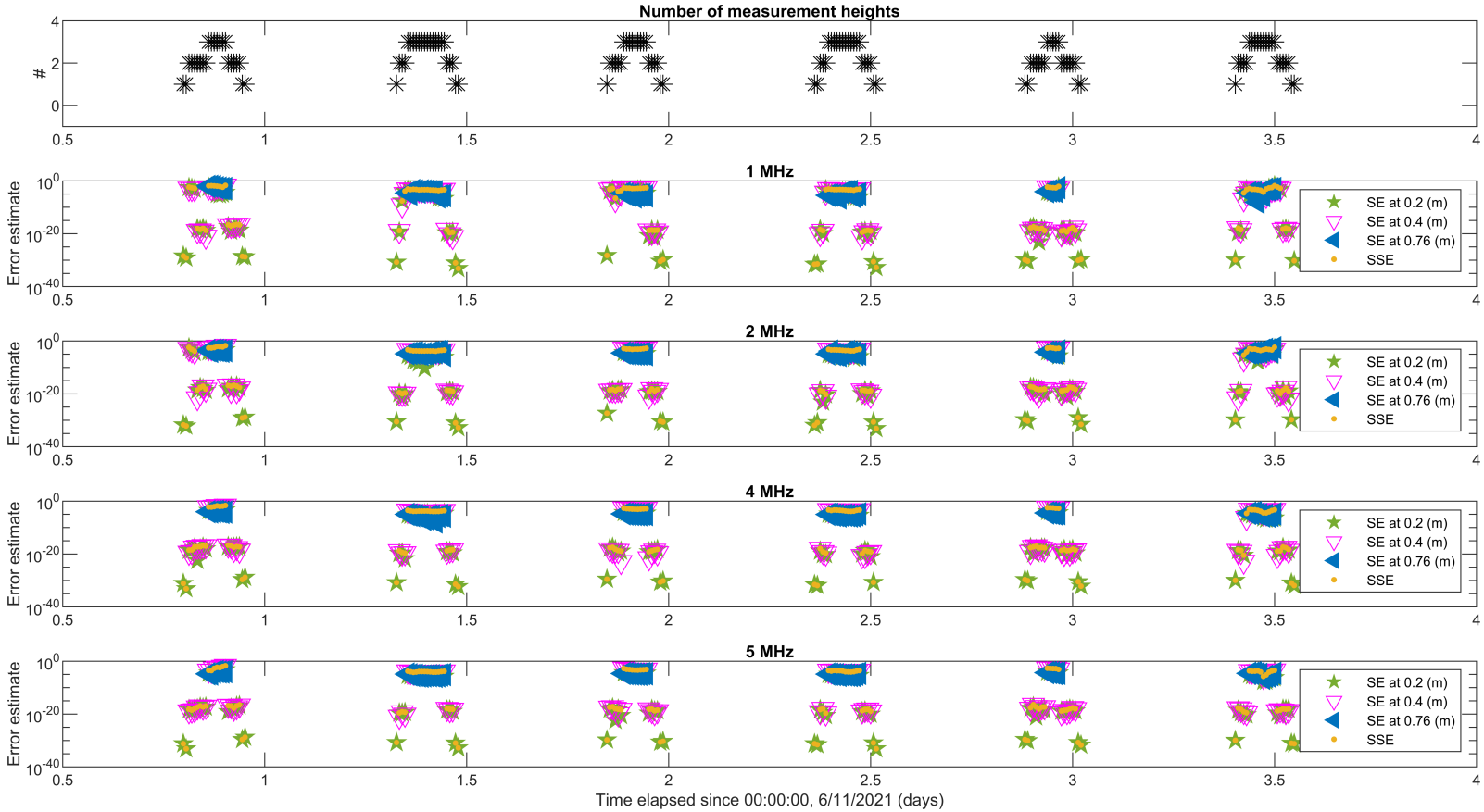

Figure 5.5: Time series of optimised inversion method associated error between M_{ABS} and M_{OBS} profiles taken at each OBS field instrument deployment height at (m) above bed, per burst for each transducer (1, 2, 4, and 5 MHz)

Future research work should focus on improving the inversion methodologies discussed by accounting for changes in particle size distribution, in part driven by flocculation, and the influence these controls have on the scattering characteristics, f_∞ and Σ_s. Implementation of floc size measurement instruments, like a LISST, a floc camera or similar optical instruments (Fox et al., 2004; MacDonald and Mullarney, 2015; Manning et al., 2006; Mikkelsen and Pejrup, 2000) combined with multi-frequency ABS devices deployed in the field, will impart enhanced information on cohesive particle scatterer sizes and behavior, inferred from the differential scattering characteristics from different frequencies.

Chapter 6

Conclusions

In this thesis, we explored the use of acoustic instruments to resolve concentrations of suspended sediments in a coastal setting. The work contributes a novel data set to the limited body of existing work examining acoustic backscatter from suspensions of cohesive particles.

We firstly obtained the intrinsic parameters for our specific instruments by following a recently defined calibration procedure (Wilson & Hay, 2017), and then obtained the acoustic scattering properties, namely f_∞ and Σ_s of mud in a field setting and used these parameters to obtain profiles of SSC. In general the work showed promise for using acoustic techniques in these environmental settings; however, a key finding was that the characteristics of mud from the estuary studied in this thesis, were not universal or indeed could not be broadly applied across multiple tides. However, the experimental results have provided a baseline of reasonable values for f_∞ and Σ_s for cohesive sediments in suspension in the Firth of Thames. These values were not previously available, and thus this thesis provides a useful contribution to the work in this region. Nonetheless, there remains a need for much future work – in particular, by using backscatter data from multiple frequencies to obtain information about particle size distributions.

Appendices

Chapter A

ABS laboratory calibration: single sphere experiment results for all transducers

For each transducer of instrument A and B, Figures (A.1) to (A.7) show the time series of raw, ABS data collected from the tungsten carbide ball laboratory experiments, over a twenty-four range of bins, starting at bin 227.

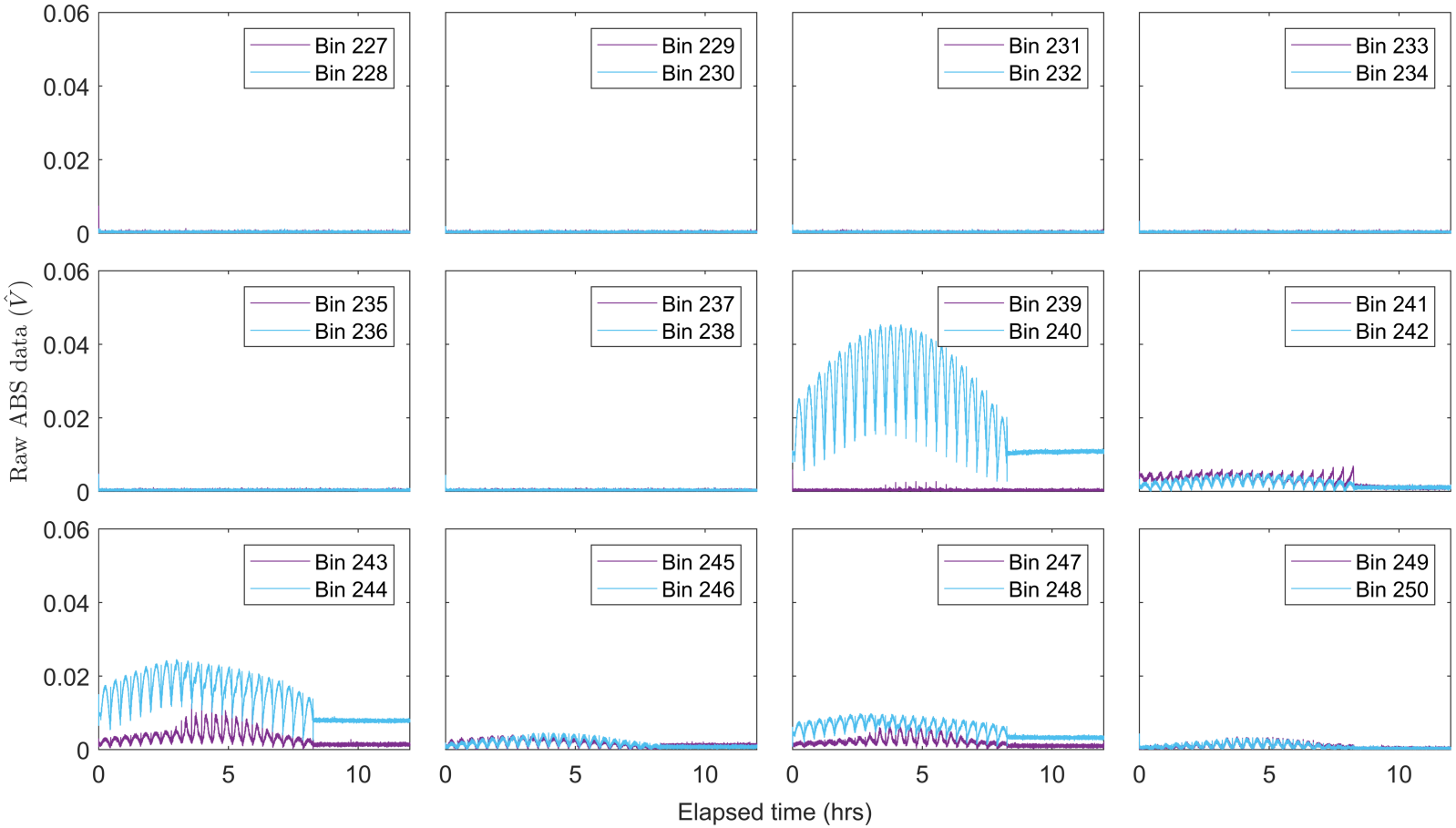

Figure A.1: Time series of the received raw, ABS signal ($\hat{V}$) for the 2 MHz transducer of instrument B from the tungsten ball laboratory experiments.

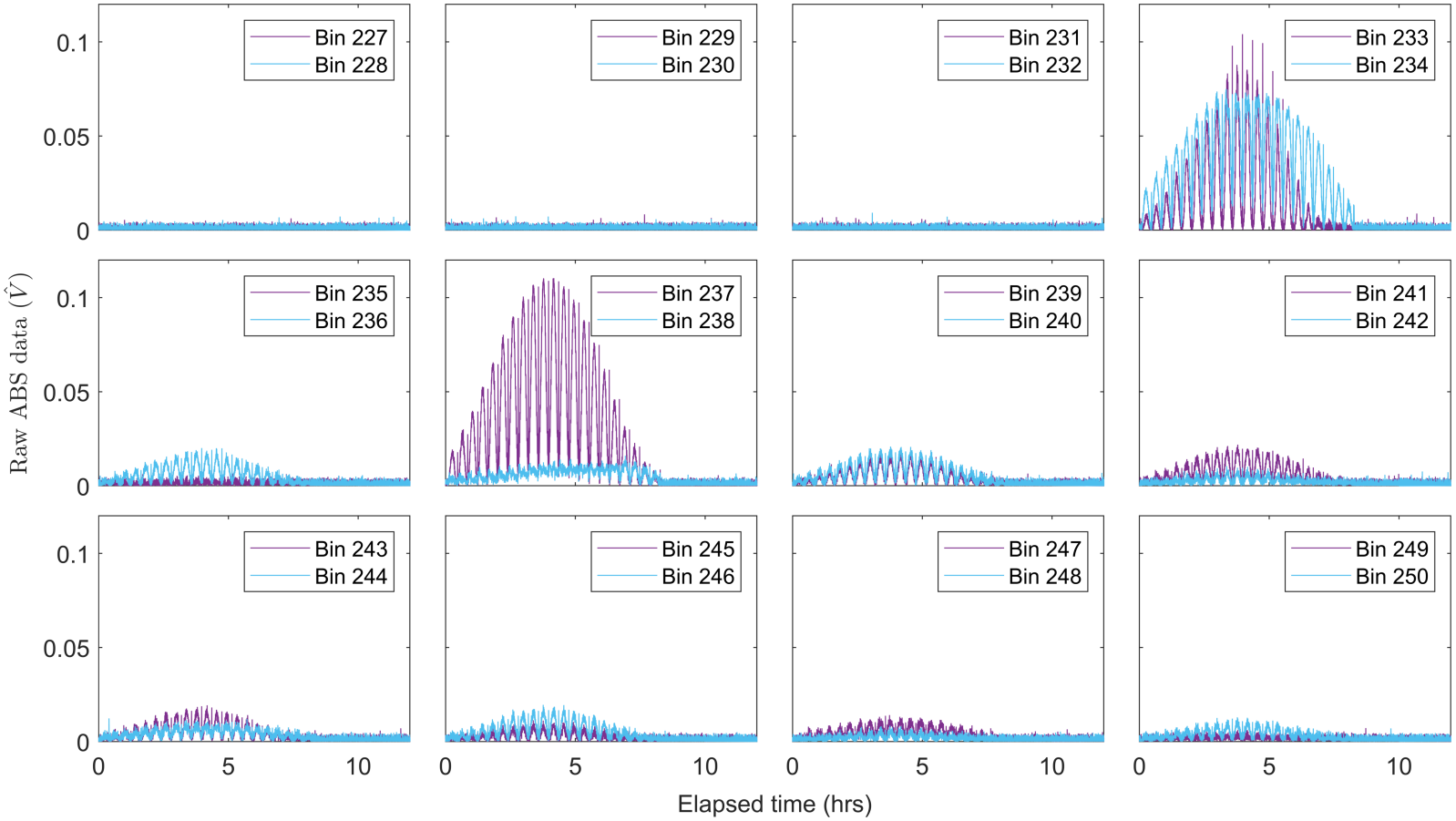

Figure A.2: Time series of the received raw, ABS signal ($\hat{V}$) for the 3 MHz transducer of instrument B from the tungsten ball laboratory experiments.

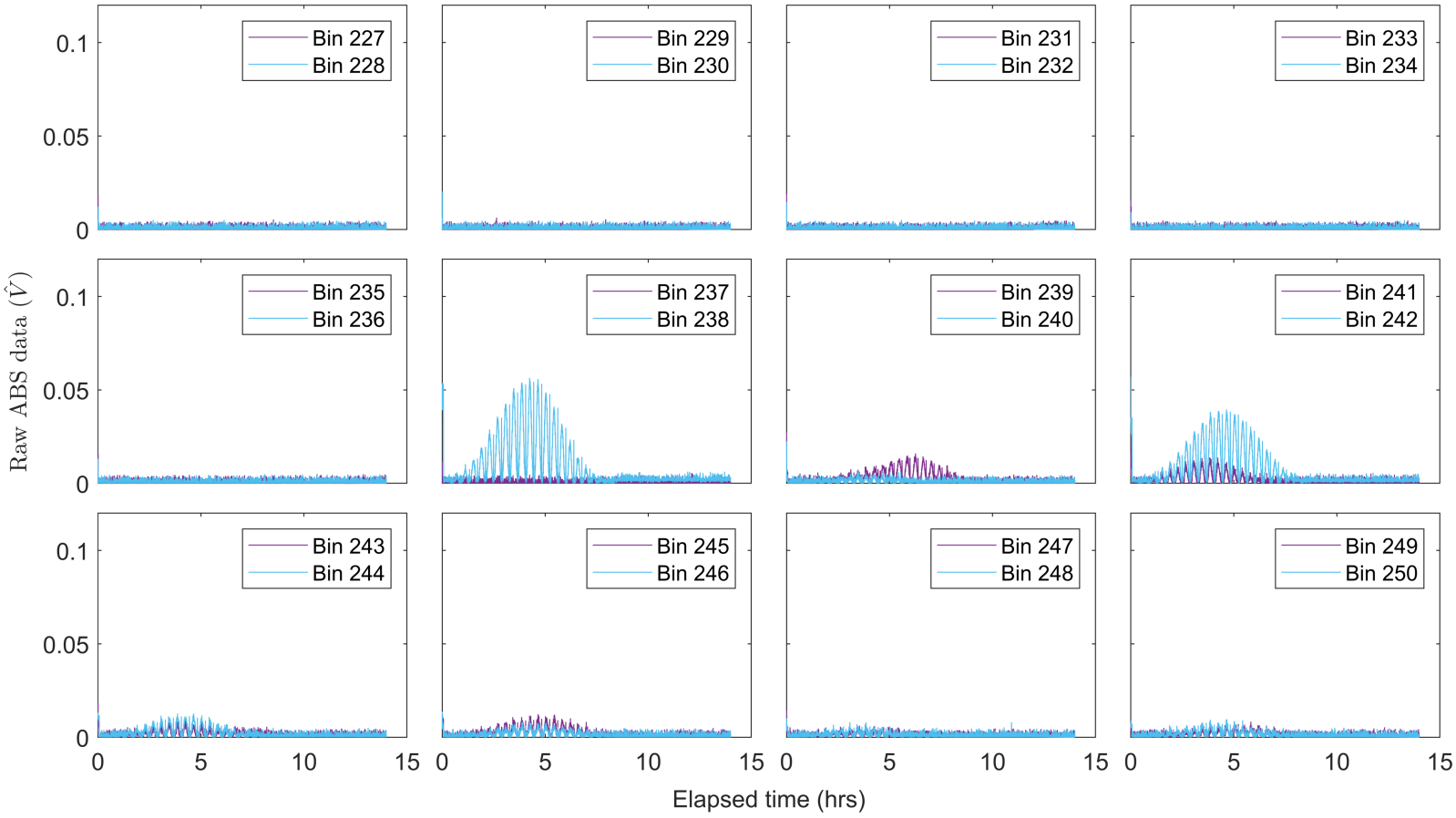

Figure A.3: Time series of the received raw, ABS signal ($\hat{V}$) for the 4 MHz transducer of instrument B from the tungsten ball laboratory experiments.

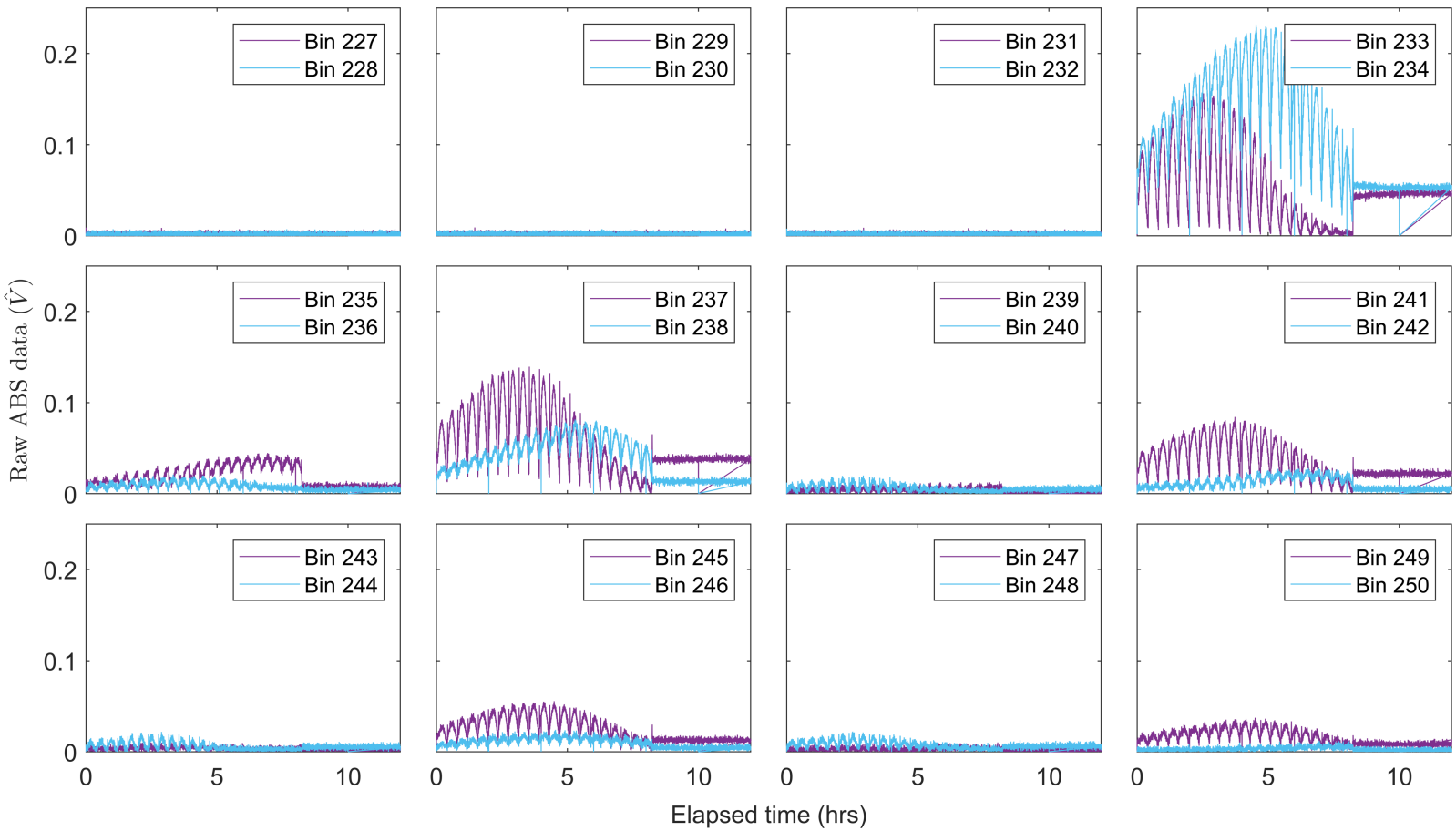

Figure A.4: Time series of the received raw, ABS signal ($\hat{V}$) for the 1 MHz transducer of instrument A from the tungsten ball laboratory experiments.

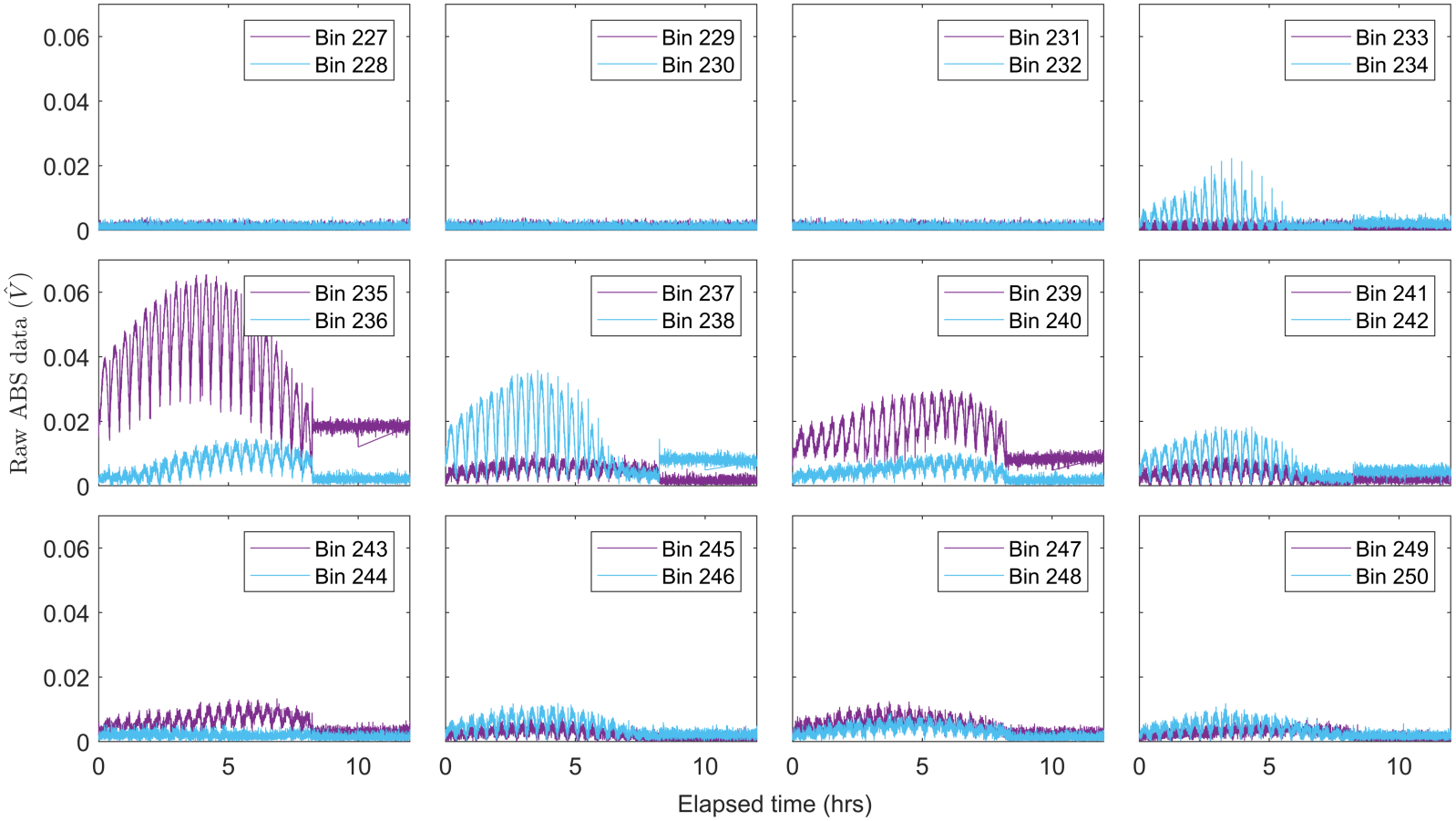

Figure A.5: Time series of the received raw, ABS signal ($\hat{V}$) for the 2 MHz transducer of instrument A from the tungsten ball laboratory experiments.

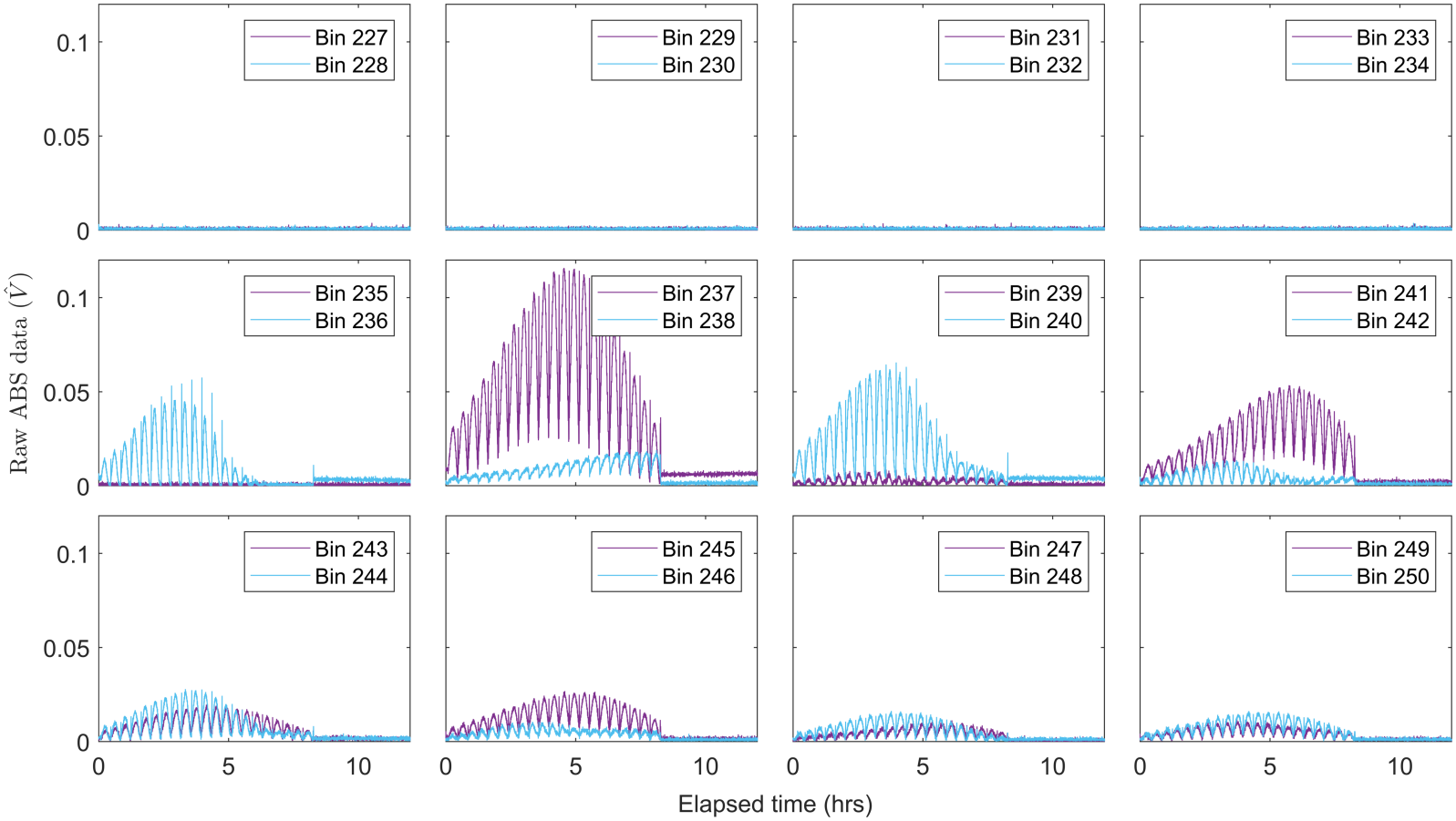

Figure A.6: Time series of the received raw, ABS signal ($\hat{V}$) for the 2.5 MHz transducer of instrument A from the tungsten ball laboratory experiments.

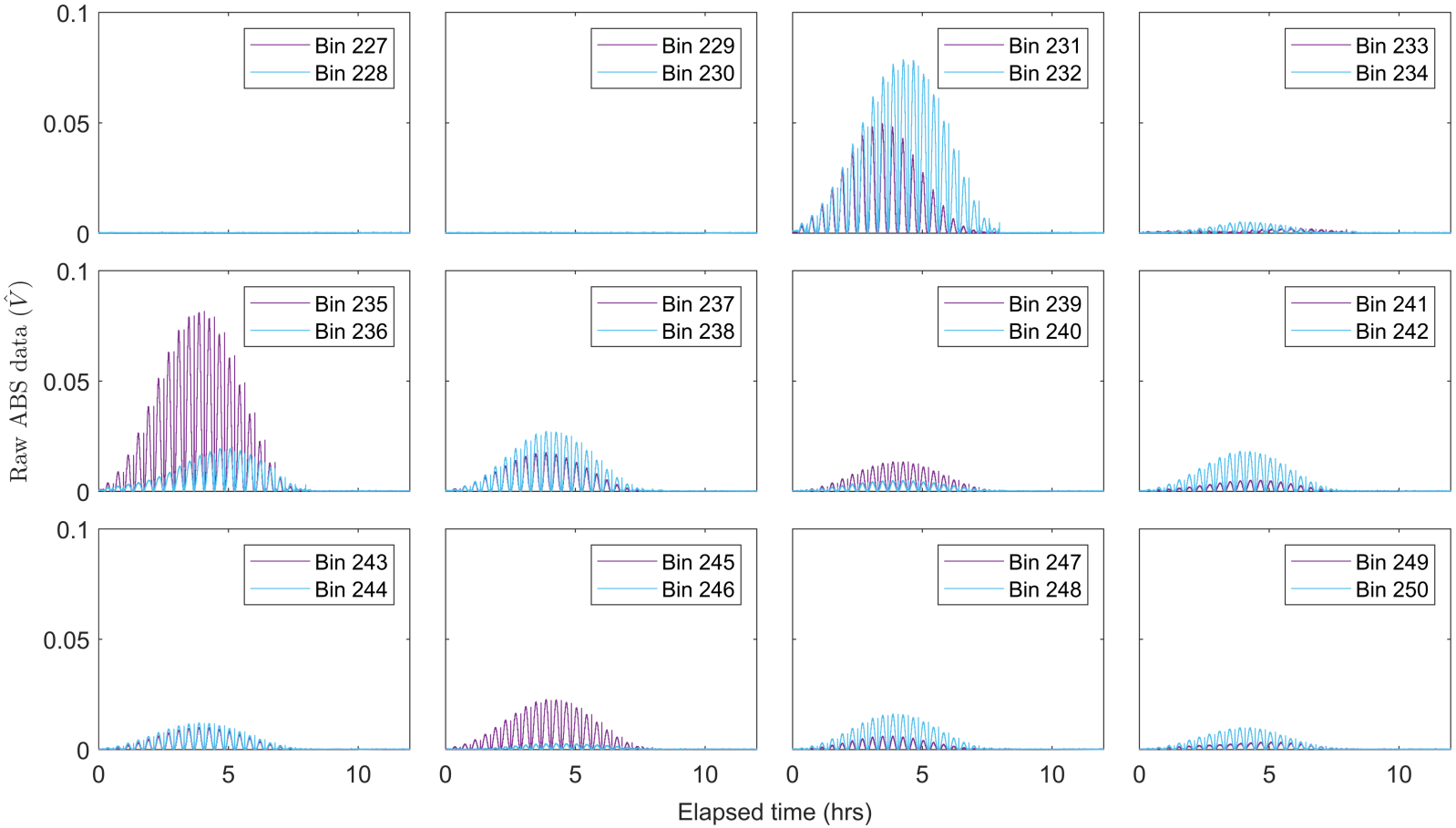

Figure A.7: Time series of the received raw, ABS signal ($\hat{V}$) for the 4 MHz transducer of instrument A from the tungsten ball laboratory experiments.

Chapter B

Field ABS data results: burst files used for linear fit inversion method

Table B.1: Tally of ABS burst files which satisfied $R^2 > 0.95$ for each channel per transducer of instrument A. These listed files were acceptable for the following linear fit inversion analysis.

Channel 1	Channel 2	Channel 3	Channel 4
1 MHz	2 MHz	4 MHz	5 MHz
38	39	38	38
39	40	39	39
40	43	40	40
41	47	41	41
42	112	42	42
43	113	43	43
44	114	44	44
45	115	45	45
345	116	46	46
346	117	47	47
	118	48	48
	119	49	49
	120	111	111
	121	112	112
	122	113	113
	123	116	114
	124	187	116
	194	188	117
	261	189	123
	262	190	125
	263	191	187
	264	192	188
	265	193	189
	267	194	190
	268	195	191
	269	196	192
	270	198	193
	271	199	194
	272	261	195
	273	263	196
	275	264	197
	414	265	198
	415	274	199
	416	275	261
	417	340	262
	418	341	263
		342	264
		343	265
		344	274
		411	275
		412	338
		422	339
			340
			341
			342
			343
			344
			345
			346
			411
			412
			415
			419

References

Abramowitz, M. and I. A. Stegun (2006). *Handbook of mathematical functions with formulas, graphs, and mathematical tables*. Washington: US Govt. Print.

Anh, L. N., D. D. Tran, N. Thong, C. T. Van, D. H. Vinh, N. H. Au, and E. Park (2022). Drastic variations in estuarine morphodynamics in Southern Vietnam: Investigating riverbed sand mining impact through hydrodynamic modelling and field controls. *Journal of Hydrology 608*, 127572.

Barbier, E. B., S. D. Hacker, C. Kennedy, E. W. Koch, A. C. Stier, and B. R. Silliman (2011). The value of estuarine and coastal ecosystem services. *Ecological monographs 81*(2), 169–193.

Betteridge, K. F., P. D. Thorne, and R. D. Cooke. (2008). Calibrating multi-frequency acoustic backscatter systems for studying near-bed suspended sediment transport processes. *Continental Shelf Research 28*(2), 227–235.

Bianchi, T. S. and M. A. Allison (2009). Large-river delta-front estuaries as natural "recorders" of global environmental change. *Proceedings of the National Academy of Sciences 106*(20), 8085–8092.

Bulmer, R. H., F. Stephenson, A. M. Lohrer, C. J. Lundquist, A. Madarasz-Smith, C. A. Pilditch, S. F. Thrush, and J. E. Hewitt. (2022). Informing the management of multiple stressors on estuarine ecosystems using an expert-based Bayesian Network model. *Journal of Environmental Management 301*(3), 113576.

Chapman, P. M. and F. Wang (2001). Assessing sediment contamination in estuaries. *Environmental Toxicology and Chemistry: An International Journal 20*(1), 3–22.

Clay, C. S. and H. Medwin (1977). *Acoustical Oceanography: Principles and Applications*. Wiley-Interscience, New York.

Costanza, R., R. d'Arge, R. D. Groot, S. Farber, M. Grasso, B. Hannon, and K. L. et al. (1997). The value of the world's ecosystem services and natural capital. *Nature 387*(6630), 253–260.

Davies-Colley, R., W. Vant, and D. Smith (2003). *Colour and Clarity of Natural Waters: Science and Management of Optical Water Quality*. The Blackburn Press.

Douglas, E. J., C. A. Pilditch, A. M. Lohrer, C. Savage, L. A. Schipper, and S. F. Thrush (2018). Sedimentary environment influences ecosystem response to nutrient enrichment. *Estuaries and coasts 41*, 1994–2008.

Downing, J. (2006). Twenty-five years with OBS sensors: The good, the bad, and the ugly. *Continental Shelf Research 26*(17-18), 2299–2318.

Eidam, E. F., T. Langhorst, E. B. Goldstein, and M. McLean (2022). OpenOBS: Open-source, low-cost optical backscatter sensors for water quality and sediment-transport research. *Limnology and Oceanography: Methods 20*(1), 46–59.

Fox, J., P. Hill, T. Milligan, A. Ogston, and A. Boldrin (2004). Floc fraction in the waters of the Po River prodelta. *Continental Shelf Research 24*(15), 1699–1715.

Fromant, G., F. Floc'h, A. Lebourges-Dhaussy, F. Jourdin, Y. Perrot, N. Le Dantec, and C. Delacourt (2017). In situ quantification of the suspended load of estuarine aggregates from multifrequency acoustic inversions. *Journal of Atmospheric and Oceanic Technology 34*(8), 1625–1643.

Fugate, D. C. and C. T. Friedrichs (2002). Determining concentration and fall velocity of estuarine particle populations using ADV, OBS and LISST. *Continental Shelf Research 22*(11-13), 1867–1886.

Gray, J. R. (2000). *Comparability of suspended-sediment concentration and total suspended solids data*. Number 4191. US Department of the interior, US Geological Survey.

Guerrero, M., N. Rüther, S. Haun, and S. Baranya (2017). A combined use of acoustic and optical devices to investigate suspended sediment in rivers. *Advances in Water Resources 102*, 1–12.

Hamilton, L. J., Z. Shi, and S. Y. Zhang (1998). Acoustic backscatter measurements of estuarine suspended cohesive sediment concentration profiles. *Journal of Coastal Research 14*(4), 1213–1224.

Hickling, R. (1964). Analysis of echoes from a hollow metallic sphere in water. *The Journal of the Acoustical Society of America 36*(6), 1124–1137.

Hume, T. M., T. Snelder, M. Weatherhead, and R. Liefting (2007). A controlling factor approach to estuary classification. *Ocean & coastal management 50*(11-12), 905–929.

Jones, J. B. (1992). Environmental impact of trawling on the seabed: a review. *New Zealand Journal of Marine and Freshwater Research 26*(1), 59–67.

Kanga, S., G. Meraj, B. Das, M. Farooq, S. Chaudhuri, and S. K. Singh (2020). Modeling the spatial pattern of sediment flow in Lower Hugli estuary, West Bengal, India by quantifying suspended sediment concentration (SSC) and depth conditions using geoinformatics. *Applied Computing and Geosciences 8*, 100043.

Levin, L. A., D. F. Boesch, A. Covich, C. Dahm, C. Erséus, K. C. Ewel, and R. T. K. et al. (2001). The function of marine critical transition zones and the importance of sediment biodiversity. *Ecosystems 142*(3), 430–451.

Little, S., K. L. Spencer, H. M. Schuttelaars, G. E. Millward, and M. Elliott. (2017). Unbounded boundaries and shifting baselines: Estuaries and coastal seas in a rapidly changing world. *Estuarine, Coastal and Shelf Science 198*, 311–319.

Lohrer, A. M., S. F. Thrush, J. E. Hewitt, K. Berkenbusch, M. Ahrens, and V. J. Cummings (2004). Terrestrially derived sediment: response of marine macrobenthic communities to thin terrigenous deposits. *Marine Ecology Progress Series 273*, 121–138.

Lovett, N. (2017). *Sediment transport in the Firth of Thames mangrove forest, New Zealand*. Master's thesis, The University of Waikato.

Ludwig, W. and J. L. Probst (1998). River sediment discharge to the oceans; present-day controls and global budgets. *American Journal of Science 298*(4), 265–295.

MacDonald, I. and J. Mullarney (2015). A novel "FlocDrifter" platform for observing flocculation and turbulence processes in a Lagrangian frame of reference. *Journal of Atmospheric and Oceanic Technology 32*(3), 547–561.

MacDonald, I. T., C. E. Vincent, P. D. Thorne, and B. D. Moate (2013). Acoustic scattering from a suspension of flocculated sediments. *Journal of Geophysical Research: Oceans 118*(5), 2581–2594.

Mackenzie, K. V. (1981). Nine-term equation for sound speed in the oceans. *The Journal of the Acoustical Society of America 70*(3), 807–812.

Manning, A., S. Bass, and K. Dyer (2006). Floc properties in the turbidity maximum of a mesotidal estuary during neap and spring tidal conditions. *Marine Geology 235*(1-4), 193–211.

Medwin, H. and C. S. Clay (1998). *Fundamentals of acoustical oceanography*. Academic Press.

Mehta, A. J. (2013). *An introduction to hydraulics of fine sediment transport*, Volume 38. World Scientific Publishing Company.

Mehta, A. J. (2022). *Introduction To Hydraulics Of Fine Sediment Transport* (2 ed.), Volume 56. World Scientific Publishing Company.

Mikkelsen, O. and M. Pejrup (2000). In situ particle size spectra and density of particle aggregates in a dredging plume. *Marine Geology 170*(3-4), 443–459.

Milligan, T. G. and P. S. Hill (1998). A laboratory assessment of the relative importance of turbulence, particle composition, and concentration in limiting maximal floc size and settling behaviour. *Journal of Sea Research 39*(3-4), 227–241.

Milligan, T. G., P. S. Hill, and B. A. Law (2007). Flocculation and the loss of sediment from the Po River plume. *Continental Shelf Research 27*(3-4), 309–321.

Milligan, T. G. and D. H. Loring (1997). The effect of flocculation on the size distributions of bottom sediment in coastal inlets: implications for contaminant transport. *Water, Air, and Soil Pollution 99*(1), 33–42.

Moate, B. D. and P. D. Thorne (2009). Measurements and inversion of acoustic scattering from suspensions having broad size distributions. *The Journal of the Acoustical Society of America 126*(6), 2905–2917.

Moate, B. D. and P. D. Thorne (2012). Interpreting acoustic backscatter from suspended sediments of different and mixed mineralogical composition. *Continental Shelf Research 46*, 67–82.

Moate, B. D. and P. D. Thorne (2013). Scattering from suspended sediments having different and mixed mineralogical compositions: Comparison of laboratory measurements and theoretical predictions. *The Journal of the Acoustical Society of America 133*(3), 1320–1334.

Moate, B. D., P. D. Thorne, and R. D. Cooke (2016). Field deployment and evaluation of a prototype autonomous two dimensional acoustic backscatter instrument: The Bedform And Suspended Sediment Imager (BASSI). *Continental Shelf Research 112*, 78–91.

Moore, S. A., J. Le Coz, D. Hurther, and A. Paquier (2012). On the application of horizontal ADCPs to suspended sediment transport surveys in rivers. *Continental Shelf Research 46*, 50–63.

National Institute of Water & Atmospheric Research (NIWA) Ltd. (2016). A classification of New Zealand's coastal hydrosystems. *Report number: HAM2016-062* (Prepared for Ministry of the Environment).

Nittrouer, C. A., D. J. DeMaster, E. F. Eidam, T. T. Nguyen, J. P. Liu, A. S. Ogston, and P. V. Phung (2017). The Mekong continental shelf: The primary sink for deltaic sediment particles and their passengers. *Oceanography 30*(3), 60–70.

Nowacki, D. J. and A. S. Ogston (2013). Water and sediment transport of channel-flat systems in a mesotidal mudflat: Willapa Bay, Washington. *Continental Shelf Research 60*, S111–S124.

O'Hara Murray, R. B., P. D. Thorne, and D. M. Hodgson (2011). Intrawave observations of sediment entrainment processes above sand ripples under irregular waves. *Journal of Geophysical Research: Oceans 116*(C1).

O'Laughlin, C., D. Van Proosdij, and T. G. Milligan (2014). Flocculation and sediment deposition in a hypertidal creek. *Continental Shelf Research 82*, 72–84.

Pritchard, D. (1967). What is an estuary: Physical viewpoint. In *Estuaries*, pp. 3–5. American Association for the Advancement of Science, Washington, DC.

Rai, A. K. and A. Kumar (2015). Continuous measurement of suspended sediment concentration: Technological advancement and future outlook. *Measurement 76*, 209–227.

Safak, I., M. A. Allison, and A. Sheremet (2013). Floc variability under changing turbulent stresses and sediment availability on a wave energetic muddy shelf. *Continental Shelf Research 53*, 1–10.

Sahin, C., M. Ozturk, and B. Aydogan (2020). Acoustic doppler velocimeter backscatter for suspended sediment measurements: Effects of sediment size and attenuation. *Applied Ocean Research 94*, 101975.

Sahin, C., I. Safak, T. J. Hsu, and A. Sheremet (2013). Observations of suspended sediment stratification from acoustic backscatter in muddy environments. *Marine Geology 336*, 24–32.

Soulsby, R. L., A. J. Manning, J. Spearman, and R. J. S. Whitehouse (2013). Settling velocity and mass settling flux of flocculated estuarine sediments. *Marine Geology 142*(3), 1–12.

Staudt, F., M. J.C., C. Pilditch, and K. Huhn (2017). The role of grain-size ratio in the mobility of mixed granular beds. *Geomorphology 142*(3), 1655–1662.

Staudt, F., J. Mullarney, C. Pilditch, and K. Huhn (2019). Effects of grain-size distribution and shape on sediment bed stability, near-bed flow and bed microstructure. *Earth Surface Processes and Landforms 44*(5), 1100–1116.

Styles, R. (2006). Laboratory evaluation of the LISST in a stratified fluid. *Marine Geology 227*(1-2), 151–162.

Thorne, P. D. and M. J. Buckingham (2004). Measurements of scattering by suspensions of irregularly shaped sand particles and comparison with a single parameter modified sphere model. *The Journal of the Acoustical Society of America 116*(5), 2876–2889.

Thorne, P. D., A. G. Davies, and P. S. Bell (2009). Observations and analysis of sediment diffusivity profiles over sandy rippled beds under waves. *Journal of Geophysical Research: Oceans 114*(C2).

Thorne, P. D. and D. M. Hanes (2002). A review of acoustic measurement of small-scale sediment processes. *Continental shelf research 22*(4), 603–632.

Thorne, P. D. and A. E. Hay (2012). The application of acoustics to sediment transport processes. *Continental Shelf Research 46*, 1–106.

Thorne, P. D. and D. Hurther (2014). An overview on the use of backscattered sound for measuring suspended particle size and concentration profiles in non-cohesive inorganic sediment transport studies. *Continental Shelf Research 73*, 97–118.

Thorne, P. D., I. D. Lichtman, and D. Hurther (2021). Acoustic scattering characteristics and inversions for suspended concentration and particle size above mixed sand and mud beds. *Continental Shelf Research 214*, 104320.

Thorne, P. D., I. T. MacDonald, and C. E. Vincent (2014). Modelling acoustic scattering by suspended flocculating sediments. *Continental Shelf Research 88*, 81–91.

Thorne, P. D. and R. Meral (2008). Formulations for the scattering properties of suspended sandy sediments for use in the application of acoustics to sediment transport processes. *Continental Shelf Research 28*(2), 309–317.

Thorne, P. D., C. E. Vincent, P. J. Hardcastle, S. Rehman, and N. Pearson (1991). Measuring suspended sediment concentrations using acoustic backscatter devices. *Marine Geology 98*(1), 7–16.

Thrush, S. F., J. E. Hewitt, V. J. Cummings, J. I. Ellis, C. Hatton, A. Lohrer, and A. J. F. I. E. Norkko (2004). Muddy waters: elevating sediment input to coastal and estuarine habitats. *Frontiers in Ecology and the Environment 2*(6), 299–306.

Thrush, S. F., M. Townsend, J. E. Hewitt, K. Davies, A. M. Lohrer, C. Lundquist, K. Cartner, and J. Dymond (2013). The many uses and values of estuarine ecosystems. In *Ecosystem services in New Zealand–conditions and trends*, pp. 226–237. Manaaki Whenua Press, Lincoln, New Zealand.

Urlich, S. C. (2020). Opportunities to manage sediment from forestry more effectively in the Marlborough Sounds and contributing catchments. *NZ Journal of Forestry 65*(2), 29.

Vergne, A., J. Le Coz, C. Berni, and G. Pierrefeu (2020). Using a down-looking multifrequency ABS for measuring suspended sediments in rivers. *Water Resources Research 56*(2), 1–19.

Wilson, G. W. and A. E. Hay (2015). Acoustic backscatter inversion for suspended sediment concentration and size: A new approach using statistical inverse theory. *Continental Shelf Research 106*, 130–139.

Wilson, G. W. and A. E. Hay (2017). Short-pulse method for acoustic backscatter amplitude calibration at MHz frequencies. *The Journal of the Acoustical Society of America 142*(3), 1655–1662.

Winterwerp, J. C. (1998). A simple model for turbulence induced flocculation of cohesive sediment. *Journal of hydraulic research 36*(3), 309–326.

Winterwerp, J. C., A. J. Manning, C. Martens, T. De Mulder, and J. Vanlede (2006). A heuristic formula for turbulence-induced flocculation of cohesive sediment. *Estuarine, Coastal and Shelf Science 68*(1-2), 195–207.

Wren, D. G., B. D. Barkdoll, R. A. Kuhnle, and R. W. Derrow (2000). Field techniques for suspended-sediment measurement. *Journal of Hydraulic Engineering 126*(2), 97–104.